Swanson School of Engineering

Undergraduate Summer Research Program

Summer 2013

Swanson School of Engineering

Undergraduate Summer Research Program

One advantage of a research university is the opportunity that it provides for undergraduate students to become involved in cutting edge research with leading scientists and engineers. The University of Pittsburgh and its Swanson School of Engineering are no different. This past spring, the Swanson School invited all undergraduates to propose a research topic of interest and to identify a faculty mentor who would serve as a sponsor. Students were not restricted to the Swanson School of Engineering or even the University of Pittsburgh. The world was fair game. In fact, two students journeyed Germany to work with colleagues at the Hannover Medical school (as an outreach of our Engineering Research Center).

In all, we were able to fund 41 students, with generous support from the Office of the Provost; additional support was provided by the Swanson School of Engineering and individual investigators Jorge Abad, April Chambers, Traci Cui, Lance Davidson, Richard Debski, Shawn Farrokhi, Eric Lagasse, Steven Little, Scott Tashman, Gelsy Torres-Oviedo and David Vorp. Students came from all of the Swanson School's six departments. Mentors came from throughout the University of Pittsburgh as well as the above noted Hannover Medical School. Each student received a grant of $3,500; the only obligations were to write a two-page abstract at the end of the summer and submit a poster abstract to Science 2013 – Convergence in October. Many of the students also present posters in their special undergraduate student research session event at Science 2013.

This document contains the students' abstracts. It demonstrates the creative, intellectually challenging research that our undergraduates are conduction, and our students' wide range of interests. In presenting this work, we also want to acknowledge and thank those faculty mentors who made available their laboratories, their staff, and their personal time to assist the students and further spark their interest in research.

David A. Vorp
Larry J. Shuman

Student		***Mentor***		***Title of Research***
Jennifer L. Yeager	BioE	Steven D. Abramowitch	BioE	*Improving the Performance of a Biaxial Device to Mechancially Test Highly Compliant Planar Tissues*
Joseph C. Kennedy	BioE	Bryan N. Brown	BioE	*Evaluation of Macrophage Phenotype in the Pathogenesis of Endometriosis*
Joan R. Guyer	BioE	April J. Chambers	BioE	*Ergonomic Analysis of Microlaryngoscopy Using Surface Electromyography*
Tyler B. Pirkle	BioE	Kevin C. Chan	BioE, Ophthalmology	*Magic Angle Enhanced Microscopy of Fibrous Ocular Structures*
Andrew J. Macgregor	BioE	Xinyan Tracy Cui	BioE	*Automated Impedance Modeling to Streamline Analysis of Neural Electrode Implantation*
Linn Zhang	BioE	Xinyan Tracy Cui	BioE	*PEDOT/GO Carbon Fiber Microelectrode for Dopamine Detection*
Eric B. Weston	BioE	Xinyan Tracy Cui & Lance A. Davidson	BioE	*Further Characterization of Electrically Induced Contractility of Intact Embryonic Tissues on a Microelectrode Array*
Jonathan D. Brokaw	BioE	Richard E. Debski	BioE	*Development of 6 Degrees of Freedom Clamps for the Study of Human Shoulder- and Knee-Joint-Complexes*
Ryan J. Mooney	BioE	Marina V. Kameneva	BioE	*Evaluation of Functionality of Modified Red Blood Cells for Intravascular Drug Delivery*
Casey E. Rayburg	BioE	Sanjeev G. Shroff	BioE	*Automated Quantification of Interstitial and Perivascular Cardiac Fibrosos in the MREN2(27) Transgenic Rat Model*
Thomas W. Rotella	BioE	Gelsy Torres-Oviedo	BioE	*Increasing Natural Variance to Improve Transfer of Motor Learning from Treadmill to Over Ground Walking*

* Abstract withheld to protect intellectual property

Student		Mentor		Title of Research
Alexander D. Josowitz	BioE	David A. Vorp	BioE	*A Method for Assessing the Seeding Efficiency of Human Adipose-Derived Stem Cells in Synthetic Scaffolds*
Scott W. Thompson	ECE	Douglas J. Weber	BioE	*A Multi-Channel Electrical Micro-Stimulation System for Sensory Feedback Research*
Gerald T. McFarlin IV	ChE	Anna C. Balazs	ChE	*Dynamic Ability of Fiber-Filled Gels to Control Oil-Droplet Motion in Water Systems*
Kimaya Padgaonkar	ChE	Ipsita Banerjee	ChE	*Investigation of Human Embryonic Stem Cell Differentiation Induced by Chitosan Nanoparticles*
Patrick A. Bianconi*	BioE	Steven R. Little	ChE	*Controlled Release of Dorsomorphin to Prevent the Terminal Differentiation of Mesenchymal Stem Cells: A Potential Method for Articular Cartilage**
Anthony V. Cugini Jr.	BioE	Steven R. Little	ChE	*Using MSC-Conditioned Media to Reconstruct Gluococorticoid Damaged Trabecular Meshwork Cytoskeleton*
Jahnelle C. Jordan*	BioE	Steven R. Little	ChE	*Microparticle-Based Systems to Mimic or Manipulate Antigen Presenting Cells**
Meghana A. Patil*	BioE	Steven R. Little	ChE	*Controlled-Release Kartogenin: A Treatment for Cartilage Regeneration in Osteoarthritis**
Martin D. Roberts	ChE	Götz Veser	ChE	*Nanoscale Heterogenization of Homogeneous Acetylation Catalysts using Nickel Lined Silica Nanoparticles*
Adrian Mikhail P. Garcia	CEE	Jorge D. Abad	CEE	*Migration Rates and Metrics of the Peruvian Amazon*
Brian W. Hone	CEE	Jorge D. Abad	CEE	*Characterization of Bends in Meandering Rivers*

* Abstract withheld to protect intellectual property

Student		***Mentor***		***Title of Research***
John Teoli IV	ECE	Ervin Sejdić	ECE	*The Angait Device; A Simple Means for Diagnosing Gait Deficiencies*
Donald K. Voland Jr.	MEMS	Minhee Yun	ECE,BioE	*Synthesis of Graphene for Use in Applied Electronic Devices*
Devon L. Albert	BioE	Frank Witte	Hannover Medical School	*Three Magnesium-Rare Earth Alloys as Biomaterials*
Liza A. Bruk	BioE	Frank Witte	Hannover Medical School	*Antibacterial Effects And Cytotoxicity Of Varied Silica Nanoparticles*
Aniket C. Patel	BioE	Youngjae Chun	IE	*A Microfluidic Study for Osteoblast Cell Responses*
David J. Eckman	IE	Denis R. Sauré	IE	*Multi-Armed Bandit with Correlated Rewards*
Michael P. Nites	IE	Andrew J. Schaefer	IE	*The Characterization of a Pure Integer Program Through a Linear Program*
Alexander P. Valentino	MEMS	Mark L. Kimber	MEMS	*Impinging Jet Effects of Turbulent Flows*
Fangzhou Cheng*	MEMS	Anne M. Robertson	MEMS	*Design and Manufacture of a New Catheter/Guidewire System**
Jeremy W. Murphy	MEMS	Paolo Zunino	MEMS	*Motion of a Rigid Body with a Cavity Filled with Viscous Fluid*
Sarah E. Higbee	ECE	Stephen D. Meriney	Neuroscience	*Calcium Channels in Synaptic Structure*

* Abstract withheld to protect intellectual property

Student		***Mentor***		***Title of Research***
Greta R. Brecheisen	BioE	Scott Tashman	Orthopaedic Surgery	*In Vivo Three Dimensional Kinematics of the Knee During Downhill Running*
Timothy N. Thompson	BioE	Eric Lagasse	Pathology	*PRL-3 Mediates Colony Formation of Mouse Tumor Cells In Vitro*
Matthew J. Pincus	ChE	Xiang-Qun (Sean) Xie	Pharmacy	*Escherichia Coli Expression, Purification and Artificial Chaperone Refolding of Recombinant SQSTM1/p62 ZZ-Domain Protein Fragments for Structure/Function Studies*
Paige E. Kendell	ECE	Shawn Farrokhi	Physical Therapy	*Determining the Threshold of Beneficial Walking in Patients with Knee Osteoarthritis*
Megan E. Robinson	BioE	Shawn Farrokhi	Physical Therapy	*Increased Variability of Knee Motion Among Knee Osteoarthritis Patients with Epesodic Reports of Instability*
Jake R. Bosin	BioE	Colleen A. McClung	Psychiatry	*Effects of Pharmacogenetic Manipulation of the Nucleus Accumbens on Alcohol-Induced Taste Aversion*
Deanna C. Pelkey	BioE	Theodore J. Huppert	Radiology	*Creation of a Handheld NIRS Imaging Device for Infants*
Drake D. Pedersen	BioE	William R. Wagner	Surgery, BioE, & ChE	*Characterizing Real-Time Platelet Deposition Onto Clinically Relevant Surfaces*

* Abstract withheld to protect intellectual property

IMPROVING THE PERFORMANCE OF A BIAXIAL DEVICE TO MECHANICALLY TEST HIGHLY COMPLIANT PLANAR TISSUES

Jennifer Yeager[1], William Barone[1], Pamela A. Moalli[2] MD, PhD, Steven Abramowitch[1,2], PhD
[1]Musculoskeletal Research Center, Department of Bioengineering
[2]Urogynecology & Reconstructive Pelvic Surgery, Magee-Women's Hospital
University of Pittsburgh, PA, USA
Email: jly24@pitt.edu Web: http://www.pitt.edu/~msrc/

INTRODUCTION

Soft tissue biomechanics is an important aspect of clinical and engineering research. Some important tissues being studied include skin, tendons, heart valves, blood vessels, and vaginal tissue.

Soft tissues exhibit unique biomechanical properties, making traditional uniaxial testing insufficient. Thus, biaxial testing is important because this allows a deeper knowledge of structure-function relationships. Additionally, it provides insight into the axial coupling relationships and often better simulates in-vivo loading states. Also, biaxial testing is important for constitutive modeling in that it allows for a direct measurement of tissue anisotropy. However, biaxial testing is limited by several factors. These include sample geometries, difficulty achieving an equal force distribution in plane, specimen variability, and possible damage due to clamping or fixing the specimen to the device. [1]

The most limiting factor in our biaxial testing device was friction within the system. Because the soft tissues of interest in our laboratory are highly compliant, the amount of friction in the system could not be assumed to be negligible. In order to meaningfully test these tissues, the biaxial testing device needed to be modified to eliminate this source of error.

METHODS

Eliminating friction required a complete redesign of the system. Therefore, several design criteria were developed:

- Friction must be minimized
- A modified strain tracking system must be incorporated to allow custom post-analysis
- A new water bath must be designed to allow testing active mechanical properties
- Longer hooks must be created to attach to the tissue, but do not alter the applied load

After considering the design criteria, the initial design was developed. This design featured four sleds on four tracks, arranged to create two perpendicular axes of motion. Figure 1 depicts the initial design for a sled and track.

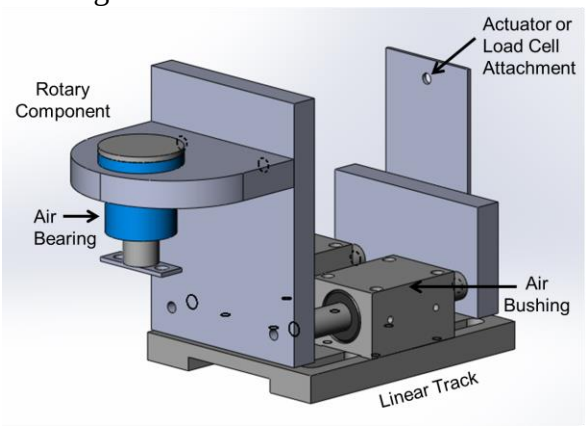

Figure 1: Solidworks drawing for new biaxial testing device design depicting a sled and track

I. Eliminating Friction with Air Bearings

New Way air bearings and bushings were used to combat friction. These air bearings supply pressurized air through a porous media creating a zero contact surface allowing frictionless motion.

II. Air Bearings Validation

To confirm that the air bearings were successfully facilitating frictionless movement, a validation procedure was developed. A load cell was attached to a linear actuator and known masses were displaced on the track in a sinusoidal waveform. The corresponding function for the displacement waveform was found using Mathematica and the acceleration waveform was subsequently calculated. The maximum theoretical force was then determined using Newton's second law and compared to the maximum force measured by the load cell.

VI. Hook Development

Due to the addition of the linear track, the new hook design required a much greater length than the

original hooks. The design for the hooks was fabricated from suture and small fly fishing hooks. This resulted in a long segment of suture with a hook attached by a surgical knot at each end. Small pieces of cork were placed on the hooks making them buoyant. The hooks were attached to the device by wrapping the suture around a spindle connected to the rotary component. This method allows in plane shear and does not restrict the hooks.

VII. Preliminary Hook Testing

To test this hook design, preliminary testing was conducted using the new biaxial testing device and rat skin samples. The samples were approximately 2 cm x 2 cm. Four hooks, two sets of two, were attached to each side of the sample. The protocol applied an equal displacement of four millimeters on each axis.

RESULTS

The new biaxial testing device, including the new water bath, is shown below in Figure 2.

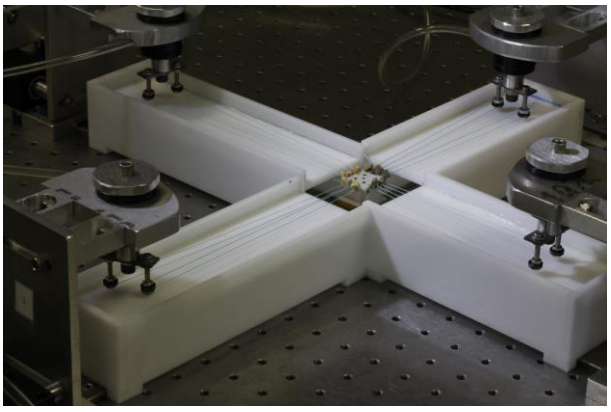

Figure 2: New biaxial testing device with new water bath

I. Air Bearings Validation

The validation procedure has been performed on one sled. The comparison of the theoretical force sinusoid and the measured force sinusoid is displayed in Figure 3.

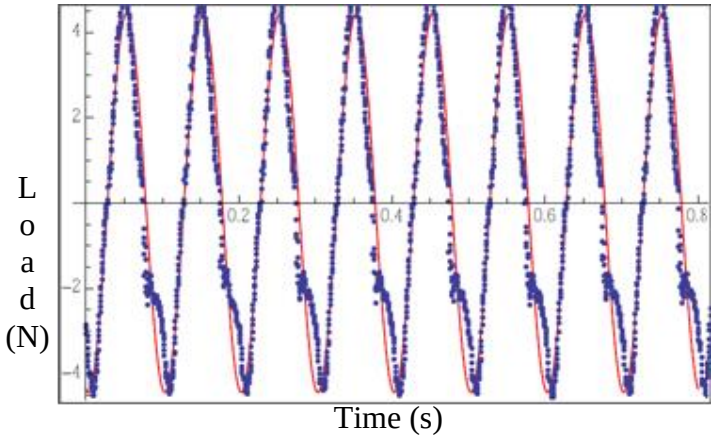

Figure 3: Comparison of the calculated theoretical force (red) and the measured force (blue) from the load cell during

This procedure revealed a percent difference between measured and theoretical force of approximately 2.46% after neglecting the inertial forces from moving the load cell on the actuator.

II. Preliminary Hook Testing

Preliminary testing of the hooks revealed that suture was not an ideal material. The suture would initially transfer tension to the tissue. However, after returning the specimen to its zero displacement position, the suture would become slacked, indicating a permanent plastic deformation.

DISCUSSION

In this project, we determined that the original biaxial testing device was unsuitable for highly compliant soft tissues. Determining its major weakness as friction, we developed a design for a new biaxial testing device to eliminate friction as well as introduce several other improvements.

The new design satisfies multiple design criteria. The air bearing validation indicates that friction is negligible in the new design. Additionally, both a modified strain tracking system and a new water bath have been incorporated into the system. These improvements over the previous system allow for more accurate testing of highly compliant tissues, and a higher level of control over the data being collected.

The remaining limitation in the system is the deformability of the hooks, resulting in failure to meet all of the design criteria at this point in time. In the future, it is important to develop a new hook design that is resistant to plastic deformation, able to float, and accommodate small sample sizes. Additionally, further validations should be performed on the air bearings to confirm that the friction in the other sleds is negligible as well.

REFERENCES

1. Sacks, M. 2001. Biaxial Mechanical Evaluation of Planar Biological Materials. *Journal of Elasticity*, 61: 199-246.

ACKNOWLEDGMENTS

Thank you to Katrina Knight and the Musculoskeletal Research Center for their mentoring and support as well as Dean Shuman for providing summer research funding.

EVALUATION OF MACROPHAGE PHENOTYPE IN THE PATHOGENESIS OF ENDOMETRIOSIS

Joseph Kennedy, Deepa Mani, Nicole Donnellan and Bryan Brown
McGowan Institute of Regenerative Medicine, Magee-Womens Research Institute, Department of Bioengineering
University of Pittsburgh, PA, USA
Email: jck49@pitt.edu, Web: http://mirm.pitt.edu/

INTRODUCTION

Macrophage populations with distinct phenotypes have recently received attention as predictors of disease pathogenesis in processes such as cancer, atherosclerosis, periodontitis, and fibrosis, among many others. Specifically, macrophages have also been described as having phenotypes that range along a spectrum from pro-inflammatory (M1) to anti-inflammatory/regulatory (M2). Endometriosis is a disease characterized by endometrial glands and stroma being present outside of the uterus; inflammation, adhesions, pain and infertility are also associated with the disease. The disease represents the third leading cause of hospitalization for gynecologic indications and affects over 5 million individuals in the United States.

Despite the prevalence of the disease, the etiology is unknown. Endometriosis is assumed to result from retrograde menstruation or from a dysregulated inflammatory response. To date, the inflammation has largely been assessed in the peritoneal fluid, rather than on a tissue level. A small number of studies that have investigated endometriosis on the tissue level have shown macrophage polarization may play a role in helping the endometrial tissues survive outside of the uterus. Perplexingly, while the peritoneal fluid shows an increased level of inflammatory factor, tissue level examinations show that the anti-inflammatory response is prevalent within endometriotic lesions. The discovery suggests while endometriotic lesions are considered to be benign, a number of parallels can be drawn between the inflammatory process in cancer and endometriosis, implying the cells are able to evade the immune system through manipulation of a locally favorable environment.

The aim of this project was to develop methods for quantitative assessment of macrophage phenotype at the tissue level in endometriotic lesions from the peritoneal cavities of human patients. The results obtained from these methods will also be correlated to quality of life surveys to measure the role macrophage phenotype plays in the progression and symptoms of the disease. We hope to understand the mechanisms of endometriosis, such as pain and infertility, and hope to inform future biomaterial strategies for the treatment of endometriosis and reconstruction of affected lesions.

METHODS

Tissue Collection

Tissues were collected from sixty-nine human patients who were diagnosed with endometriosis. The patients underwent laparoscopic surgery and biopsies were taken from several sites of endometriosis (including peritoneum, uterosacral ligament, and ovarian fossa) and a control section (no lesions).

Hematoxylin & Eosin

To show the morphology of the glands and stroma present in the lesions, slides underwent hematoxylin and eosin staining. Sections were placed in decreasing ethanol washes (100%, 95%) twice for 1 minute each, followed by 2 Type I water washes for 1 minute. Sections were placed in Gill's III hematoxylin for 1minute and 30 seconds and then rinsed twice for 30 seconds in Type I water, followed by 3 dips in glacial acetic acid, and then rinsed again in water twice for 1 minute. The sections were counterstained with Eosin Y (1% Solution in Water) for 2 minutes, followed by increasing ethanol washes (95%, 100%) and dehydrated in xylene; slides were coverslipped using non-aqueous mounting medium and stored at room temperature. Pictures were taken using a Nikon E600 microscope fitted with a Nuance multispectral imaging system.

Immunofluorescent Labeling

The biopsies were embedded in optimal cutting temperature compound and flash-frozen in liquid

nitrogen at -80°C. 5 µm thick sections were fixed with 50:50 methanol-acetone for 10 minutes at room temperature and then placed in antigen retrieval buffer for 20 minutes at 95°C. After cooling, the sections underwent 10 mM $CuSO_4$ incubation at 37°C for 35 minutes to reduce auto-fluorescence. After incubation, tissue sections were incubated in PBS + 2% bovine serum albumin for 1 hour at room temperature and then overnight at 4°C with mouse CD68 mAb (clone number KP-1, Abcam), rabbit CD86 mAb (clone number EP1158Y, Abcam), and goat polyclonal CD206 (Santa Cruz), staining cell markers for macrophages, M1 macrophages and M2 macrophages, respectively, over a range of dilutions from 1:50 to 1:150. Endothelial cells were identified by staining with rabbit polyclonal CD31 (Abcam). Primary antibodies were identified by using Alexa Fluor 594 donkey anti-mouse, 568 donkey anti-rabbit, 488 donkey anti-goat, and 488 donkey anti-rabbit (Invitrogen) using a range of dilutions from 1:100 to 1:250. Slides were counterstained with DAPI and examined using a FLoid Cell Imaging Station. Parallel slides in which primary antibody had been omitted were used as negative controls.

TUNEL

To show any apoptotic cells/cell death occurring around the glands/stroma, a TUNEL stain was performed. Sections underwent 4% paraformaldehyde fixation for 20 minutes at room temperature, followed by a 1x PBS wash for 30 minutes. After washing, sections were placed in permeabilisation solution (0.1% Triton X-100/0.1% sodium citrate) for 2 minutes at 4°C. Samples were then given TUNEL reaction mixture (50 µL Enzyme Solution, 450 µL Label Solution) and incubated for 1 hour at 37°C in the dark. Slides were counterstained with DAPI and examined using a FLoid Cell Imaging Station. Two samples on different slides were kept as negative controls and received only label solution.

RESULTS

Paraffin-embedded slides exhibited a better preserved tissue morphology, as well as providing brighter and clearer stains than their frozen tissue counterparts.

Figure 1 below displays a comparison between the frozen (see left side) and paraffin sections (see right side) and how the immunoflourescent labeling appeared for each

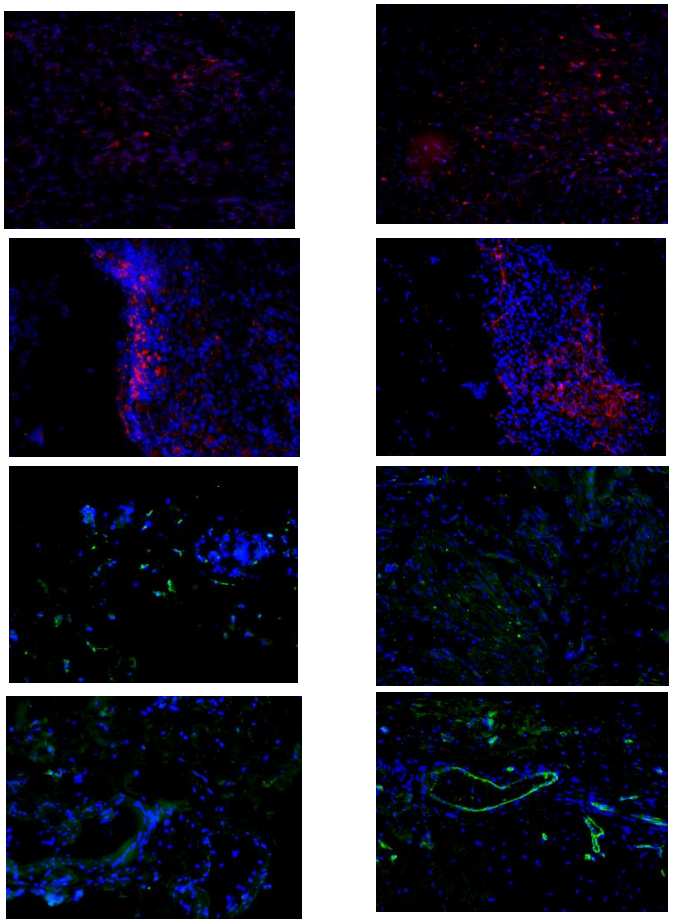

Figure 1: Pictures of immunoflourescent labeled sections staining for CD68 (top row), CD86 (second row), CD206 (third row), and CD31 (bottom row). Pictures of the frozen sections are on the left side, while pictures of the paraffin sections are on the right side. Both kinds of sections received a primary dilution of 1:50 and a secondary dilution of 1:100

DISCUSSION

The difference between frozen and paraffin sections is easily seen; the paraffin sections show a much brighter stain and did not require the use of $CuSO_4$ incubation to reduce autofluorescence, unlike the frozen sections. Furthermore, we can see the frozen sections show slight disturbance in their overall morphologies, whereas the paraffin sections remain largely undisturbed.

Going forward in this project, we propose to stain primarily paraffin sections due to their more favorable outcomes in the process of immunofluorescent labeling and keeping of the overall structural integrity of the sample. In conclusion, we have developed a set of staining, labeling, and imaging methods which will allow for quantification of the host innate immune response in endometriosis. Ongoing studies are being performed to develop automated methods for quantification of images and to quantify the cellular response and relate it to quality of life measures.

ERGONOMIC ANALYSIS OF MICROLARYNGOSCOPY USING SURFACE ELECTROMYOGRAPHY

Joan R. Guyer[1], Grace E. Owens[1], Jenna M. Trout[1], Libby J. Smith[2], Clark A. Rosen[2], April J. Chambers[1]
[1]Human Movement and Balance Laboratory, Department of Bioengineering
[2]Department of Otolaryngology
University of Pittsburgh, PA, USA
Email: jrg97@pitt.edu, Web: http://www.engineering.pitt.edu/hmbl/

INTRODUCTION Proper ergonomic positioning in the workplace is crucial in preventing musculoskeletal disorders (MSD) resulting from prolonged muscular fatigue. Specifically in microlaryngoscopy, surgeons often disregard proper ergonomic positioning in favor of dexterity and range of motion during surgery, leading to increased muscle fatigue through neck strain and compressive forces [1]. Similar MSDs are the most common reason for premature retirement in comparable medical occupations [2].

It is possible to quantify muscular fatigue that can lead to MSDs using surface electromyography (sEMG). The effects of muscle fatigue, a decrease in the muscle's ability to generate force, are evident in the myoelectric signal [3]. Both an increase in the amplitude of the sEMG signal, due to recruitment of additional motor units, and a shift towards a lower frequency spectrum, due to a decreased fiber conduction velocity from lactic acid build-up, indicate muscular fatigue [3]. The objective of this study was to use conclusions from sEMG data and ergonomic principles to analyze microlaryngeal operative postures, thus distinguishing favorable versus unfavorable surgical positioning.

METHODS Twelve healthy otolaryngology residents (7 male; mean age 31.1 ± 3.7 years) who were in their second to sixth years of residency participated in the study. No participants reported any musculoskeletal problems prior to testing. EMG sensors (Delsys, Inc.; Boston, MA) were placed at seven locations on the dominant side: the lower, middle, upper, and cervical trapezii; triceps; anterior deltoid; and extensor carpi radialis. Participants' skin was cleansed with alcohol wipes, and electrodes were affixed using EMG adhesive. For each muscle, participants executed a maximum voluntary contraction (MVC) for five seconds to be used for normalization purposes. Surgeons used a microsuspension laryngoscopy simulator (Emory University; Atlanta, GA) in pre-determined ergonomically favorable and unfavorable postures (**Figure 1)**. The favorable posture included arm rests and a neutral neck angle while the unfavorable posture involved a greater scope angle, no arm rests, and increased neck flexion. The order of the positions was randomized. Participants briefly oriented themselves with the equipment before performing the task, which consisted of touching 10 marked areas along the simulated vocal folds. Participants performed the task for 15 minutes in each position with a 15 minute break in between.

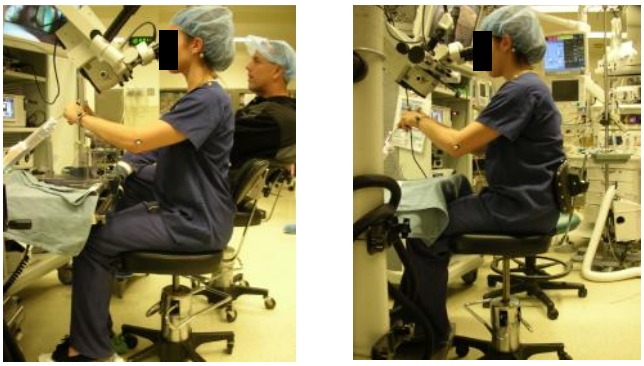

Figure 1. Laryngoscopy simulator and favorable (left) vs. unfavorable positioning set-up.

During data collection, pictures were taken of the participant to be analyzed by the Rapid Upper Limb Assessment (RULA), where lower RULA scores on a scale of 1 to 7 represent a lower risk of upper extremity MSDs [4]. At the end of the task, participants also completed questionnaires where they rated their discomfort in different areas of their body on a scale of 1-10 where 1 was no pain and 10 was the worst pain possible.

DATA PROCESSING The raw sEMG signals were collected at 2000 Hz, the mean was removed, and the signal was bandpass filtered with cutoff

frequencies of 10-400 Hz. The signal was then downsampled to 1200 Hz. Joint Analysis of EMG Spectrum and Amplitude (JASA) was used to quantify fatigue, as defined by Luttman, et al. [3]. The signal was rectified and processed with a moving average filter with a window of 400 ms (no overlap) [3]. The EA was quantified by calculating the mean of the filtered signal every 10 seconds and normalized using the maximum EA during the MVC. EA was thus expressed as the percentage of maximum EA. For the frequency analysis, the power spectral density was calculated using a fast Fourier transform. The resulting median frequency (MF) was calculated, as defined by Stulen and De Luca, every five seconds [5]. A regression analysis was performed on the resulting time series of EA and MF. The slope values for each EA and MF regression were plotted as x- and y-coordinates, respectively. Values that fell in the lower right quadrant indicated a positive slope for EA (increase) and a negative slope for MF (decrease) over time, indicating fatigue [3].

RESULTS More than half of the participants had more fatigued muscles in the unfavorable position; the majority exhibited fatigue in the upper trapezius and tricep muscles (**Table 1**). The average RULA scores for the favorable and unfavorable positions were 3.1 ± 0.3 and 3.8 ± 0.6, respectively, out of 7. On average, participants reported greater pain in the unfavorable position, as seen in **Table 2**. Surgeons in an ergonomically favorable position out-performed those in an unfavorable position. However, as years of experience increased, there was a lesser difference between positions, as seen in **Figure 2**.

Table 1. Participants demonstrating fatigue based on JASA.

Muscle	Favorable	Unfavorable
Lower Trapezius	4	5
Middle Trapezius	2	2
Upper Trapezius	4	8
Cervical Trapezius	5	7
Triceps	4	9
Anterior Deltoid	5	4
Extensor Carpi Radialis	3	2

Table 2. Results of pain questionnaire for dominant side.

Location	Favorable	Unfavorable
Posterior Neck	1.8 ± 1.2	2.3 ± 1.2
Anterior Shoulder	2.1 ± 1.2	4.2 ± 2.6
Posterior Shoulder	2.8 ± 2.2	4.7 ± 2.7
Posterior Upper Arm	1.8 ± 1.1	2.3 ± 1.4
Posterior Lower Arm	3.2 ± 1.3	3.1 ± 1.7

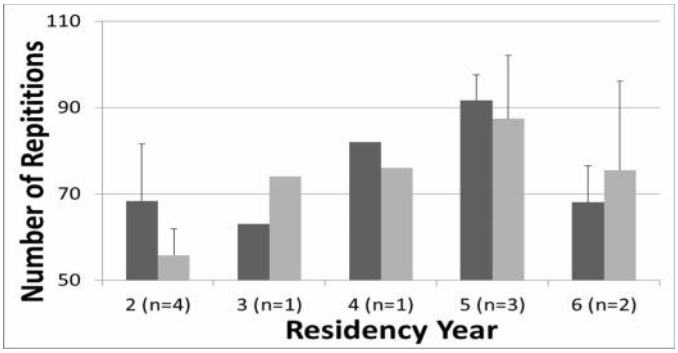

Figure 3. Repetitions of task performed in each position.
■=Favorable ■=Unfavorable

DISCUSSION When surgeons favor poor ergonomic positioning in order to avoid orientation with new equipment or to maximize range of motion, they put themselves at risk for developing MSDs. Similar to the results shown by Dorion and Darveau, we observed a correlation between increased occurrence of micro-breaks, such as rolling the shoulders, and time spent in the unfavorable posture [6]. Micro-breaks taken during long tasks temporarily allow increased blood flow and relieve fatigue. Thus, more micro-breaks correlate with the greater need to immediately relieve fatigue, indicating uncomfortable positioning [6]. Our data suggests that arm rests and a neutral neck angle cause less pain and fatigue and increase productivity. However, as residency year increases, surgical positioning does not seem to have as extreme of an effect on performance. This indicates that greater experience in the profession increases the surgeon's ability to perform, even under non-ideal circumstances.

REFERENCES

1. Statham et al. *The Laryngoscope* **120**, 297-305, 2010.
2. Gandavadi et al. *Br Dent J* **203**, 601-605, 2007.
3. Luttmann et al. *Int J of Industrial Ergonomics* **25**, 645-660, 2000.
4. McAtamney et al. *Ergonomics* **24**:2, 91-99, 1993.
5. Stulen et al. *IEEE Transactions of Biomedical Engineering* **BME-28,** 515-523, 1981.
6. Dorion et al. *Annals of Surgery* **257**: 2, 256-259, 2013.

ACKNOWLEDGEMENTS

Participants were tested in the operating room of the University of Pittsburgh Medical Center's Montefiore Hospital. Funding was provided by University of Pittsburgh Department of Otolaryngology. We would also like to thank Arash Mahboobin and Nancy Baker for assistance with data processing.

Magic Angle Enhanced Microscopy of Fibrous Ocular Structures

Tyler Pirkle, Leon Ho, and Kevin Chain
Neuroimaging Laboratory, McGowan Institute of Regenerative Medicine
University of Pittsburgh, PA, USA
Email: tbp12@pitt.edu Web: http://www.kimlab.pitt.edu/

INTRODUCTION

The sclera is a collagenous ocular structure which shares the same structural characteristics as tendon. Like tendon, studies suggest the sclera is not a static container, but rather a dynamic tissue capable of altering its composition and biomechanical properties in response to changes in the visual environment. The role that such mechanical behavior plays in eye diseases such as glaucoma and myopia remains poorly understood [1,2] due to the lack of non-invasive techniques able to access and monitor the ocular fibrous microstructures globally, longitudinally, and reliably without altering the biochemical environment.

T_2 relaxation is a tissue specific property responsible for generating contrast in magnetic resonance images. Signal intensities are due to the relationship of water to collagen fiber structure. Intensities can vary from extremely low, as observed in bone, or exceptionally high, as observed in blood [3]. Dense, fibrous structures such as tendon or sclera exhibit little to no MRI contrast because of rapid T_2 relaxation brought on by water's intermolecular dipolar interactions. Magic angle enhancement poses a detour around these interfering dipolar interactions.

Past experiments have demonstrated an orientation dependency for signal intensity of fibrous structures [3]. These studies show that orienting the collagenous structures to the magic angle of 54.7 degrees from the main magnetic field decreases dipolar interactions resulting in longer relaxation times, which ultimately yields higher signal intensity. This study is aimed to evaluate the angular dependence phenomenon in tendon and sclera samples for the purpose of potentiating a possible in vivo technique to monitor degeneration of fibrous ocular structures.

METHODS

Sheep tendon and sclera samples were positioned at different orientations to the main magnetic field B_o while scanned using 9.4T Varian MRI. Air Motor Control, engineered by a collaborator at the University of Georgia Robotics Lab, was used to precisely rotate the sample relative to the main magnetic field. Signal intensity data was collected from surface and volume coils. The custom surface coil was designed for high sensitivity, while the volume coil was used to rid of prevalent artifacts at the expense of sensitivity.

The sheep tendon sample was formed into a u-shape and placed in 2% agar. The purpose of the u-shaped tendon was to allow a more convenient visualization of the angular variation. Bending the tendon in this manner ensured more accurate results by allowing one image to capture all tendon fibrils with ranging orientation without the need to reset the sample.

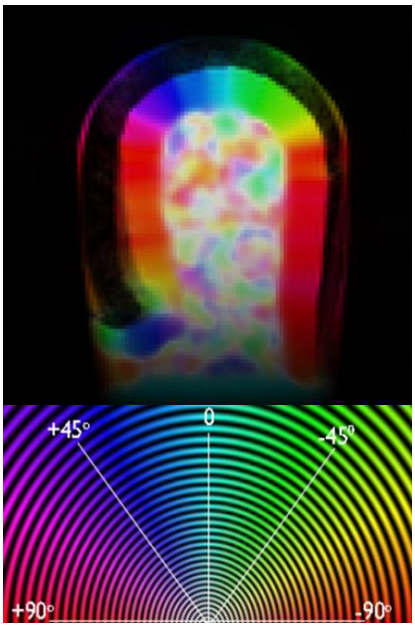

Figure #1 shows a 0 to 180 degree range of fibril orientation. Red denotes perpendicular to the main magnetic field B_o. Blue and green regions are suspected to exhibit the magic angle enhancement.

Figure #2 displays sample ROIs with their corresponding T_2* values. The magic angle enhancement is visually and numerically observed for both 55 and (-)55 degrees.

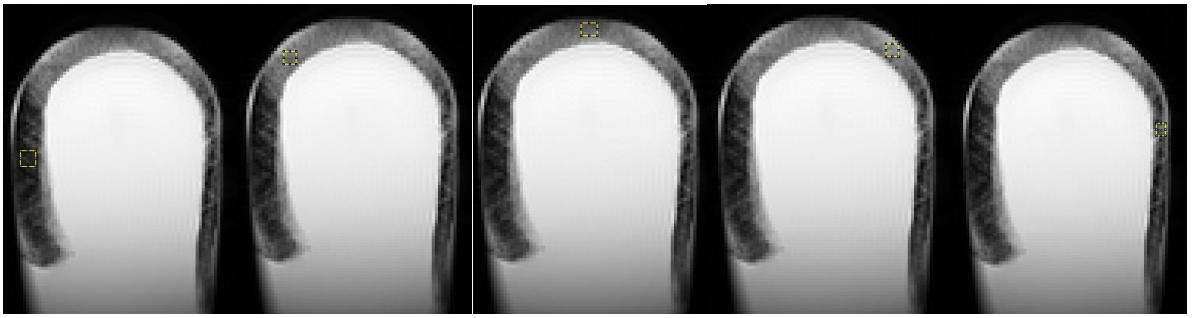

B_0

90 Degrees	55 Degrees	0 Degrees	(-)55 Degrees	(-)90 Degrees
T2*: 4.79	T2*: 6.48	T2*: 2.49	T2*: 8.84	T2*: 6.90

DATA PROCESSING

Matlab was used to convert the raw data files into an ImageJ compatible format. ImageJ calculated the intensity values for the selected regions of interest. These intensity values were organized and evaluated in Excel. Excel allowed graphical representation of our data while also calculating the fitted trendline needed for T_2* analysis.

RESULTS

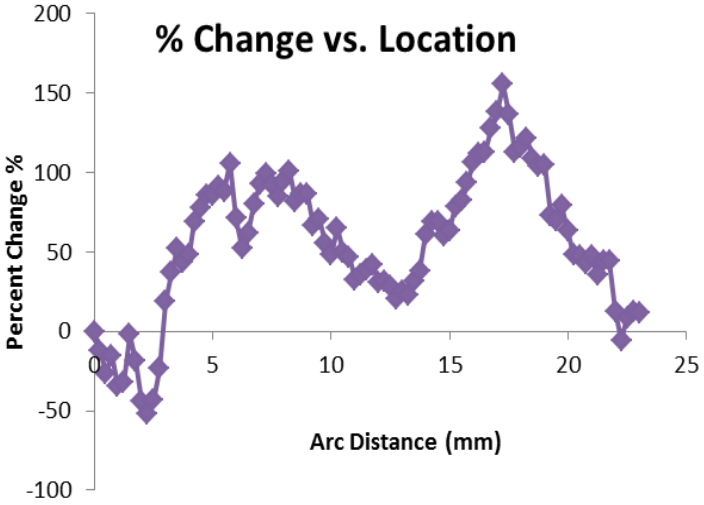

Figure #4 shows the percent change relative to the 90 degree orientation. At the latter magic angle, (-55) degrees, enhancement reaches a maximum of 155% percent change. Minimum values near 0% change are reached at 90, 0 and (-) 90 degree orientations. The curved line ROI helps demonstrate a smooth fluctuation between these orientations. The purpose of this graph is to show the predicted slopes and troughs of signal enhancement relative to the orientation of the tendon.

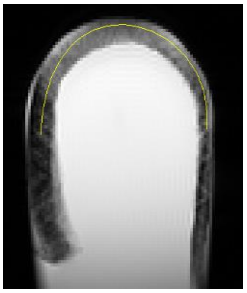

Figure #3 shows the percent change of intensity while varying the degree of orientation. The ROI in this case is a smooth curved line.

Observing *Figure #2* helps visualize and numerically demonstrate the regions of magic angle enhancement. The data extracted from the shown regions of interest (ROI) also indicate a significant increase in T_2* signal intensity. It may be important to note the lowest signal achieved occurs when tendon fibril orientation is perpendicular to B_o.

DISCUSSION

We believe this study demonstrates a potential biomarker for cartilage degeneration, more specifically, an in vivo technique to monitor cartilagous structures such as a tendon or sclera. Our data trends are aligned with that of current literature. Magic angle enhancement yields a more accurate visualization of collagen rich tissue by ridding images of previous artifacts and laminar appearance. An accurate visualization of collagen rich structures potentially opens the door for a proper in vivo monitoring technique.

To improve upon the magic angle phenomenon, it may be of benefit to explore the sensitivity of T_1rho values rather than T_2. Kelsey Mountain suggests T_1rho can be calculated using a relatively similar technique to calculating T_2, but yield a more change sensitive variable [3].

By solidifying this study's data, we hope to move on in the same direction and explore the potential of T_1rho as a biomarker for cartilage degradation.

REFERENCES

1. Rada JA, et al. Exp Eye Res. 2006 Feb;82(2):185-200
2. Pijanka JK, et al. Invest Ophthalmol Vis Sci. 2012 Aug 7;53(9):5258-70
3. Mountain, Kelsey et al Magnetic Resonance Medicine. 2011; 66:520-570

ACKNOWLEDGEMENTS

Collaboration from Robotics Laboratory at the University of Georgia

AUTOMATED IMPEDANCE MODELING TO STREAMLINE ANALYSIS OF NEURAL ELECTRODE IMPLANTATION

Andrew Macgregor, Zhanhong Jeff Du, and Xinyan Tracy Cui
Neural Tissue/Electrode Interface Lab
University of Pittsburgh, PA, USA
Email: ajm194@pitt.edu Web: http://www.engineering.pitt.edu/cui/

INTRODUCTION

A key problem facing neural prostheses is inflammation and glial scar formation in the region surrounding the site of electrode implantation [1]. The fibrous tissue encapsulation that is part of the foreign body response attenuates mass and current flow between the electrode and surrounding neural tissue, reducing the efficacy of both neural stimulation and recording. In order to combat the fibrous tissue encapsulation faced by bare metallic electrodes, a variety of surface modification techniques are being explored, including conducting polymers [2]. Analysis of the electrical properties of surface modifications may achieved by measuring impedance at a biologically-relevant spectrum of frequencies to develop an understanding of the advantages and limitations of conducting polymers.

LEVM(Macdonald, 2012) is a numerical least-squares impedance modeling program which allows estimation of parameter values for a mathematical model of an equivalent circuit using spectral impedance data from the physical system of interest. Although LEVM is packaged with a fully functional GUI, the ability to run LEVM in the command line opens the possibility for automation, which is the subject of this project. The automation process has the potential to greatly improve the efficacy and practicability of modeling while simultaneously reducing human bias during analysis.

METHOD

LEVM uses plain text-formatted input/output, which is easily incorporated into MATLAB (MathWorks, 2013), preferred due to its user accessibility. LEVM input files are organized into a header, in which modeling conditions are specified, and a body portion, where the spectral data is included. Lines are fixed-width, allowing LEVM to extract data and parameters based on their position.

In brief, the MATLAB program uses the header from an input file, INFL, which may be edited by the user, and generates a new INFL including data from files selected by the user. There is no limitation to the number of data files except available memory. LEVM is then called, and it generates the output files, PNTOUTL and OUTIN. INFL is rewritten with the updated parameter values from OUTIN and the data is extracted from the next data file selected. A fit quality factor (FQF) parameter is extracted from PNTOUTL to quantitatively determine whether fitting was successful. The FQF threshold selected here was arbitrarily selected on the qualitative basis of fit curve/data similarity.

To demonstrate the time saving advantage of automating this process, curve fitting and data analysis were carried out on data acquired from a different project in this lab. The data in question was from a 16-channel microelectrode array implanted in vivo over the course of 11 days prior to histological analysis. Impedance data were fitted to an equivalent circuit consisting of a series combination of a Randles circuit and a ladder network (Figure 1).

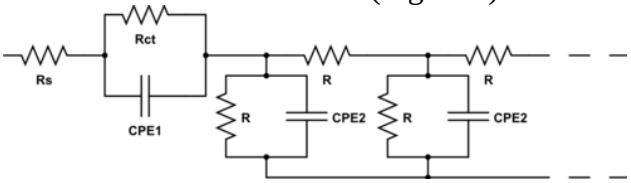

Figure 1: Equivalent circuit for impedance modeling of individual electrodes in a 16-channel microelectrode array during subacute implantation.

The Randles circuit accounts for solution

resistance (Rs), capacitive effects of the double layer(CPE1), and a charge transfer resistance(Rct) to faradaic current. The ladder network models the effects of encapsulation of the electrode(R, CPE2). Initial guesses for circuit parameters were selected from those which previously produced a successful fit.

RESULTS

Spectra were fitted to the equivalent circuit above, and the parameters Rct, Ccpe1, Pcpe1, R, Ccpe2, and Pcpe2 set free as part of the fit. In analysis, the Ccpe1 of all 16 channels recorded on each day were averaged and plotted with respect to time to observe time-dependent changes as the host tissue response progresses (Figure 2).

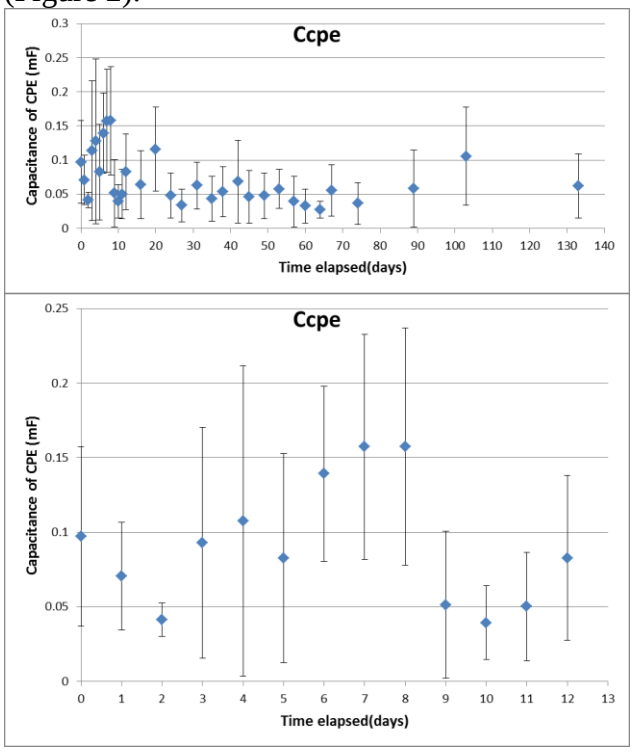

Figure 2: Average capacitive behavior of the Randles CPE. Error bars denote standard deviation(top). Expanded view of subacute period of same (bottom).

Fitted spectra with FQF outside the target threshold were discarded along with obvious outliers. In the first 7 days following implantation, Ccpe1 follows a generally positive trend, though it appears to drop again and remain constant from day 24 to day 74.

DISCUSSION

This paper presents the analysis of a single parameter of an equivalent circuit describing a 16 channel microelectrode array during subacute implantation. The software presented in this paper enables the rapid processing of large volumes of data efficiently. Manual determination of equivalent circuit model parameters is a task which can take approximately two weeks. Using the automation technique described above, that time may be reduced to approximately two days by allowing for many models and initial conditions to be explored in a short time.

The fit produced by the software shows a relatively high quality on the majority of the data set. It should be noted that LEVM does not produce an adequate model if too many parameters are free during fitting, and further analysis with fixed parameters may show the initial assessment of parameters to be confounded by too many degrees of freedom.

REFERENCES

[1] Turner et al. *Exp Neurol*. 156(1):33-49. Mar 1999.
[2]Luo et al. *Biomaterials.* 32(24):5551-7. Aug 2011.

ACKNOWLEDGMENTS

Data was acquired in the Neural Tissue/Electrode Interface Lab, University of Pittsburgh.

PEDOT/GO CARBON FIBER MICROELECTRODE FOR DOPAMINE DETECTION

Linn Zhang, Cassandra Weaver, Tracy Cui
Neural Tissue Engineering Laboratory, Department of Bioengineering
University of Pittsburgh, PA, USA
Email: LIZ55@pitt.edu, Web: http://www.engineering.pitt.edu/cui/

INTRODUCTION

Dopamine (DA) sensing has become an important emerging technology due to the regulatory role of DA signaling in neurological diseases such as schizophrenia, addiction and Parkinson's[1,2]. However, due to its low concentration in the CNS relative to coexisting species such as ascorbic acid (AA), DA can be difficult to detect accurately. When using traditional electrodes, the recorded oxidation potentials of DA and AA are so close that their voltammetric responses often overlap, causing an interfering signal from the AA[6].

The biologically compatible, structurally robust carbon fiber microelectrode (CFME) offers a superior alternative to the traditional electrode. CFMEs have already been extensively electrochemically characterized. They are relatively inert and resistant to fouling, while also showing good detection of catecholamines like DA[4]. Furthermore, they are 7μm in diameter, making them less intrusive and dmazing than conventional electrodes to delicate brain tissue. The deposition of a biocompatible conducting polymer (CP), such as poly(ethylenedioxythiophene)/graphene oxide (PEDOT/GO) composite, onto the surface of the CFME further improves the electrode's sensitivity toward DA. PEDOT has been shown to increase the separation of AA and DA peaks, thus reducing the interference from AA and increasing the precision of the DA sensing[5].

The addition of the GO nanoparticle dopant to the PEDOT CP further increases the mechanical strength of the film as well as the sensitivity toward dopamine through π- π interactions. The sensing capacity of the CFME, used in conjunction with fast scan cyclic voltammetry (FSCV) and the PEDOT/GO composite, is optimal for use in identifying small and rapid changes is essential for the detection of DA *in vivo* due to its continuous fluctuation in the brain. In this study, we will characterize the DA sensing ability of the PEDOT/GO film on CFMEs *in vitro* to further the advancement of a tool that will help us elucidate the effect of DA in the brain *in vivo*.

METHODS

Custom-made CFMEs consisted of carbon fibers (7μm diameter) threaded through tapered borosilicate glass capillaries filled with mercury. All electrochemical procedures were carried out with a three-electrode setup with a CFME working electrode, Ag/AgCl reference electrode and a Pt counter electrode using a Gamry Potentiostat, FAS2/Femtostat (Gamry Instruments). The CFMEs were modified by electrodepositing PEDOT/GO from a solution of 0.01 M EDOT and 5 mg mL^{-1} GO, using multiple parameters (3.5 nA 15s or 30s, 5 nA for 15s or 30s) with chronopotentiometry. FSCV experiments carried out in solutions of 10 μM DA were used to evaluate the electrocatalytic activity of the PEDOT/GO modified CFME toward DA. The electrode potential was swept from -0.5 V to 1 V at 400V/s and the oxidation peak and location values were evaluated.

RESULTS/DISCUSSION

As seen in Figure 1, PEDOT/GO-modified electrodes pass at least six times more current than the bare CFME at the DA oxidation peak location,

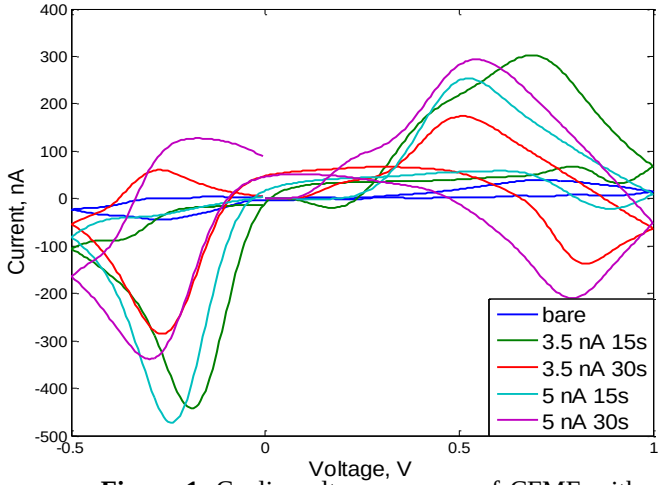

Figure 1. Cyclic voltammograms of CFME with various PEDOT/GO coatings in DA solution (n=3 for each group), using FSCV.

while all but the thinnest film (3.5 nA for 15s) show an oxidation peak shifted to a lower voltage when compared against the bare CFME.

The shift of the oxidation peak is likely due to a faster oxidation reaction facilitated by interactions between the PEDOT/GO film and DA molecules. The DA oxidation peak of the film deposited by 3.5 nA for 15 s may not exhibit the same shift due to the thinner, less homogenous layer of film on the surface of the CFME. The film deposited at 5 nA 15s had narrowest oxidation peak and the best specificity for DA relative to its peak value, making it the most promising possibility for *in vivo* sensing with the least amount of interference from AA.

For all further testing, only the electrodes fabricated with chronopotentiometry at 3.5 nA and 5 nA at 15s were considered since they showed a better peak definition and specificity for DA using FSCV. Figure 2 shows the comparison of electrodes coated with PEDOT/GO and PEDOT doped with polystyrene sulfonate (PEDOT/PSS), which is another commonly used CP film well characterized in literature.

The slow scan cyclic voltammogram differs from the FSCV in that the DA response appears smaller. Even so, the electrode coated with the PEDOT/GO film has a larger charge storage capacity than either the bare or PEDOT/PSS coated electrode. Furthermore, the PEDOT/GO electrode gives the most the most DA specific response.

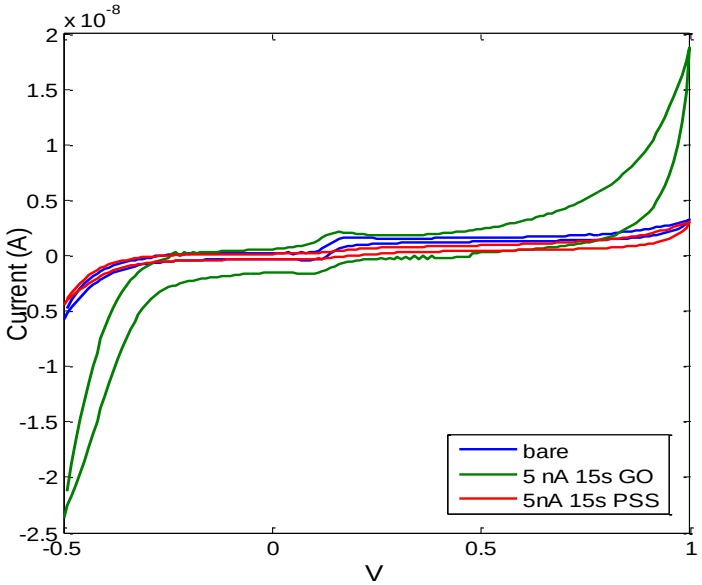

Figure 2. Cyclic voltammograms of CFME coated with PEDOT/GO and PEDOT/PSS with chronopotentiometry at 5 nA and 15s using Gamry slow scan (n=4).

REFERENCES

CFMEs coated with PEDOT/GO film offer improved sensitivity toward DA detection over bare sensing electrodes. To further characterize the film on the CFME and its sensing capabilities toward DA, the electrodes will be tested in solutions of DA and AA with concentrations that mimic those found *in vivo*. The results thus far suggest that the PEDOT/GO coated CFME can be implemented *in vivo* and help further our understanding of DA's role as a neurotransmitter in the brain.

REFERENCES

1. A. Galvan TW. Pathophysiology of parkinsonism. *Clinical Neurophysiology*. 2008;119:1459-1474.

2. R.M. Wightman LJM, A. C. Michael. Detection of dopamine dynamics in the brain. *Analytical Chemistry*. 1988;60:769A-779A.

3. F. Gonon MB, R. Cespuglio, M. Jouvet, J. F. Pujol. In vivo electrochemical detection of catechols in the neostriatum of anaesthetized rats: dopamine or DOPAC? *Nature*. 1980;286:902-904.

4. M. L. Huffman BJV. Carbon-fiber microelectrodes for *in vivo* application. *Analyst*. 2009;134:18-24.

5. S. R. Jeyalakshmi SSK, J. Mathiyarasu, K. L. N. Phani, V. Yegnaraman. Simultaneous determination of ascorbic acid, dopamine and uric acid using PEDOT polymer modified electrodes. *Indian Journal of Chemistry*. 2007;46(A):957-961.

ACKNOWLEDGEMENTS

This research was funded by the University of Pittsburgh, Swanson School of Engineering and Neural Engineering Laboratories.

FURTHER CHARACTERIZATION OF ELECTRICALLY INDUCED CONTRACTILITY OF INTACT EMBRYONIC TISSUES ON A MICROELECTRODE ARRAY

Eric Weston[12], Deepthi Vijayraghavan[1], Cassandra Weaver[2], X. Tracy Cui[2] and Lance Davidson[1]
[1]Morphogenesis and Developmental Biomechanics Laboratory, Department of Bioengineering
[2]Neural Tissue Engineering Laboratory, Department of Bioengineering
University of Pittsburgh, PA, USA
Email: ebw8@pitt.edu

INTRODUCTION

Epithelial tissue contractility plays critical roles in developing embryos. In the fruit fly *Drasophila*, for example, epithelial contraction drives ventral furrow formation, while in vertebrates, epithelial contraction drives neural tube closure [1,2]. The ability to induce controlled contractions within the epithelium can provide further insight into both cellular and molecular mechanisms that regulate how contractions shape a developing embryo. Previous whole embryo studies show that contractions can be induced via chemical perfusion of ATP or electrical stimulation [3]. We have also previously shown neuroelectrophysiology techniques, mainly planar, sixty-four electrode microelectrode arrays (MEAs), are a viable option for electrical stimulation of isolated epithelium. This method allows the experimenter to observe contractile effects of more localized stimulation.

Our study focuses on further characterization of contractility within *Xenopus laevis* animal cap explants. These surgically isolated tissues include one epithelial cell layer and up to two layers of mesenchymal cells underneath it. We characterize two types of contractile responses, one being a small, local contractile response close to the point of stimulation and a second large, contractile "wave" response that propagates throughout the tissue. We also show that a contractile potentiation response exists within the tissue after elicitation of a large response. Finally, we characterize contractility of isolated cell layers from the animal cap.

METHODS

Animal cap explants were microsurgically removed from gastrula stage *Xenopus laevis* embryos. The tissues were transferred to a well of a MEA previously coated with polyethylenimine and fibronectin. Explants were gently massaged down onto the MEA surface (Figure 1) and allowed to heal, adhere and spread for .5 hours. Contractions were induced via the Autolab or MED64 stimulator, both available from the NTE lab, and were visualized using a stereomicroscope equipped with a CCD camera acquiring images in time-lapse mode. Both current pulses for 5 ms and voltage controlled square waves (positive, then negative voltage in equal 2.5 ms increments) were used depending on the nature of the particular experiment at hand. Voltage, current, and impedance measurements were recorded as a source of comparison among trials.

IMAGE PROCESSING

Most image stacks were analyzed qualitatively during experiments. After each experiment, however, the subtraction of background noise allowed for an even clearer qualitative understanding of the results. To quantitatively characterize contraction we utilized a strain mapping technique using BunwarpJ, a plugin in ImageJ and Fiji. This plugin calculates pixel displacement between two individual frames or between a set number of frames for an entire image stack. The displacements can then be converted into multidirectional strain maps. Additionally, we calculated the percent area of contraction within the tissue by measuring freehand area selections of both the contractile area and the total tissue area in ImageJ.

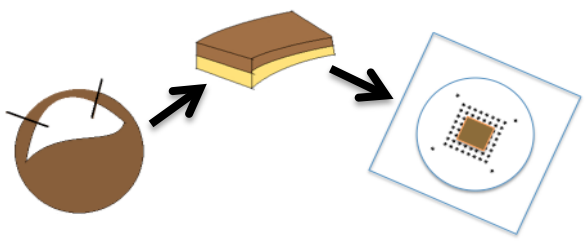

Figure 1. Method of animal cap placement

RESULTS AND DISCUSSION

Characterization of timing and magnitude of contractile response

We first observed tissue contraction in response to varied amounts of voltage. For all trials, the tissue was stimulated through an electrode with a 20 kΩ impedance at 1kHz. The smallest observable contractile response corresponded to a 0.5 V delivery, representing an average current delivery between 0.6-0.7 μA in magnitude and covered an average contractile area of 5.0%. A wave-like response, in which the contractile response propagated throughout the entire animal cap, was elicited with a 3.5 V delivery, representing an average current of 30 μA. The average contractile response lasts for 8-10 minutes in either case.

Voltage delivery utilized square waves so as to not deposit too much charge on the electrode surfaces. Therefore, a positive and negative current value was recorded for each trial. Negative current and voltage has been shown to elicit the same response in animal cap tissue, so the polarity of this delivery did not matter. The positive and negative recorded magnitudes of current were generally very similar during each trial.

Characterization of a potentiation response within the tissue

As a control, 0.5 V was delivered and imaged for ten minutes. After this time, 3.5 V was delivered so as to depolarize every cell within the tissue. Then, after a set "recovery time," the cap was stimulated with 0.5 V once more. When stimulated again within 30 minutes of the 3.5V pulse, a larger contractile response was observed than that of the control. Quantitatively, the "potentiated" response for varied recovery times was compared using contractile percent area (% CA) calculations and is shown in Table 1 below.

Recovery Time (minutes)	Control % CA	"Potentiated" % CA
15 minutes	3.98%	31.2%
20 minutes	3.98%	28.4%
30 minutes	4.55%	7.43%

Table 1. Comparison of responses before and after depolarization of all cells at varied recovery times

These preliminary results suggest that once a cell has depolarized and shown a contractile response, it seems to more readily contract, even when a lower current/voltage combination is delivered, even up to thirty minutes later. The mechanism for why this response exists, however, is unknown.

FUTURE DIRECTIONS

The individually addressable electrodes of the MEA enable parallel stimulation and electrical recording with high spatial resolution and may be used to record the propagation of electrical signals throughout an animal cap explant. This is one of the major reasons that MEAs were chosen as the method for electrical stimulation and is vital for further characterization of the induced contractile response. It is likely that stimulation at one electrode will create a recordable electrical signal that propagates within the tissue several cell diameters away from the stimulation point. Unfortunately, we have encountered several roadblocks in trying to record signals. Noise levels on the MEA surface are too high to acquire any useful data. Additionally, we are still unsure exactly what we are looking for as a response during MEA recording. All of these problems must be resolved before recording can proceed. Once recording capabilities are achieved we can then investigate whether different contractile stimuli such as chemical stimulation also lead to electrical signal propagation through the tissue.

Finally, our laboratory has developed a new imaging processing technique that quantifies area changes on a user set grid. It tracks a pixel at each vertex of the grid and the resulting area changes of the quadrilaterals within grid over time. Such a technique will be helpful because it will show where on the tissue contraction takes place at different times, there will no longer be user bias surrounding percent contractile area calculations, and the data will easily be exported as a .txt file and imported into Microsoft Excel.

REFERENCES

[1] Leptin, M. et al., Development (1990) 110(1): 73-84.

[2] Zhou J., et al., Development (2009) 136(4): 677-688.

[3] Joshi SD, et al., Exp Cell Res (2009) 316: 103-114

DEVELOPMENT OF 6 DEGREES OF FREEDOM CLAMPS FOR THE STUDY OF HUMAN SHOULDER- AND KNEE-JOINT-COMPLEXES

Jonathan Brokaw, R. Matthew Miller and Richard E. Debski
Orthopaedic Robotics Laboratory, Department of Bioengineering, University of Pittsburgh
Email: jdb122@pitt.edu

Introduction

The understanding and repair of musculoskeletal injuries in the human body is a constantly developing field. Our knowledge of tears in ligaments and muscle tissues of the knee and shoulder-complexes of humans stems primarily from clinical data of tear patients, as well as cadaveric tissue studies. With a significant portion of adults having experienced some kind of rotator cuff tear or knee injury in their lifetimes the need for improved injury prevention and repair techniques is very great .

The primary means of testing soft tissues under failure conditions is the use of materials testing machines. In order to make the most of results gained from these tensile tests all loads should be applied in as accurate an anatomical position as possible in order to offer a realistic injury simulation. To accommodate this need, clamps were developed to allow accurate positioning of cadaveric samples with as many degrees of freedom (DoFs) as possible. Clamps were updated for the human shoulder and designed in full for human knee tests.

Methods

Original Shoulder Clamps in a Ligament lab

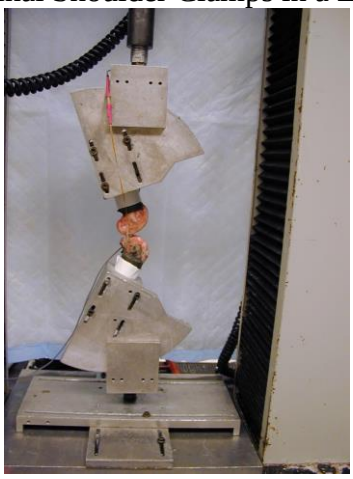

The clamps required a minimum of 6 Degrees of Freedom in order to allow a variety of anatomical positions in tests. Woo et. al. provided examples of the types of freedoms needed, as well as prior clamp-styles used in research experiments. The three translational degrees necessary were medial-lateral, anterior-posterior, and proximal-distal. The rotational degrees of freedom are internal-external, flexion-extension, and varus-valgus rotations. [1]

The designs were formed using the CAD software Solidworks(SW). The software allows users to constrain and simulate clamp functionality prior to machining. After several revisions the final SW drawings of the shoulder clamps were tendered to several machine shops for quotes.
The human shoulder clamp designs were to be updated to account for wear on materials as well as adapting the designs to fit the new Instron machine. The designs were based on clamps previously developed by Dr. Debski.

The knee clamps were developed using the same program learned to develop the shoulder clamps. The initial aim of the knee clamp design was to allow a full 6 DoFs, while reducing the moment acting on the load cell component of the Instron machine so as to prevent fracturing of the load cell. The maximum force capacity of the load cell is 5000 Newtons. The load cell capacity needed to include the force caused by the mass of the top section of the clamps, as well as the 2500N ultimate failure load of potential knee tests. The need to align the tissue to be tested directly beneath the load cell posed a particularly challenging problem as it required departure from designs previously used in tensile testing apparatuses with similar goals [2].

Results

The human shoulder clamps were updated to allow for less wear on the clamps themselves. This was accomplished by the addition of grommets to the

enhanced clamps so as to prolong their longevity. Along with the shoulder clamps soft tissue adaptors were developed to allow individual ligaments and tissues to be tested in the Instron independent of the bone or joint-complexes they are naturally adhered to. These clamps and adaptors were submitted to the Pittsburgh Foundry for machining and will be complete within two weeks.

The new human knee clamps used 10 DOFs by allowing medial-lateral, internal-external, anterior-posterior, flexio-extention, and varus-valgus freedoms on both the tibial and femoral components of the apparatus. The initial design intent also included minimizing the number of fixation points within the clamps The increased positioning flexibility of these clamps allows a substantial range of potential positions for use in knee testing protocols.

Solidworks Drawing of New Human Knee Clamps

Discussion

The shoulder clamps and soft tissue adaptors allow the desired degrees of freedom to be present for tests. However, the designs of the shoulder clamps also require that several screws be fixed into place before tests can occur. The time required to fix the clamps at the desired flexion angle, as well as setting the joint-complex into the clamps, proves to be a significant delay to protocols, which is compounded by the time required for disassembly.

The knee clamps avoid the issue of increased assembly time by minimizing the number of necessary attachments between pieces, requiring only that each component of the clamps be fixed in relation to the needs of each particular protocol's anatomic positioning. The corollary of the loss in fixation points is that the clamp components are fairly bulky and require more material. While the newly designed clamps are developed to be durable and able to take standard wearing, the use of the rotational components in tests may eventually require that the rotary bearings used to fix angles of flexion-extension and varus-valgus rotations be replaced.

Conclusion

The equipment designed this summer will allow the Orthopaedic Robotics Laboratory to study a variety of injuries and material components of the human shoulder and knee. The clamps allow material testing in the lab to commence and studies with developed protocols to be implemented. The development of the clamps allows the lab to move on with cadaveric studies and confirming clinical findings.

The ORL will continue to develop its capacity for new protocols with the development of a laser micrometer for measuring the cross-section of tissues and new clamps to model desired failure mechanisms. The equipment so developed will continue to help maximize injury prevention while minimizing the costs and time associated with tears and injuries of the human musculoskeletal system.

Acknowledgements

The design and development of this equipment was funded in part by the Summer Research Internship program of the Swanson School of Engineering and the Department of Orthopaedic Surgery. The author thanks Dr. Richard Debski, Ph.D. candidate R. Matthew Miller and the members of the Orthopaedic Robotics Laboratory for their contributions and support.

Reference

1.Woo S. LY, Hollis JM, et al: Tensile properties of the human femur-ACL-tibia complex: The effects of Specimen age and orientation. American J. Sports Med. 19 217-225, 1991

2. Lyon RM, Woo SL-Y, Hollis JM, et al: A new device to measure the structural properties of the femur-anterior cruciate ligament-tibia complex.
J Biomech Eng 114 350-354, 1989

EVALUATION OF FUNCTIONALITY OF MODIFIED RED BLOOD CELLS FOR INTRAVASCULAR DRUG DELIVERY

Ryan Mooney, Jill Anderson, Hironobu Murata Ph.D., , Richard Koepsel Ph.D., and Marina Kameneva Ph.D.
McGowan Institute of Regenerative Medicine, Department of Bioengineering
University of Pittsburgh, Institute for Complex Engineered Systems, Carnegie Mellon University, Pittsburgh, PA, USA

INTRODUCTION

Drug delivery using red blood cells (RBCs) as biocompatible vehicles is a promising novel technology which may enhance effectiveness and safety of intravascular drugs. Camptothecin is an antitumor drug that acts by inhibiting DNA topoisomerase I.[1] Despite its potential, camptothecin has the drawback of having low water-solubility.[2] DMSO is one of the few solvents that is able to get camptothecin into solution. It has been proposed that by incubating camptothecin with DMSO, it can be attached to NHS_βAlaPDMAA_Rodamine B polymer that can in turn be attached to RBCs (specific technological process developed at Russell Laboratory, ICES, CMU). If successful, this method would provide opportunity to use patient's own RBCs for treatment. The attachment to RBCs will allow camptothecin (or other similar drugs) to be delivered throughout the vascular system to the targeted cancer cells with no extravasation and at much lower concentrations. One important issue for application of modified RBCs is preservation of their functionality. The major objective of this research project was assessment of functionality of the modified RBCs via evaluation of their morphology and deformability.

METHODS

Commercial human RBCs were purchased from Valley BioMedical Products & Services, Inc. RBC modification was accomplished by first attaching a camptothecin monomer to a βAlaPDMAA_Rodamine B polymer having an NHS end group. This polymer-drug construct was then attached to the surface of RBCs by incubating the drug-polymer complex with RBCs in 1% DMSO. RBCs attached with only the polymer, without the camptothecin, were also analyzed in this study. The modified cells were then washed and viewed under a fluorescent microscope. Since the polymer used for cell modification contained a fluorescent (Rhodamine), it was possible to confirm that the RBCs had been successfully modified. To evaluate deformability of the modified RBCs they were exposed to shear stresses of 1.5, 7.5, and 15 Pa in a Linkam shearing stage, alongside control cells which had not been modified. About 100 pictures were taken at each shear rate analyzed. The samples were then refrigerated and their deformability was analyzed on the day after the modification to ensure deformability had not changed. Control and modified cell morphology was confirmed via Nikon contrast microscope.

DATA ANALYSIS

Cells were analyzed using ImageJ software. For each sample, 200 cells were analyzed at each shear stress on each day of testing. By measuring the major and minor axis of the cells, an elongation index (EI) at each shear stress was calculated using the equation

$$EI = \frac{major\ axis - minor\ axis}{major\ axis + minor\ axis}$$

The EI of the modified cells on Day 1 were compared to the EI of the control cells on Day 1 at each shear rate, etc. The EI of the modified cells on Day 1 were also compared to the EI of the modified cells on Day 2, etc. to ensure that the deformability did not change over time. A student t-test was used in each case.

RESULTS

Figure 1 shows the average EI for the camptothecin modified (n=1), the polymer only modified (n=3), and the control (n=4) at 100, 500, and 1000 s^{-1} on Day 2 of the study. The error bars show that the averages fall in close proximity with each other at each shear rate.

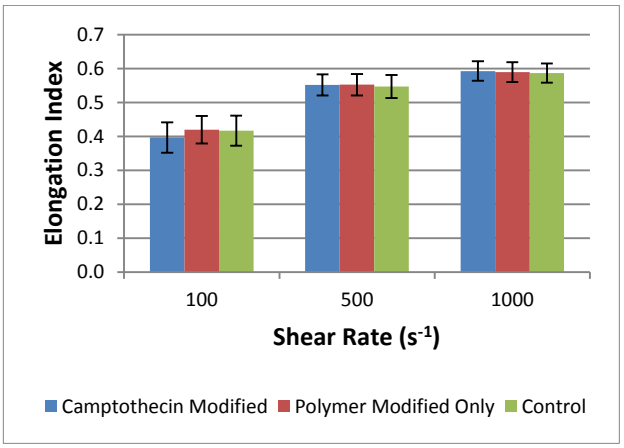

Figure 1: The average elongation index of each sample a day after modification over a range of shear rates with standard deviation error bars.

Figure 2 shows the deformability of each sample over the course of two days at each shear rate. The error bars again indicate little change has occurred in deformability from the day modification occurred until the day after.

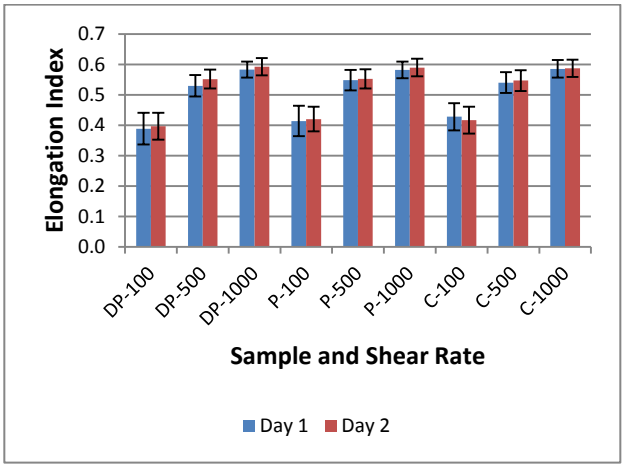

Figure 2: The average elongation index of each sample over a range of shear rates the day of modification and the day after with standard deviation error bars (DP-drug polymer, P-polymer only, C-Control)

Table 1 shows the results of the t-tests done between the average EIs of the camptothecin modified/polymer only modified cells and the control.

Table 1: P Values Obtained Using Average EIs from Each day of Testing.

	Shear Rate					
	100		500		1000	
Sample	Day 1	Day 2	Day 1	Day 2	Day 1	Day 2
Drug-Polymer	0.511		0.657		0.739	
Polymer Only	0.619	0.903	0.346	0.810	0.524	0.899

DISCUSSION

The similar values of the EI for control and modified RBCs at each shear rate demonstrated that the modification of RBCs with the polymer-drug construct did not affect the deformability of RBCs. There was no significant difference between morphology of modified and control cells. This data supports the hypothesis that RBCs can be utilized for efficient intravascular delivery of drugs where the integrity of the modified RBCs is maintained for at least 24 hours after modification.

REFERENCES

1. Hsiang, Yaw-Huei, et. al. "Camptothecin Induces Protein-linked DNA Breaks via Mammalian DNA Topoisomerase I". *The Journal of Biological Chemistry.* Vol 260 Issue 27: pp. 14873-14878, 1985.

2. Saetern, Ann Mari et. al. "Effect of hydroxypropyl-β-cyclodextrin-complexation and pH on solubility of camptothecin*". International Journal of Pharmaceutics.* Volume 286, Issues 1-2: pp.61-68. 2004.

ACKNOWLEDGEMENT

The authors would like to thank Rudolf Hellmuth for his help developing a new image analysis protocol.

AUTOMATED QUANTIFICATION OF INTERSTITIAL AND PERIVASCULAR CARDIAC FIBROSIS IN THE MREN2(27) TRANSGENIC RAT MODEL

Casey Rayburg, Jamie Haney, Sanjeev G. Shroff
University of Pittsburgh, PA, USA

INTRODUCTION

Fibrosis is a naturally occurring process that results from the accumulation of collagen proteins in several tissues throughout the body. While these increases in collagen often occur with age, fibrosis can be aggravated by disorders such as hypertension and upregulated renin-angiotensin-aldosterone system. Hypertension is a prevalent issue in today's society, and studies show that with this disorder, increased fibrosis can lead to damaging effects in cardiac tissues. These rats are designed to overexpress renin, which through activation of the renin-angiotensin system (RAS), subsequently exhibit several symptoms of increased cardiac fibrosis. The mechanisms by which renin causes downstream effects on cardiac fibrosis are due to increased angiotensin (II) as a result of RAS activity. Increased angiotensin (II) is a known mediator of hypertension, and linked to cardiomyocyte hypertrophy, left ventricular (LV) dysfunction, and interstitial cardiac fibrosis.

The aim of this study was to utilize picrosirius red staining to quantify myocardial collagen in the mRen2 transgenic rat and its sex- and age- matched Wistar-Han control rat (WHC). Based on previous knowledge, a good animal model of cardiac fibrosis should demonstrate increased levels of collagen protein in cardiac tissue. Additionally, this study aimed to optimize an automated computer-based algorithm for myocardial collagen content analysis. When paired with functional whole heart data and genetic-level fibrotic expression, this protein-level study will serve to set the stage for future antifibrotic therapy studies in the mRen2 transgenic rat model.

METHODS

Samples of LV from both heterozygous mRen2 transgenic rats (n=4) and WHC rats (n=8) were isolated, weighed, and cut into two cross-sections. Each was stored overnight in 10% formalin solution and embedded in paraffin. These samples were sectioned at 5μm and mounted onto slides in preparation for histological staining. The slides were then deparaffined and washed with xylene before being rehydrated with a descending ethanol gradient. The samples were stained with picrosirius red dye (0.5% in saturated picric acid) for 80 minutes. Following the completion of the stain, slides were then dehydrated through an ascending ethanol gradient and mounted with a coverslip for examination via light microscope (Olympus Provis bright-field microscope).

Bright-field images were collected at 4x magnification on four quadrants of each LV sample. Additionally, representative perivascular images were taken at 20x magnification. The researcher taking the images was blinded to the identity of each sample. Olympus microscopes were set at a predetermined exposure time and transmitted light setting.

ImageJ, a NIH approved image-editing software, was used to process and organize images according to tissue type prior to collagen assessment. Using a custom-developed automated algorithm, images were analyzed based on saturation thresholds that were calculated within bounds set by the algorithm, versus manually-set saturation thresholds. The four quadrants of each sample were combined and the ratio of collagen area to total tissue area was expressed as a percentage. Perivascular measurements were expressed as an average percentage of perivascular tissue area.

RESULTS

Transgenic rats showed a significant increase in interstitial collagen protein expression versus WHC rats, and a tendency for increase in perivascular collagen protein expression. mRen2 rats exhibited an average collagen to total tissue area of 5.95% $\pm$ 1.01% (n=4). This was overall a 67% increase in interstitial collagen content versus WHC rats, which exhibited a ratio of 1.96% $\pm$ 0.06% (n=7); $P = 0.012$

(Figure 1A). Perivascular content showed a slight increase in collagen as a percentage of perivascular tissue area; however, this did not reach statistical significance (mRen2: 28.54% $\pm$ 6.65% *vs*. WHC: 23.05 $\pm$ 0.451%; $P = 0.161$) (Figure 1B).

There was a significant linear correlation between the collagen content values obtained by the two methods, both for interstitial collagen ($R^2 = 0.86$, Figure 1C) and perivascular collagen ($R^2 = 0.74$, Figure 1D) data. There was a difference between the absolute values obtained by the two methods (Figures 3 and 4). However, the Spearman's Rank-Order Correlation (ρ) was highly significant ($P = 0.001$) for perivascular collagen data (ρ = 0.84, Figure 1D), indicating that there was significant strength and direction of association between the two methods. Similar associative strength was observed for intestinal collagen data (ρ = 0.56, Figure 1C); however, the ρ value did not reach statistical significance ($P = 0.07$).

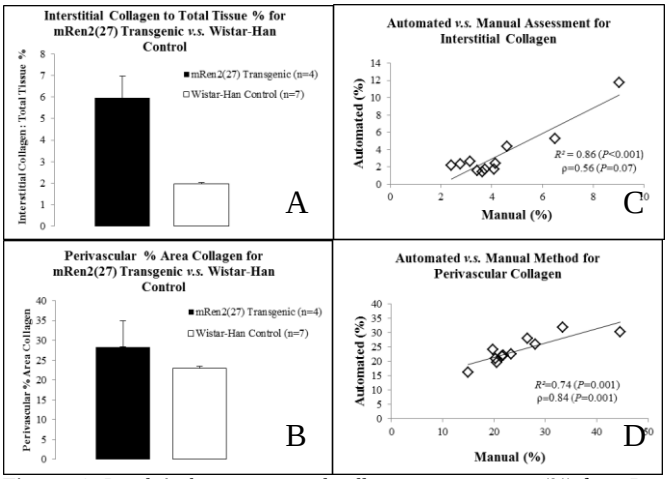

Figures 1: Panel A shows interstitial collagen-to-tissue ratio (%) for mRen2 transgenic rats (n=4) and WHC rats (n=7), **P* = 0.012. Panel B shows perivascular collagen-to-tissue ratio (%) for mRen2 transgenic rats (n=4) and WHC rats (n=7), *P* = 0.161. Panels C and D show a comparison of collagen content data obtained by the two analysis methods (automated and manual) for interstitial and perivascular collagen, respectively. Data from both groups (WHC and mRen2) are pooled together (n=11). R^2: coefficient of determination from linear regression; ρ: Spearman's rank-order correlation.

DISCUSSION

The heterozygous mRen2 transgenic rat model, a proven hypertensive animal in fibrosis research, was compared with WHC sex- and age- matched controls. The purpose behind this study's method was to establish protein-level fibrosis expression in mRen2 rats versus normotensive controls (WHC) using automated methods. Due to the downstream effects of the activated renin-angiotensin system, interstitial collagen protein levels in transgenic rats were significantly higher than in their WHC counterparts. Despite a slight difference in perivascular collagen content, overall change was not significant. While more data is needed to confirm perivascular collagen quantification, this study confirms previous findings that mRen2 transgenic rats exhibit increased interstitial cardiac fibrosis.

ImageJ has often proved useful to researchers as a tool to process and collect data from image based experiments. Within the parameters of this study, this algorithm was optimized to determine collagen in LV tissue samples. As evidenced by the outcomes of this study, statistical analysis showed a significant correlation between the absolute results of both perivascular and interstitial collagen content. Further analysis of rank-order determined a strong association between the automated and manual assessments for perivascular collagen content, and to a lesser degree interstitial collagen content.

Previous studies have measured the cardiac function of mRen2 transgenic rats; however, no conclusive measurements of cardiac dysfunction could be linked to the fibrosis seen in mRen2 LV tissue. This may be due to the variability and complexity associated with cardiac performance measurement techniques (pressure-volume catheter or echocardiography). Future development of credible functional assessment techniques will lead towards an investigation into potential treatments for cardiac fibrosis.

ACKNOWLEDGEMENTS

I would like to acknowledge my advisor Dr. Sanjeev Shroff and my graduate student mentor Jamie Haney for their continued support and fantastic mentoring throughout the semester and the SRI program. I would like to acknowledge those who helped with this study, including the staff at the Center for Biologic Imaging (CBI) and histology department at McGowan Institute of Regenerative Medicine. Lastly, I would like to thank the Excel program for this opportunity.

INCREASING NATURAL VARIANCE TO IMPROVE TRANSFER OF MOTOR LEARNING FROM TREADMILL TO OVER GROUND WALKING

Thomas Rotella
Human Movement Research Laboratory, Department of Bioengineering
University of Pittsburgh, PA, USA
Email: twr4@pitt.edu

INTRODUCTION

Transfer of device assisted motor learning to natural contexts is essential for rehabilitation. Specifically for our study, transfer of split-belt treadmill learning to natural over ground walking is critical to successful rehabilitation. Unfortunately, learning seems to be context specific. Motor learning is tied to the treadmill and does not transfer significantly to over ground walking [1,2]. Young children, however, seem to defy this finding. Young children are able to transfer their learning on the treadmill to over ground walking where as adults cannot. Children are also normally more variable in their gait than adults [3]. Is the higher variability the reason for children's ability to transfer learning or is age the controlling factor? To test this we will attempt to make young healthy adults more variable. If variability is increased in an adult, will transfer of learning from the treadmill to over ground be improved?

METHODS

The study consisted of ten young, healthy adults (25.3 ± 5.5). We used a motion capture system (Optotrak system, NDI corp) to record the kinematics of subjects walking over ground and on the treadmill throughout the duration of the study. In order to make the subjects more variable in their gait we had them walking on the split-belt treadmill with both belts moving at the same speed and responding to a series of pseudorandom computer commands. The computer told subjects to walk with "slow steps", "fast steps", "long steps", or "short steps." This period on the treadmill was labeled variable baseline. Then we began an adaptation period where the belts gradually changed from a 1:1 speed ratio to a 2:1 speed ratio. During the adaptation subjects continued to respond to the pseudorandom computer commands in order to maintain a higher variability. After the adaptation period, subjects walked over ground to test for after effects generated by the split-belt walking experience.

DATA PROCESSING

We used the kinematic data from the motion capture system to calculate phase shift, step symmetry and center of oscillation parameters which are shown to quantify the adaptation and transfer of learning on a split-belt treadmill [4]. Phase shift indicates the temporal relationship between the legs. Step symmetry is a spatial parameter comparing the distance between heel strikes. Center of oscillation indicates the difference in where the legs oscillate with respect to an axis along the trunk of the body.

Transfer was quantified as the mean of the first three steps of over ground walking after the treadmill paradigm (OGafter). To remove any bias the mean of all steps in the baseline over ground walking (recorded before the treadmill paradigm) was subtracted from OGafter. The variance was calculated for the variable baseline condition and the normal baseline condition (no computer commands). The two variances were compared to check for an increase from normal baseline to variable baseline. The ten subjects of this study were compared to 42 other subjects through plotting in Matlab. The data from the 42 other subjects is from Torres-Oviedo et al. (abstract 2010).

RESULTS

First, we observed that subjects did increase their variance from normal baseline to the variable baseline. Figure 1 is a bar plot for a single subject's change in variance for phase shift, step symmetry, and center of oscillation. All p-values were less than 0.05. Figure 2 is a plot of variance vs. amount of transfer for the phase shift condition. Higher variances appear to have higher transfer. The

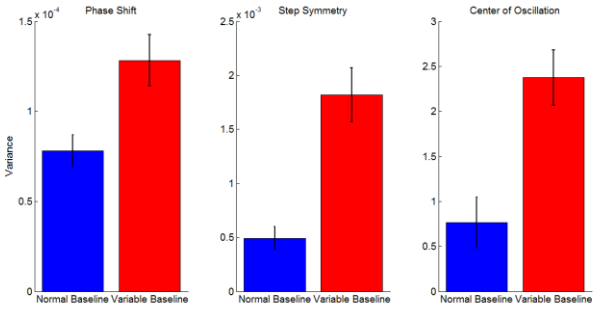

Figure 1: A plot comparing normal baseline variance and variable baseline variance for phase shift, step symmetry, and center of oscillation. The blue bar is normal baseline and the red bar is variable baseline.

markers are color coded for different age groups and the black markers are the subjects from the current study. The R^2 value equals 0.468.

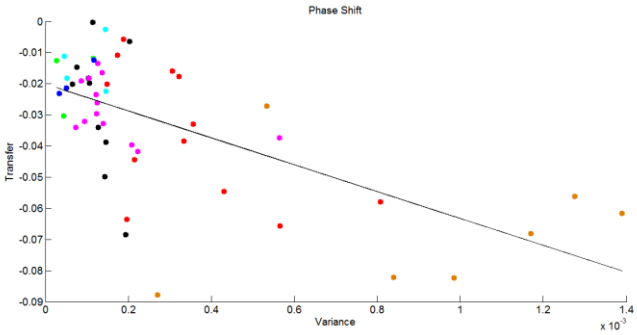

Figure 2: A plot of variance vs. transfer for the phase shift parameter. The black circles are the subjects from this study. The other circles are all of the other subjects from a previous study color coded for age groups. Orange is less than 6 years. Red is 7 to 11 years. Magenta is 12 to 16 years. Cyan is 17 to 21 years. Green is 22 to 26 years. Blue is greater than 26 years.

Figure 3 is a plot of age vs. variance for the phase shift condition. The younger subjects have higher transfer than the older subjects. The subjects from this study (black circles) show similar results to the red age group who are more than a decade younger.

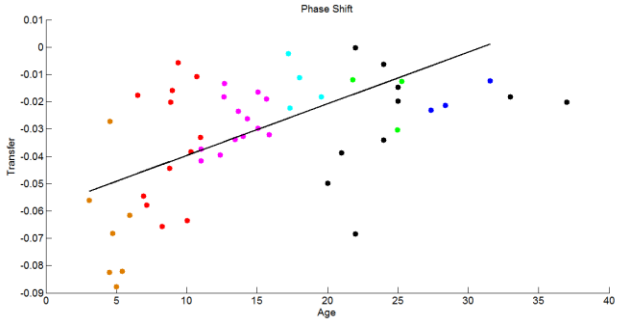

Figure 3: A plot of age vs. transfer for the phase shift parameter. The black circles are the subjects from this study. The other circles are all of the other subjects from a previous study color coded for age groups. Orange is less than 6 years. Red is 7 to 11 years. Magenta is 12 to 16 years. Cyan is 17 to 21 years. Green is 22 to 26 years. Blue is greater than 26 years.

DISCUSSION

Overall the variance of each subject was able to be increased. The ten subjects of this study have variances matching other subjects several years younger but none of the subjects increased their variance to match any of the children. Analysis of the amount of transfer of learning from the treadmill to over ground shows that three or four of our ten subjects have improved their transfer. Similar results were observed for the step symmetry and center of oscillation parameters.

From this study we have learned that it is possible to make an individual temporarily more variable in their gait, though the increase is not large as large as we desired. We have also learned that variance plays a role in how well a subject can transfer motor learning from the treadmill to over ground walking. Further statistical analysis of this data and further collection of new data must be conducted to learn what mechanisms contribute to the ability to transfer learning from one situation to a new situation and if there is an optimal ratio of contributors for maximum transfer.

REFERENCES

1. Reisman et al. *Neurorehabilitation and Neural Repair*, **23(7)**, 735-744, 2009.
2. Torres-Oviedo et al. *Journal of Neuroscience*, **30(50)**, 17015-17022, 2010.
3. Torres-Oviedo et al. *Journal Neurophysiol*, **107**, 346-356, 2012.
4. Vasudevan et al. *Journal of Neuriscience*, **31**, 3055-3065, 2011.

ACKNOWLEDGEMENTS

Subject testing was performed at Johns Hopkins University. Dr. Gelsy Torres-Oviedo oversaw the project.

A METHOD FOR ASSESSING THE SEEDING EFFICIENCY OF HUMAN ADIPOSE-DERIVED STEM CELLS IN SYNTHETIC SCAFFOLDS

Alexander D. Josowitz[1], Jeffrey T. Krawiec[1,5], Brian J. Philips[3], Antonio D'Amore[5], William R. Wagner[5,6], J. Peter Rubin[3,5], David A. Vorp[1,2,4,5,6]
1. Department of Bioengineering 2. Department of Cardiothoracic Surgery 3. Department of Plastic Surgery
4. Department of Surgery 5. McGowan Institute for Regenerative Medicine
6. Center for Vascular Remodeling and Regeneration
University of Pittsburgh, PA, USA
Email: adj34@pitt.edu

INTRODUCTION

Cardiovascular disease is the leading cause of death within the United States and current revascularization techniques, such as autologous vein grafting, are limited by their lack of availability and low success rate due to intimal hyperplasia development [1,2]. Because of this, tissue engineers have long sought to develop a small-diameter vascular graft that adequately mimics the anatomy and functionality of a native artery.

To develop a tissue engineered blood vessel (TEBV), we have previously seeded mesenchymal stem cells within bilayered poly(ester urethane)urea (PEUU) scaffolds utilizing a rotational vacuum seeding device (RSVD) [3]. This provides a rapid (<5 min), efficient (>90%), and uniform distribution of cells within PEUU scaffolds [4]. Upon implantation of these TEBVs in a rat model, they remained patent over 8 weeks and developed a composition similar to native vessels [5]. However, the implanted cells were derived from rats and thus do not adequately mimic the use of human cells.

To continue the development of this stem cell based-TEBV with a clinical goal in mind, it is crucial to assess TEBV functionality when composed of human cells. The first step in this process is to seed human adipose-derived stem cells (ADSCs) from healthy, diabetic and older donors (the latter two both high-risk groups for cardiovascular disease) into PEUU scaffolds and analyze their cellular distribution.

Ensuring that a proper cell distribution (i.e. uniform in all directions) is achievable for each donor type is important not only for quality-control – and thus can eliminate variability concerns due to poor TEBV construction in future studies – but because a TEBVs function is heavily affected by its cellular composition. However, in order to perform this type of quality control would require manually counting thousands of cells, which is not practical. Thus, the goals of this project were to **develop an automated cell counting tool** to expedite the process of analyzing cell distributions within the scaffolds and to analyze scaffolds seeded with human ADSCs from healthy, diabetic, and older donors. This counting tool will be of benefit to anyone with the need to count cells, determine cell densities, and characterize cell distributions in seeded scaffolds.

METHODS

ADSCs were generously provided by Dr. Peter Rubin's laboratory and were classified into three groups (**Table 1**). This division isolates comparisons between young and old as well as non-diabetic and diabetic donors. The ADSCs obtained from each donor were cultured in ADSC growth media (DMEM+1:1 DMEM/F12 containing 10% FBS and antibiotics) with media replenished every 2 days. Upon confluence, ADSCs were seeded into tubular PEUU scaffolds donated by Dr. William Wagner's laboratory utilizing the RSVD. TEBVs were then dynamically cultured in spinner flasks for 48 hours to allow for cell attachment. TEBVs were fixed in

Group	Age (years)	Diabetic
Healthy	< 45	No
Diabetic	< 45	Yes
Old	> 65	No

Table 1. Classification of ADSC donors

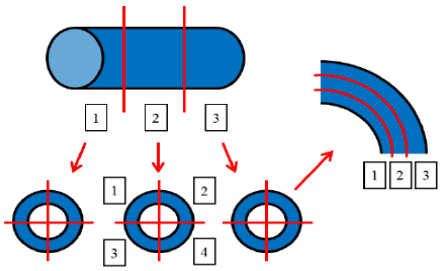

Figure 1. Division of TEBVs into longitudinal, circumferential, and radial segments for analysis of cell distribution

paraformaldehyde and embedded in OCT media for histological analysis. TEBVs were separated into 3 longitudinal pieces and each was cut to obtain a circular section via a cryo-microtome. Sections were then stained with DAPI to identify cell nuclei. Complete multi-colored images of each circular TEBV section were acquired at 10x using an epi-fluorescent microscope with NIS Elements software (4.0, Nikon Instruments, Melville, New York) and an image stitching toolbox within ImageJ (1.47, Rasband, Bethesda, Maryland). To analyze the cell density an automated tool was developed using ImageJ macros to filter the images, remove background noise, and count the total number of cells present. Complete images from the 3 longitudinal sections were then segmented into 4 circumferential quadrants and 3 radial sections to analyze uniformity in all directions (**Figure 1**). One-way ANOVA was used to determine if significant differences at $p<.05$ existed between the data for the sections within each donor type.

RESULTS

An image-processing tool was developed with ImageJ to filter TEBV images and automatically count cell nuclei. The tool separates the channels of multi-channel images to obtain the blue channel (DAPI) and applies a difference of Gaussian blurs to remove background noise. It then uses Otsu's threshold to convert the pixels to binary, creating contrast between the background and foreground. Then the tool uses a watershed command to separate large objects into individual cells. Finally, the tool counts the cell nuclei as particles (**Figure 2)**. Excluding longitudinal diabetic TEBVs, all TEBVs displayed uniform cell distribution in all directions (**Figure 3**, circumferential and longitudinal not pictured) as shown by non-significant ANOVA results (**Table 2)**.

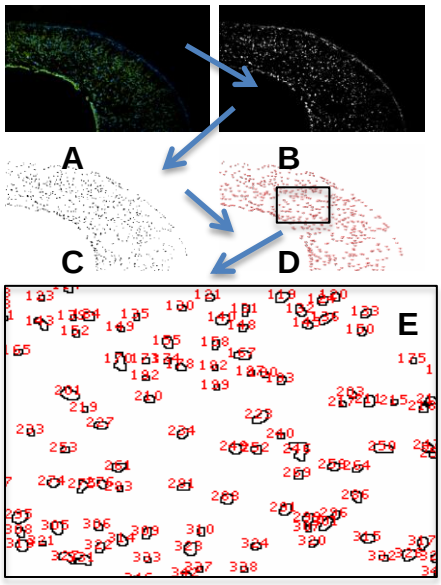

Figure 2.
A) Original multi-channel image
B) DAPI-channel is extracted and difference of Gaussian blurs applied
C) Otsu's Threshold and watershed are applied
D) Final image with cells counted marked in red
E) A close up of cells that have been counted and numbered

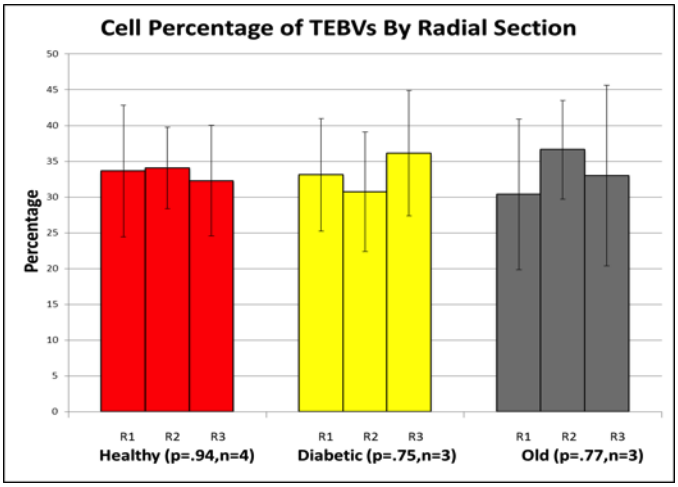

Figure 3. Comparison of radial cell density across 3 sections in TEBVs seeded with healthy, diabetic, and old cells.

Donor Type	Longitudinal	Circumferential	Radial
Healthy (n=4)	0.74	0.96	0.94
Diabetic (n=3)	0.05	0.48	0.75
Old (n=3)	0.26	0.65	0.77

Table 2. A table of p-values for differences between cell counts for different sections by donor type and direction

DISCUSSION

The lack of significant differences between the mean cell nuclei counts for the longitudinal, circumferential, and radial sections demonstrates an even seeding density across the TEBV for all donor types, removing a potentially problematic source of variability in future testing. It is likely that the discrepancy amongst the diabetic longitudinal data is a result of a manufacturing issue that altered the shape of the diabetic scaffolds. The automated cell counting tool can benefit those who need to count cells, determine cell densities, and characterize cell distributions in multi-channel images.

REFERENCES

1. Isenberg et al. *Circulation Research* **98**. 25-35. 2006.
2. Weintraub et al. *American Journal of Cardiology*. **73**. 103-112. 1994.
3. Nieponice et. al. *Biomaterials*. **29**. 825-8332. 2008.
4. Soletti et al. *Biomaterials*. **27(28)**. 4863-4870. 2006.
5. Nieponice et al. *Tissue Eng Part A*. **16(4)**. 1215–1223. 2010.

ACKNOWLEDGMENTS

I would like to acknowledge the Swanson School of Engineering for funding this research project and Dr. Vorp and Jeffrey Krawiec for mentoring me through this research experience.

A Multi-Channel Electrical Micro-Stimulation System for Sensory Feedback Research

Scott Thompson
Rehabilitation Neural Engineering Lab, Department of Bioengineering and Department of Physical Medicine and Rehabiliation
University of Pittsburgh, PA, USA
Email: swt5@pitt.edu, Web: http://w3.rnelab.com/

INTRODUCTION

Direct neural interfaces have demonstrated the capacity to provide paralyzed people with the ability to control dexterous prosthetics [1], however, subjects currently lack somatosensory feedback from these devices. This lack of proprioceptive and cutaneous feedback is thought to be a significant barrier to achieving device embodiment and naturalistic control. To overcome this, high-channel count electrical micro-stimulation of the nervous system has been proposed. Unfortunately, available multi-channel stimulators frequently lack the capabilities required by research labs to fully explore the immense parameter space associated with micro-stimulation. To overcome these limitations, I started the development of a multi-channel stimulator based on National Instruments (NI) hardware and a single-channel isolated stimulator that would enable direct stimulation of the nervous system through microelectrode arrays.

The aims of this project were to develop a stimulation system that allowed two simultaneous channels of stimulation to be delivered through up to 64 connected electrodes. The pulse parameters of the stimulus waveforms were required to be programmable and pulses should be delivered as current-controlled waveforms. Finally, the interface to the stimulator should be accessible through an API-like method.

METHODS

Figure 1, shows the overall flow diagram for the proposed system and illustrates the communication, connection and control pathways between devices. The NI hardware includes a PXI chassis, which contains a high-speed multi-function data acquisition (DAQ) board (PXI 6259) and a high-density FET switch matrix (PXI 2535). The NI hardware is controlled by the computer via LABVIEW and interconnects with a custom PCB that performs as the connection hub for all devices. The PCB also communicates with two analog stimulus isolators (A-M Systems, Model 2200) and electrodes for stimulation.

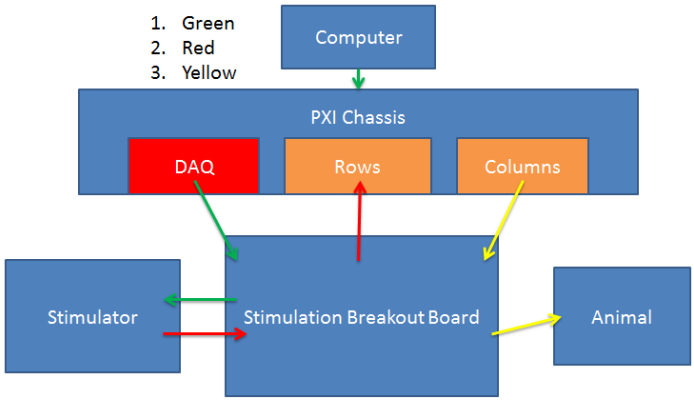

Figure 1: Flow Chart for Stimulation

In order to generate a pulse at the target electrode, the NI (DAQ) board first generates a voltage signal with the parameters of a stimulation waveform sampled at a frequency of 100 kHz. This waveform is sent directly through the PCB to the isolated stimulator acting as a voltage-to-current converter. The current waveform is then routed through the PCB to an NI switch matrix. The switch matrix enables the multi-channel capabilities of the device by selecting one of up to 64 output channels using an array of MOSFET switches. The resulting current waveform is then routed back through the PCB to the desired electrode channel for stimulation.

The switch matrix (4 rows, 136 columns) contains a switch at each intersection of a row and column in a matrix. The active rows include the stimulator positive and negative terminals while the active columns include all 64 electrodes, as well as the return electrode, an external ground, and the stimulator positive terminal. In order to make a connection to an electrode, there is a specific

sequence that the switches are opened and closed to provide a safe connection to the preparation and ground for stimulation while also having a complete disconnection when there is no stimulation pulse. During periods where no stimulation is being delivered, the stimulator positive and negative terminals are connected together so that current cannot flow to the electrodes (the terminals are shorted at the stimulator). When a stimulus pulse is commanded to be generated, the shorted terminals are disconnected, the return electrode is connected to the negative terminal of the stimulator, and the stimulator positive terminal is connected to the electrode channel specified by the user. After the stimulation pulse is completed, the positive terminal of the stimulator disconnects from the electrode channel, the return is disconnected and the terminals of the stimulator again get shorted. The switches have a switching time of approximately 12 µs, enabling fast connection and disconnection to the electrodes.

The Labview VI designed to coordinate and control the stimulator has three inputs: an *N*x8 matrix with each row containing the pulse parameters and timing for a single pulse, trigger type (software or external hardware), and the type of grounding. There are two loops that run simultaneously where one is a state-machine primarily controlling the switches, pulse parameters, and analog waveform while the other loop deals with timing. Timing is controlled through the use of counters in the DAQ board. When the edge counter reaches the specified timing parameter value, a trigger is sent to the other loop to start switching and send out the waveform. Simultaneously, the counters reset and start counting until they reach the timing parameter of the subsequent pulse. The loops will continuously run until there are no more pulses to generate.

RESULTS

The NI system was designed for this specific implementation and the system was tested using a test program where pulses were generated and switching was controlled. This test program ensured that the switching was properly executed, the DAQ generated a waveform with the parameters specified and the control of the system, via computer, occurred as expected.

The PCB was designed using DipTrace (schematic capture and PCB design software) and the connectors implemented on the board were specifically chosen to match the cables already in use by the lab. The PCB and connectors were ordered, hand soldered and tested.

After the testing of the NI system and the integration of components on the PCB, a general purpose API was developed to control the devices and implement the procedure described in the methods section.

DISCUSSION

The stimulator will provide the lab with a less expensive, highly customizable option for stimulation. The stimulator, due to the switching procedure described earlier, will be safer than many other stimulators available on the market due to the well-controlled connection/disconnection scheme that ensures that the stimulator is only connected to an electrode when a pulse is generated. This stimulator will also allow bipolar stimulation (between any two electrodes) due to the flexible configuration scheme, as well as dual-channel stimulation. These features will allow advanced investigations into the method of neuronal recruitment in nervous tissue that may ultimately enable closed-loop sensory neuroprostheses to become a reality.

REFERENCES

1. Collinger, J. L., Wodlinger, B., Downey, J. E., Wang, W., Tyler-Kabara, E. C., Weber, D. J., McMorland, A. JC., Velliste, M., Boninger, M. L., Schwartz, A. B. (2012). High-performance neuroprosthetic control by an individual with tetraplegia. *Lancet*. 10.1016/S0140-6736(12)61816-9

ACKNOWLEDGEMENTS

The engineers and other workers at the Rehabilitation Neural Engineering Lab provided an excellent learning environment with a positive attitude and patience towards a student with very little background in this specific subject of research.

DYNAMIC ABILITY OF FIBER-FILLED GELS TO CONTROL OIL-DROPLET MOTION IN WATER SYSTEMS

Gerald T. McFarlin, Xin Yong, and Anna C. Balazs
Mascaro Center for Sustainable Innovation, Department of Chemical Engineering
University of Pittsburgh, PA, USA
Email: gtm9@pitt.edu

Introduction

There is a pressing need for robust oil-water separating systems for environmental and economical purposes. High recovery of oil in the petroleum industry requires effective separation techniques [1]. A few techniques capable of separating micro-scale oil droplets exist, yet it is still challenging to do so practically on a large-scale [2-4]. Thus, it is desirable to design novel materials that can effectively separate the two liquids.

Thermo-responsive micro-/nanogels quickly respond to temperature changes by shrinking or swelling due to their small size. Thus, they can be used to develop materials that can dynamically change their size, morphology, or functionality in response to external stimuli. Using a polymeric gel and fibers, we design a thermo-responsive composite film that can be harnessed to control the motion of oil droplets in microfluidic devices. We use dissipative particle dynamics (DPD) to model our system [5]. By varying the system temperature, we can program the film to dynamically catch and release oil. Our findings reveal how nanofibers can be integrated into the gel system to achieve synergistic manipulation of droplet motion, and how this thermo-responsive nanocomposite gel coating could be utilized as a phase-separation tool.

Methods

The system that we built is composed of gel, fiber, oil, water, and wall DPD beads. Conservative (soft repulsion) interaction parameters between beads of different species were carefully chosen to simulate the desirable behaviors between the system components. The parameters were chosen such that the oil was slightly more hydrophobic than the oily fibers, and so that the gel, wall, and water behaved as hydrophilic moieties. The gel swelling dynamics were reproduced consistently with experiments and other simulations [6-8]. Table A-1 in the Appendix shows the exact parameter coefficients chosen. The values change proportionately to the temperature change, and were adjusted accordingly [5].

A rigid sphere was generated to simulate a micro-scale hydrophobic particle in water. To drive the droplet parallel to the film, a laminar shear flow was generated by moving the top wall of the simulation box each time step.

To compare the fiber-gel to its isolated component systems, we prepared three systems which are described in Table 1.

Table 1. Trial Descriptions.

Trial 1	Oil drop interacts with film; system T = 28℃
Trial 2	Oil drop interacts with film; system T = 48℃
Trial 3	System resulting from Trial 2 is cooled to 28℃

Results

Figs. A-1, A-2, and A-3 in the Appendix show the motion of the particle when exposed to the fiber-filled gel in the three trials. Table 2 displays the distance traveled by the particle in the direction of the fluid flow.

Table 2. Distance traveled by oil-particle during trials.

	Fiber-Filled Gel*	Fiber System**	Gel System**
Trial 1	408.9946	19.7738	192.2411
Trial 2	20.6024	18.7096	140.1175
Trial 3	136.2321	-3.9280	206.5900

*1,000,000 time step trials
**500,000 time step trials, due to computational time limits

Discussion

According to the results from the fiber-filled gel trials, the droplet traveled a significantly longer distance during trials 1 and 3 than in trial 2. In trial 1, the gel screened the fibers from interacting with the droplet (the interaction between fibers and droplet is energetically favorable). In trial 2, the heated gel revealed its embedded fibers to allow the favorable fiber-droplet interaction to ensue. Analyzing Figs. A-1 and A-2, the droplet traveled approximately 20 DPD units in the first 100,000 time steps before contacting with the film. During this time period, the droplet was moving towards the film. When the droplet interacted with the exposed fibers, it was pulled close to the film, and even slightly back against the fluid-flow (corresponding to the small overshooting in Fig. A-2). The droplet then remained trapped in the gel by the fibers. In trial 3, the gel swelled and pushed the droplet away from the fibers. When fully swollen, the gel once again completely hid the fibers from interacting with the droplet and allowed the droplet to move away from the film.

Comparing the results from the fiber-filled gel to the bare-component trial results, we find that the combination of fibers with the gel is critical in realizing the film's complex dynamic

behavior. In all of the fiber-only trials, the droplet was pulled towards the substrate surface and pinned there for the remainder of the trial. Since the fibers do not respond to temperature changes, they were incapable of releasing the droplet. The bare gel system behaved oppositely. The shrunken thermo-responsive gel still repelled the droplet when heated to 48℃. Consequently, the gel did not significantly prevent the motion of the droplet. Variations in distance traveled by the droplet in trials 1-3 for the bare gel system can be attributed to the different friction caused by the gel at different temperatures (due to different polymer volume fraction) rather than the attractive interactions that hindered the droplet motion in the systems containing fibers.

Conclusions

The results provide evidence that the designed film could be used to separate oil droplets from predominantly water systems. The parameters used provide guidelines for extending this system from computational to a experimental setting.

This study will continue in order to find ranges within which the system is capable of catching and releasing oil-droplets. Elasticity of fibers is also a parameter that needs to be explored in depth—heating a film with very flexible fibers may result in some fibers bending and remaining hidden in the gel. This would influence the fiber density of the system and the ability of the film to catch oil-droplets. On the contrast, very stiff fibers may be less effective at catching droplets due to their inability to wrap around the oil. These questions will be explored in order to gain a deeper understanding of this thermo-responsive system that has potential for efficiently separating oil-contaminated water.

References

1. Banat, I. M. Biosurfactants production and possible uses in microbial enhanced oil recovery and oil pollution remediation: a review. Bioresour. Technol. 51, 1–12 (1995).
2. Kota, A. K. et al. Hydro-responsive membranes for effective oil-water separation. Nat. Commun. 3, 1025 (2012).
3. Kwon, G. et al. On-demand separation of oil-water mixtures. Adv. Mater. 24, 3666–3671 (2012).
4. Field, R. W. Separation by reconfiguration. Nature 489, 41–42 (2012).
5. Groot R. D. and Warren P. B. Dissipative particle dynamics: Bridging the gap between atomistic and mesoscopic simulation. J. Chem. Phys. 107, 11 (1997).
6. Quesada-Peréz M. et al. Computer simulations of thermo-sensitive microgels: Quantitative comparison with experimental swelling data. J. Chem. Phys. 136, 244903 (2012).
7. Hirotsu, S. Softening of bulk modulus and negative Poisson ratio near the volume phase-transition of polymer gels. J. Chem. Phys. 94, 3949-3957 (1991) .
8. Hellweg, T. et al. Colloidal crystals made of poly(N-isopropylacrylamide) microgel particles. Colloid Polym. Sci. 278, 972-978 (2000).

Appendix

Table A-1. Conservative Interaction Parameters a_{ij} in equation $F^{C}_{ij} = a_{ij}(1-r_{ij})\hat{r}_{ij}$

Species j \ Species i	Gel	Fiber	Oil	Water	Wall
Gel	25	37	40	Chi*	25
Fiber	X	25	28	37	37
Oil	X	X	15	40	40
Water	X	X	X	25	25
Wall	X	X	X	X	25

*Chi is a function of the system temperature and gel polymer volume fraction. This parameter is responsible for the gel-swelling/-shrinking kinetics [5]

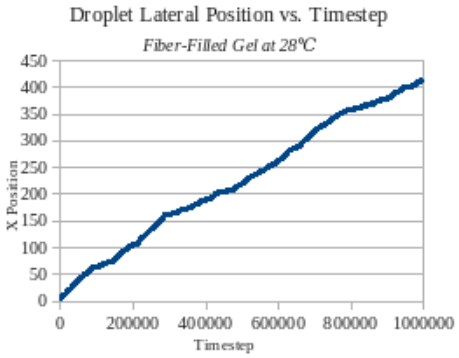

Figure A-1: Droplet motion in direction of water flow while interacting with fiber-filled gel in Trial 1

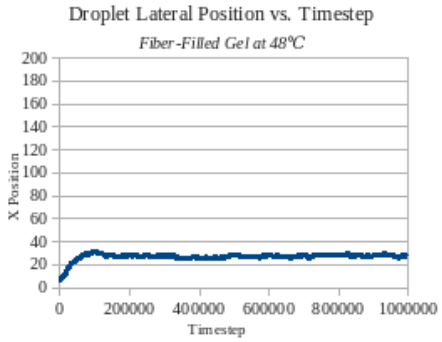

Figure A-2: Droplet motion in direction of water flow while interacting with fiber-filled gel in Trial 2

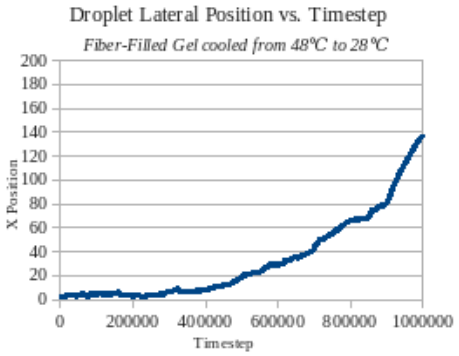

Figure A-3: Droplet motion in direction of water flow while interacting with fiber-filled gel in Trial 3

Investigation of Human Embryonic Stem Cell Differentiation Induced by Chitosan Nanoparticles

Kimaya Padgaonkar[1], Thomas Richardson[1], Joseph Candiello[2],
Shilpa Sant[2,3,4], Ipsita Banerjee[1,2,4]
Department of Chemical Engineering[1] & Department of Biongineering[2], Swanson School of Engineering; Department of Pharmaceutical Sciences[3]; McGowan Institute for Regenerative Medicine[4]
University of Pittsburgh
Email: kip15@pitt.edu

INTRODUCTION

Type 1 diabetes results in the destruction of insulin producing cells, leaving the individual insulin dependent. These people require alternative sources of insulin, such as manual insulin injection or transplantation of donor organs. However, insulin injections are inconvenient while donor organs and islets for transplantation are scarce, therefore, an alternative option—the transplantation of insulin producing cells from a regenerative source—could be highly influential. With their unlimited self-renewal capacity, hESCs can potentially alleviate the problem of current insulin sources, after undergoing successful differentiation to the proper functional cell type. Directed differentiation by addition of chemical factors is one method that allows for induction of hESC to the mature functional cell types. However, these soluble growth factors, such as Activin A typically used to induce definitive endoderm, are expensive. We investigated the possibility of using less expensive, insoluble materials such as chitosan to induce differentiation. We investigated the possibility of differentiating hESCs in presence of chitosan using alternate culture configurations.

METHODS

2-D cultures in tissue culture plastic (TCP), a common method for culturing cells, was utilized as were two different 3-D methods---calcium alginate encapsulation and cellular aggregation. The 2D cultures, with CNPs added in the culture media, elicited no significant effect in the hESC population. In the 3D configuration first we co-encapsulated hESCs with chitosan nanoparticles (CNP) in calcium alginate. The co-encapsulated cells were allowed to differentiate with and without the growth factor, Activin A. hESCs encapsulated in calcium alginate without CNPs were used as control for spontaneous differentiation. Very interestingly, the CNP co-encapsulated hESCs showed significant enhancement in differentiation, compared to the spontaneous control. In 3-D encapsulation, gene expression analysis showed that ectoderm and mesoderm specific differentiation were not induced. Quite surprisingly however, mesendoderm and endoderm specific differentiation were induced on a level similar to chemically induced differentiation by Activin A. Definitive Endoderm differentiation was confirmed by analysis of protein expression for proteins indicative of the DE layer. Since chitosan was observed to induce endoderm differentiation even without any growth factor, we began an investigation of the effect of chitosan on hESC aggregates alone.

To isolate the cause of differentiation, calcium alginate were eliminated in our subsequent experiments, and hESCs were directly aggregated with CNP using alternate formation methods. Confluent H1 hESC colonies were made into a single cell suspension with Accutase and treated with ROCK inhibitor. Two

methods were utilized to form aggregates. The hanging drop method had a cell seeding density of $10x10^5$ cells/mL and 30 µL of media for each hanging drop. Aggregates were collected after 4 days. CNP to hESCs mixed ratios were 1:1, 1;10, and 1:40. The microwell method had a cell seeding density of $10x10^6$ cells/mL in 450 nm microwells, and were seeded using two sequential seedign steps. Aggregates were collected after 4 days. Three techniques were used: CNPs mixed with hESCs (1:10) and then seeded in two steps; CNPs seeded between two layers of hESCs (1:40); CNPs mixed with hESCs (1:40) and then seeded in two steps.

RESULTS

For the hanging drop method, 1:40 CNPs to cell ratio had the best EB formation and CNP incorporation of the three concentration ratios tested. Figure 1 below displays the formed aggregates for the hanging drop method.

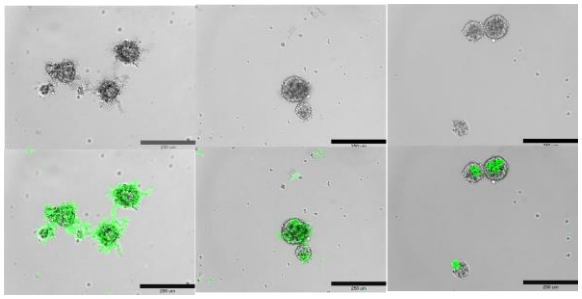

Figure 1: From left to right, CNP to hESCs mixed ratios are 1:1, 1;10, and 1:40.

For the microwell method, 1:40 CNPs to cells ratio had the best EB formation and CNP incorporation of the two concentration ratios tested. The mixed approach was more straightforward than the layered approach. Figure 2 below displays the formed aggregates for the microwell method.

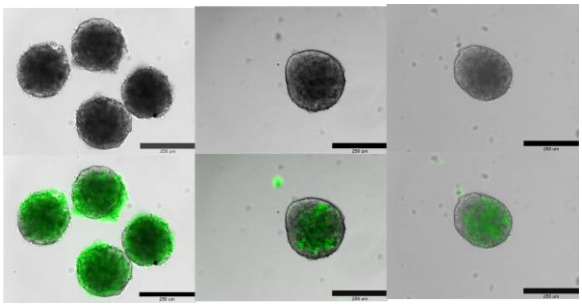

Figure 2: From left to right, CNPs mixed with hESCs (1:10); CNPs seeded between two layers of hESCs (1:40); CNPs mixed with hESCs (1:40).

DISCUSSION

The best technique creating aggregates in microwells had the greater ratio between CNPs and cells (1:40) and incorporated CNPs with cells prior to seeding. It created uniform aggregates and was more straightforward compared to the layering method. The microwell method showed better incorporation of CNPs within aggregates compared to the hanging drop method which created smaller, less uniform aggregates even within the same CNP ratio trials. Aggregates formed by the microwell method were further analyzed via gene expression and the results were not as expected as compared to the encapsulation gene expression data. We observed little to no upregulation in the definitive endoderm stage even though the encapsulation data had showed strong upregulation. The microwell method is still under investigation so trials will be repeated and further analyzed. Based on those results, exploration of microwell (sizes) and CNP incorporation (ratios) can be continued.

ACKNOWLEDGEMENTS

Thank you Dr. Shuman, Swanson School of Engineering, Dr. Parker, Systems Medicine REU: NSF/EEC #1156899 & Dr. Russell Clark, PASGC for partial support

Using MSC-Conditioned Media to Reconstruct Gluococorticoid Damaged Trabecular Meshwork Cytoskeleton

Anthony Cugini, Morgan Fedorchak, and Steve Little
Little Lab, Department of Chemical Engineering
University of Pittsburgh, PA, USA
Email: avc10@pitt.edu, Web: http://www.littlelab.pitt.edu/

1. Introduction

Synthetic glucocorticoid (GC) drugs are used to suppress the immune response in cases such as allergies[1]. However, one of the potentially harmful side effects of GC use is ocular hypertension that can lead to an increased chance of developing iatrogenic secondary open-angle glaucoma[2].

GCs cause ocular hypertension by increasing resistance to aqueous humor flow through the eye[3]. Severity of the response to GCs is dependent on duration and potency of the dose as well as individual susceptibility of the patient[4].

The mechanisms of GC-induced hypertension involve altering two cell processes in the ocular drainage canal: formation of cross-linked actin networks (CLANS) in trabecular meshwork (TM) cells and decreased phagocytosis in TM cells[5]. Normally, TM cells form a sheet over the aqueous humor drainage canal, filter out extracellular debris and pump humor out of the eye and back into circulation[6]. When the TM cells are treated with GCs, there is a buildup of cytoskeletal materials and decreased pores through the sheet of TM cells, drastically slowing down ocular drainage pathways[7]. These side effects are similar to the symptoms of primary open angle glaucoma, the most prevalent form of glaucoma[7]. Such effects can be reproduced in laboratory models with dexamethasone (a widely used GC) to simulate the symptoms of primary open angle glaucoma (POAG) In Vitro[8].

Current treatments for POAG aim at reducing IOP by decreasing production or flow of IOP[9]. However, novel treatments are continually sought after.

Mesenchymal Stem cells (MSCs) are a promising new area of tissue regeneration and of particular interest in glaucoma therapies[10]. The effects of these cells are only beginning to be understood, but already, these cells are being used to regenerate damaged tissue in the presence of active diseases such as osteoarthritis[10]. Studies propose MSCs are releasing factors that influence the damaged cells around them to begin repair[10]. These released factors can be collected and filtered to produce a conditioned media. We want to use the conditioned media from the MSCs to treat TM cells damaged in an iatrogenic glaucoma model and monitor for cytoskeleton repair.

2. Methods

2.1 TM Cell Culture

Human Mesenchymal Stem Cells were cultured in biologic conditions (37°C) in 75cm^2 adherent cell culture flask with TM cell medium consisting of Gibco Minimum Essential Medium supplemented with 10% fetal bovine serum and 1% penicillin/streptomycin.

2.2 In Vitro Model Treatment

TM cells were plated onto a 12 well adherent plate at $4*10^5$ cells per well. Cells were grown for 7 days to achieve a monolayer. Cells were then treated every day for 4 days

with groups: no DEX, 100nM DEX, 300nM DEX. On the fourth day, one hour after the treatment, cells were blocked with Formalin and prepared for staining.

2.3 Staining and Microscopy

Cells were stained with FITC, TRITC, and DAPI in order to visualize focal adhesions, cytoskeleton, and nuclei respectively. Imaging was done on a Nikon Eclipse TI fluorescent microscope using Nis Elements Br to analyze the images.

2.4 CLAN Quantification

CLAN percentages were calculated according to the protocol set up by Filla et al which stated that any 3 actin filaments connected by 3 vertices constitute a CLAN[11](figure 1).

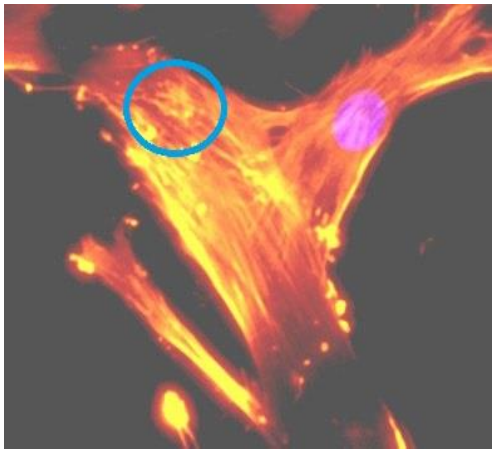

Figure 1: A TM Cell with CLAN circled in blue (image taken on 7/3/13)

Results

3.1 TM Cell Treatments

The 300nM DEX group achieved a CLAN percentage of 47.1%. The 100nM group had 18.1%. The control group had 5.7% CLANs. These results are supported by literature values[11,12].

Acknowledgements

Thanks to the Little Lab and my mentors Morgan Fedorchak and Steven Little for all the help this summer. Also thanks to the Swanson School of Engineering for my scholarship.

References

1. Stamer, Daniel W. Et Al. Unique Response Profile of Trabecular Meshwork Cells to the Novel Selective Glucocorticoid Receptor Agonist, GW870086X *IOVS* 2013;54:2100-2107.
2. Clark AF, Wordinger RJ. The Role of Steroids in Outflow Resistance. *Exp Eye Res*. 2009;88:752–759.
3. Becker B, Mills DW. Corticosteroids and Intraocular Pressure. *Arch Ophthalmol*. 1963;70:500–507.
4. Clark A. Steroids, Ocular Hypertension and Glaucoma. *J Glaucoma*. 1995;4:354–369.
5. Ishihashi, Takeshi. Et Al. cDNA Microarray Analysis of Gene Expression Changes Induced by Dexamethasone in Cultured Human Trabecular Meshwork Cells. *IOVS.* 2002;43:3691-3697.
6. Johnstone, Murray A. M.D. The Aqueous Outflow System as a Mechanical Pump. *J. Glaucoma.* 2004;13:421-438.
7. Johnson D, Gottanka J, Fl¨ugel C, Hoffmann F, Futa R, Lutjen- Drecoll E. Ultrastructural changes in the trabecular meshwork of human eyes treated with corticosteroids. *Arch Ophthalmol*. 1997;115:375–383.
8. Wilson K, McCartney MD, Miggans ST, Clark AF. Dexamethasone induced ultrastructural changes in cultured human trabecular meshwork cells. *Curr Eye Res*. 1993;12:783–793.
9. Owen, Christopher G. Et Al. Hypotensive Medication, Statins, and the Risk of Glaucoma. *IOVS.* 2010; 51:3524-3530.
10. Manuguerra-Gagne, Renaud. Transplantation of Mesenchymal Stem Cells Promotes Tissue Regeneration in a Glaucoma Model Through Laser-Induced Paracrine Factor Secretion and Progenitor Cell Recruitment. *Stem Cells.* 2013; 31:1136-1148.
11. Filla, Mark S. Regulation of Cross-linked Actin Network (CLAN) Formation in Human Trabecular Meshwork (HTM) Cells by Convergence of Distinct β1 and β2 Integrin Pathways. *IOVS.* 2009; 50:5723-5731.
12. O'Reilly, Steven. Inducers of Cross-Linked Actin Networks in Trabecular Meshwork Cells. *IOVS.* 2011;52:7316-7324.

NANOSCALE HETEROGENIZATION OF HOMOGENEOUS ACETYLATION CATALYSTS USING NICKEL LINED SILICA NANOPARTICLES

Martin D. Roberts[1], Xinyu Liu[2], Götz Veser[1]
[1]Department of Chemical & Petroleum Engineering, University of Pittsburgh, Pittsburgh PA
[2]Department of Chemistry, University of Pittsburgh, Pittsburgh PA

INTRODUCTION

Homogeneous catalysts play an important role in many industrial reactions. However, the recycling these catalysts is energy intensive and time consuming. In the present work, two novel approaches to heterogenizing a homogeneous acetylation catalyst, 1,4-diazabicyclo[2.2.2]octane (DABCO), have been developed using well-characterized hollow core shell nickel-silica nanoparticles as the heterogeneous support.

The first approach is to encapsulate the catalyst. DABCO can be encapsulated by the hollow nickel-silica nanoparticles, denoted Ni@SiO_2, through diffusive physical loading by a concentration gradient. In this process, the amine catalyst is dissolved in a compatible, low molecular weight solvent, and the Ni@SiO_2 nanoparticles are placed in the solvent. The low molecular weight solvent easily diffuses through the 10 nm thick porous silica wall of the particle, entering the hollow cavity. The high concentration of the amine outside the pores creates a driving force for the amine to enter the pores into the amine-poor solvent in the cavity.

A second option for heterogenization of the tertiary amine catalyst is embedding it in the silica structure. Previous work has been completed on entrapment of organic molecules in a sol-gel matrix which shows that entrapped molecules can still participate in chemical reactions and are thermally and chemically stable.[1,2] Addition of DABCO into the synthesis of Ni@SiO_2 should result in co-condensation of the tertiary amine with the hydrolyzed SiO_2 from TEOS. The co-condensed amine will be embedded in the silica matrix.

METHODS

The model reaction used to study the catalytic activity of this research is the acetylation of hydroxyl groups. The present work focuses on the acetylation of 4-methoxybenzyl alcohol (anisyl alcohol) with acetic anhydride to form 4-methoxybenzyl acetate (anisyl acetate) catalyzed by tertiary amines.[3] The UV-active aromatic structure within the alcohol and the acetate allow for the reaction to be monitored using thin layer chromatography under UV light.

The Ni@SiO_2 particles were prepared using a sol-gel synthesis. A reverse micro-emulsion was prepared by adding an ionic nickel aqueous solution to a cyclohexane/surfactant oil phase. Following the addition of the aqueous solution, hydrazine hydrate, ammonium hydroxide, and tetraethylorthosilicate (TEOS) were added. The hollow core of Ni@SiO_2 was stabilized with the addition of hydrazine hydrate, a strong reducing agent. The ammonium hydroxide established a basic environment for the reduction of nickel and catalyzed the hydrolysis reaction of TEOS. DABCO was co-condensed with TEOS during synthesis to embed the amine within the Ni@SiO_2 structure. DABCO was loaded into the hollow core of Ni@SiO_2 through the constant evaporation of a catalyst rich solvent. There are advantages and disadvantages to each of these heterogenization approaches.

RESULTS

Encapsulation of DABCO within the hollow cores of Ni@SiO_2 slightly decreases catalytic activity, but the catalyst remains relatively active. This specific catalyst has minimal recyclability, as shown in Figure 1. Embedding of the homogeneous catalyst significantly decreases the catalytic

activity, but the recyclability is roughly 100% (within experimental error). The recyclability of the synthetically embedded catalyst is shown in Figure 2.

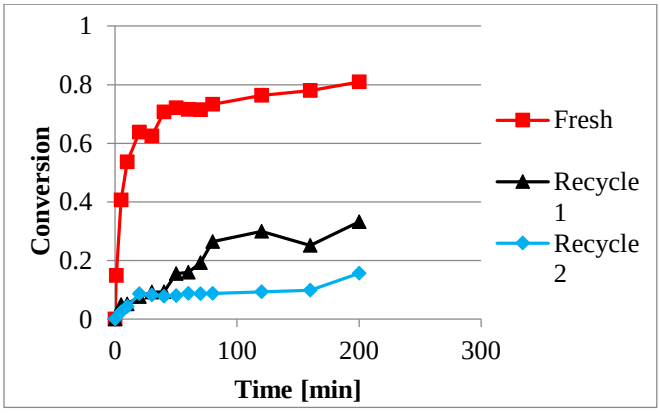

Figure 1: Core Encapsulation Recyclability

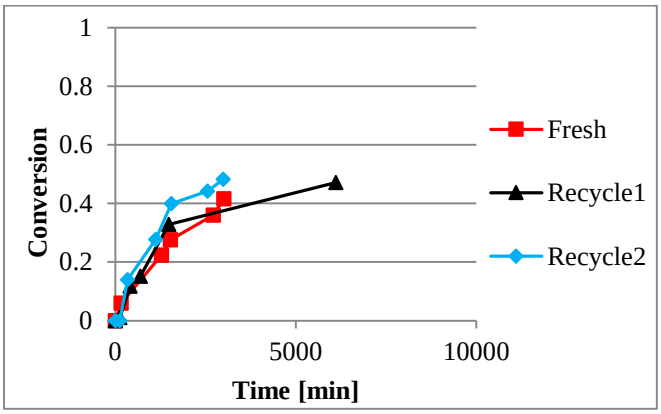

Figure 2: Synthetic Catalyst Embedding Recyclability

DISCUSSION

This study has shown that heterogenization of tertiary amine catalysts on the nanoscale can be used for the sustainability goal of recyclable acetylation catalysts. The encapsulated DABCO particles are slightly recyclable, while the embedded DABCO particles are roughly 100% recyclable. However, there is a cost in activity and reaction rate, particularly with the embedded particles which take days to reach 50% conversion. Further research will aim to increase the efficiency of the embedded nanoparticles. Also, nanoencapsulation of DABCO could be performed on the embedded Ni@SiO_2-DABCO structures, creating a hybrid catalyst with high recyclability and high activity. Another avenue for research is the embedding of 4-dimethylamino pyridine (DMAP), the typical industry choice for acetylation catalyst. Trial runs have shown that homogeneous DMAP has roughly 20 times the reaction rate that DABCO gives for the 4-methoxybenzyl alcohol acetylation reaction.

ACKNOWLEDGEMENTS

This project is funded by the Swanson School of Engineering and the Roberta Luxbacher Scholar Fund through the Mascaro Center for Sustainable Innovation at the University of Pittsburgh. This work was completed under Dr. Götz Veser, principal investigator of the catalytic reaction engineering group at the University of Pittsburgh.

REFERENCES

1. Avnir, David. "Organic chemistry within ceramic matrixes: doped sol-gel materials." Accounts of chemical research 28.8 (1995): 328-334.
2. Matsui, Kazunori. “Chapter 20: Entrapment of Organic Molecules.” Handbook of sol-gel science and technology. 1. Sol-gel processing. Ed. Sakka, Sumio. Vol. 1. Springer, 2005.
3. Greene, Theodora W., and Peter GM Wuts. Protective groups in organic synthesis. Vol. 168. New York: Wiley, 1999.

MIGRATION RATES AND METRICS OF THE PERUVIAN AMAZON

Adrian Mikhail P. Garcia
Civil and Environmental Engineering Department
University of Pittsburgh, PA

INTRODUCTION

Starting in Peru, the Amazon River flows through Columbia and Brazil; additionally, tributaries from Bolivia, Venezuela, and Ecuador contribute to the massive river and its unique geomorphic features. Accordingly, the Amazon has become an important aspect of South America and those living there.

The Amazon River Basin covers an area of 6.7 million km^2, approximately twice the size of India. It houses one of the most important ecosystems in the world, with an incredible terrestrial mammal richness, tree biodiversity, and aquatic ecosystem [1]. In addition, millions of people live along or near the Amazon River; hundreds of indigenous tribes still reside within the Amazon River Basin, while the cities Iquitos, Leticia, Manaus, and Belem are all settled along the river. These people depend upon the Amazon River and its many resources. Another important feature of the Amazon River is the transportation along it; as various commercial products, including oil, rubbers, and wood, make their way downstream, the economics of the many port cities along the river continue to thrive.

Due to the sheer magnitude and exceptionality of the Amazon River, research regarding the morphodynamic processes that shape and define the river has been difficult. It is ineffective simply to "scale up" datasets from smaller rivers and flume experiments because they do not take into consideration the anabranching structures that are found in the Amazon River and other "mega" rivers [2].

The purpose of this research was to gain an understanding of the Amazon's geomorphology. In order to accomplish this, migration rates of the Amazon River's channel within its floodplain were examined. Furthermore, numerous geomorphic metrics were extracted from planform images in order to explore possible correlations between different parameters.

PLANFORM ANALYSIS

Landsat images from the United States Geological Survey Global Visualization tool were analyzed in order to gather the data for this study. For a period from 1985-2012, satellite images were download for the entire Amazon River in increments of 5 years, excluding from 2010-2012.

This analysis was done on ArcGIS; because the images had geographic spatial referencing, they easily created a satellite image mosaic of the Amazon River when all imported onto the ArcMap data frame. For the purposes of this research, the UTM85-21S coordinate system, a meter-based coordinate system, was used. In addition to ArcGIS' standard tools, a Planform Statistics Tools and ET GeoWizards toolbox were used to gather the planform metrics.

Metrics

Various metrics were gathered for the purpose of this research: channel count, channel width, sinuosity, main channel centerline migration vectors, island count, island area, island perimeter, and confluence and bifurcation angles. While channel count, island count, and main channel centerline migration vectors were acquired for the entire Amazon River, the other values were only obtained for the Peruvian Amazon due to time constraints.

Average channel width for a channel was acquired by first creating a centerline for that channel with the Planform Statistics toolbox's capability to interpolate centerlines from 2 polyline banks. Then, the channel centerline's length was calculated using ArcMap's standard utilities. Afterwards, area was found by binding the 2 polyline bank and using the ET GeoWizards toolbox to convert the closed polyline into a polygon, from which area could be calculated. Sinuosity is a measure of how much a river channel bends and is found by dividing its length by the distance between its starting and ending point.

The main channel was digitized for all the years that the satellite images were acquired. After the banks were drawn, the centerlines were interpolated; these centerlines were then compared to adjacent years and migration vectors were created using the Planform Statistics toolbox. These vectors were processed and compared to different metrics in an attempt to draw conclusions from correlations.

Hickin Plot

According to Edward J. Hickin [5], who studied meandering rivers, there is a relationship between the migration rates of channel bends and the ratio of their channel bend radii over channel width. This ratio categorized each bend into its stage of development as: initiation, growth, or termination. When plotted against the migration rate, this ratio produced a certain trend-line for meandering rivers; the question arises, of course, if this same analysis applies to the Amazon River.

Channel radius was found from circles drawn to the size and shape of each bend of the main channel from the confluence of the Ucayali and Maranon up until Leticia, at the Peru-Colombia-Brazil border. Hickin's original plot of r_m / w_a against the migration rate yielded a certain shape. However, when the Peruvian Amazon was analyzed by these same values from 2005-2010, 2 trends were observed. One

of these appeared similar to the shape that Hickin achieved (showed by the line in graph below); the other was a cluster below it.

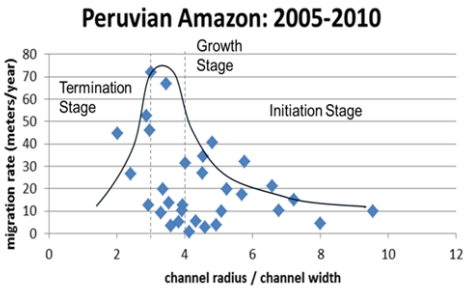

Main Channel Migration and Channel Count

For the Peruvian reaches of the Amazon, the migration of the main channel at each anabranching structure was compared to its number of channels. This analysis was done for the migration between 2010-2012, 2005-2010, and 1985-2005; this was to examine trends at a short term, medium term, and long term timespan.

The earlier year's channel count was used for this analysis; if the later year's channel count for a certain anabranching structure differed by more than 2, then that anabranching structure was not plotted. Surprisingly, for each plot, two trend-lines seemed to appear: one with a steeper upward slope for channel counts usually less than 4, and one with a less steep but still upward slope for channel counts usually greater than 4.

CONCLUSION

The Amazon River features a unique geomorphology. Spanning across the continent, the Amazon River is important for its rich ecosystem, plentiful resources, and valuable transportation routes. However, while much research has been conducted regarding the biodiversity of the Amazon River Basin, research on the Amazon River's morphodynamics are far from complete.

With the purpose of gaining an understanding the Amazon's geomorphology, research was conducted to analyze planform metrics through the use of Landsat satellite images and ArcGIS.

When Hickin's analysis was performed for the Peruvian reaches of the Amazon for its migration period from 2005-2010, 2 trends appeared: one which seemed to follow that of Hickin's original plot, and one that was a cluster of points below it. Upon further examination of these bends, it was found that the presence of anabranching structures did not seem to have any correlation with the trend to which each point was related. Consideration must be given to the vast geologic differences in the areas through which the Amazon River flows, the water levels throughout the river, and the different types of sediment prevalent in the channel bends of the Peruvian Amazon.

Most interesting was the relationship between the Peruvian Amazon's anabranching structures' island counts and their main channels' migration rates. Overall, an increase in channels results in faster migration rates, possibly because the presence of other channels forces the main channel to adjust its path; however, there appears to be some sort of a threshold at about 4 channels. Before this threshold, the migration rate increases much more rapidly with channel count than it does after; thus, this may reveal that an anabranching structure reaches relative stability upon developing about 4 channels.

Future Research

It is clear that further research is required in order to gain a more complete understanding of the morphodynamic processes that affect the Amazon River. Due to time constraints, many of the metrics were confined to the Peruvian reaches of the Amazon; metrics for the entire Amazon River should be collected for future research projects. Once all of this data is available, the first morphodynamic numerical model for the Amazon can be developed; this can be used to predict changes in the Amazon, which would be integral in directing environmental effort within the Amazon River Basin. Additionally, such a model would be beneficial for those who travel or live along the Amazon or use it to transport their commercial goods.

ACKNOWLEDGMENT

This research was done under Dr. Jorge Abad from the Department of Civil and Environmental Engineering through the University of Pittsburgh's EXCEL Summer Research Internship program. Special thanks goes to Christian Frias who has been very helpful in the understanding of content and the learning of different programs and methods used to analyze the satellite images. Extended thanks goes to the EXCEL staff and the rest of the graduate students in the Dr. Abad's laboratory who have aided the process of this research.

REFERENCES

1. Hoorn, C, et. al. "Amazonia through time: Andean uplift, climate change, landscape, evolution, and biodiversity", Science, 330, 2010, 927-931.
2. Latrubesse, E, "Patterns of anabranching channels: The ultimate end-member adjustment of mega rivers", Geomorphology, 101, 2008, 130-145.
3. Nicholas, A, "Morphodynamic diversity of the world's largest rivers", Geology, 41, 2013, 475-478.
4. Mertes, L, A, K, Dunne, T, Martinelli, L, A, "Channel-floodplain geomorphology along the Solimoes-Amazon River, Brazil", GSA Bulletin, 108, 9, 1996, 1089-1107.
5.]Hickin, E, J, "Mean flow structure in meanders of the Squamish River, British Columbia", Earth Science, 15, 1978, 1833-1849.

CHARACTERIZATION OF BENDS IN MEANDERING RIVERS

Kristin R. Dauer[1], Brian W. Hone[2], Ronald Guitierrez Llantoy[3], Jorge D. Abad[4]
Earth Processes and Environmental Flows (EPEF) Research Group
University of Pittsburgh, Swanson School of Engineering, Department of Civil and Environmental Engineering
Web: http://www.engineering.pitt.edu/EFML

[1]Student member ASCE, Ph.D student, Earth Processes & Environmental Flows (EPEF) Research Group, Department of Civil and Environmental Engineering, Benedum 718, 3700 O'Hara St, Pittsburgh, PA, 15261; email: krd33@pitt.edu
[2]Senior Undergraduate, Earth Processes & Environmental Flows (EPEF) Research Group, Department of Civil and Environmental Engineering, Benedum 718, 3700 O'Hara St, Pittsburgh, PA, 15261; email: bwh14@pitt.edu
[3]PhD, Earth Processes & Environmental Flows (EPEF) Research Group, Department of Civil and Environmental Engineering, University of Pittsburgh, Benedum 718, 3700 O'Hara St, Pittsburgh, PA, 15261; email: ro.gutierrezll@gmail.com
[4]Assistant Professor, Earth Processes & Environmental Flows (EPEF) Research Group, Department of Civil and Environmental Engineering, University of Pittsburgh, Benedum 731, 3700 O'Hara St, Pittsburgh, PA, 15261; email: jabad@pitt.edu

INTRODUCTION:

Human activities and development projects continually have an impact on the environment, including waterways. Factors such as increases in sediment laden flows, urbanization of natural rivers and the construction or removal of water control structures can all affect the historical and current properties of natural waterways. Some of these effects can be seen in the geometry of plan or bed forms and in river migration over time. The primary goal of this project was to collect and interpret data about these river morphodynamics in order to more effectively perform projects such as restoring impaired streams to more natural, stable conditions or reducing the urbanization effect on waterways. This goal was achieved through the development of a "meander toolbox" in MATLAB for analyzing river characteristics. The toolbox uses digitalized river banks and widths as input, calculates a mean centerline with wavelet analysis, and computes river bend statistics such as sinuosity, length, orientation, wavelength, and amplitude. In addition, the toolbox uses wavelet analysis to compute additional river bend properties like angular amplitude. The research team hopes to eventually incorporate river migration statistics over time and publish the toolbox in a scientific journal for use in the public domain.

METHODS:

The initial step in this project was to gather spatial river data to aid in developing the toolbox computation processes. Natural meanders were chosen from locations in the Southern US, South America, and Canada because they did not exhibit significant effects from urbanization and were undisturbed over long periods of time. Satellite data was collected for 13 river reaches, with 5 different years of data for each stream. This data was digitalized into stream-bank coordinates using AutoCAD and a mean centerline for each river and year was found using wavelet filter techniques developed by Mr. Gutierrez.

MATLAB code was then developed to accept the river centerline coordinates and mean width as input and calculate basic river characteristics such as the sinuosity (curvature) of each bend, length, bend orientation (upstream or downstream), bend wavelength, and bend amplitude. River bends were defined as the stretch of river between two inflection points of the mean river centerline. In addition to the basic calculations, additional MATLAB code was written to create a graphical user interface

(GUI) to allow the user to easily see and interpret the data utilized by the program. The GUI accepts input from the user, plots the river centerline data, plots bend limits and inflection points, and displays statistical results for basic river features. In addition, the user can elect to calculate river statistics based on wavelet analysis instead of numerical analysis. More features are expected to be added to the GUI in the future, including methods for centerline input over periods of time and calculation of river migration rates using curvilinear vectors.

RESULTS:

The meander toolbox and associated riverbank data was used to calculate bend characteristics for 13 natural river reaches in North and South America. These characteristics were verified by hand calculation and could be used to classify the river reaches as confined meanders, free meanders, or some combination of these two. Three meanders were selected (one of each type) for illustration: the Beaver River (Alberta, Canada) is classified as a confined, natural meander, the Pearl River (Mississippi, US) is a free meander, and the Red Deer River (Alberta, Canada) has both confined and unconfined characteristics[2]. A stretch of the Red Deer is shown below as it appears in the GUI window (fig. 1).

FIG. 1:

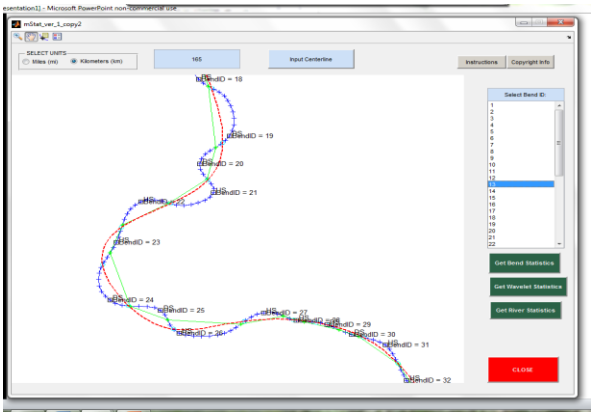

DISCUSSION:

While many authors have written articles or developed computer code that can be used to perform similar tasks to this project[1], the meander toolbox is a comprehensive tool that can aid designers in statistical analysis of meandering rivers. As such, it would be useful in a great variety of applications, including those in the academic as well as private sectors. The easy-to-use interface with graphical results represents an effective teaching tool as well as an overview of statistics about the river bends. This information is of great value when natural bend characteristics are compared to those in stream restoration or structural design. For example, river disturbances due to increased runoff from urbanization or the removal of aging dam structures could be quantified by the meander toolbox and mitigated properly due to an increased understanding of the migration process. This meander characterization could additionally be used to properly restore a river to a more stable condition after construction activities and to hold down the high cost of river restoration after such projects. It is hoped that the toolbox can be developed even further in the future to include features such as input of river centerlines over time and calculation of river migration rates using curvilinear vectors. This would provide an even more powerful calculation tool that could be used in any number of applications in waterways engineering.

REFERENCES:

1. Frascati, A., and S. Lanzoni (2009), "Morphodynamic regime and long-term evolution of meandering rivers." J. Geophys. Res., 114, F02002, doi:10.1029/2008JF001101.
2. "Evolution of Meander Loops" James C. Brice *Department of Earth Sciences, Washington University, St. Louis, Missouri 63130.* Geological Society of America Bulletin, v. 85, p. 581-586, *6* figs., April 1974

THE ANGAIT DEVICE;
A SIMPLE MEANS FOR DIAGNOSING GAIT DEFICICIENCIES

John Teoli
iMed Lab, Department of Electrical Engineering
University of Pittsburgh, PA, USA
Email: jot22@pitt.edu, Web: http://www.imedlab.org/

INTRODUCTION

Human gait, the pattern of limb movements during locomotion deteriorates with age and disease. Gait deficiencies leave many elderly people at above normal risk for spontaneous falls which can result in injuries or death. However, gait deficiencies are not easily diagnosed because gait is regulated by the integration of vestibular, visual, and proprioceptive sensory feedback which are all governed by different bodily systems. In order to analyze gait deficiencies one must collect a complete picture of the human gait.

The anGait device was designed to record all aspects of how people walk. It is an electrical device that is attached to a belt and communicates with a specially designed android application that records the data. The device features sensors to measure accelerometry, emotional response, heart rate, breathing, and stride interval. Previous studies have helped to determine the characteristics of healthy gait. The iMed Lab is now collecting data from elderly people with gait deficiencies to further understand these characteristics and to provide an easy way of diagnosing abnormal Gait.

METHODS

The study consisted elderly patients who have known gait deficiencies. They were healthy and cognitively active enough to perform several simple cognitive tasks and be able to walk freely or with a walker for at least a solid continuous minute. Data collection is still on going as we find more patients who fit these requirements. A complete population description will be made available once all the patients have been chosen.

The accelerometer used in the anGait device is a Hitachi h84c chip. The chip was located on the device itself, which should be centered along the patients spine. The Hitachi h84c collected data in three dimensions. The dimensional data was stored in three columns along with a reference voltage, which was used to convert the raw voltages to G units.

The GSR, often called Electrodermal Response in the medical world, measured skin conductance based on moisture levels caused by sweat. Skin conductance is an important parameter because sweat glands are controlled by the sympathetic nervous system. Therefore, it can be used as an indicator of physiological arousal. The device worked by measuring the resistance between two points on the subject's skin when a weak current is passed through it.

Like many GSR sensors, anGait collects its data through external sensors that subjects wear on their fingers. These sensors are made copper sheets attached to Velcro strips that the subject wears on two adjacent fingers. The sensors can be placed on any two fingers, but if the patient has large hands is may be necessary to use the pinky and ring fingers. It is also recommended that the sensors be placed near the middle of the finger and strapped tightly to prevent them from slipping off as the patient's hand gets sweaty. Each strip is connected to the anGait device by wires that are soldered to the inside of the copper.

The anGait device measured stride by making use of four different FSR, two of which were attached to the front and back of each foot pad. The sensors measured stride by voltage changes that occur when pressure is applied by each footstep. Each foot pad was connected to the device by a modified ethernet cable. However, only four of the eight copper wires in the cable were actually used.

The Electrocardiogram or ECG was used to measure the rate and regularity of heartbeats. The anGait device used a three pronged ECG which

were connected using the American Heart Association or AHA convention. The ECG signal was processed by a series of amplifiers and low pass filters starting with an AD624 instrumentation amplifier.

The respiratory belt was actually a third party device that the anGait used to collect respiratory data. The pneumotrace was strapped around the patient's chest in a way that allowed it to expand and contract with breaths, but not so tight as to cause discomfort.

DATA PROCESSING

The raw voltages were stored on the Android device columns separated by commas in a custom data format, .agt. The data was then moved from the Android to a computer via USB and converted to a Microsoft Excel comma separated data file. This file consists of 11 columns to store each sensor's information. Data collection is currently ongoing

RESULTS

The results can be graphed directly through Microsoft Excel for a visual representation. This data will be analyzed mathematically to provide more meaningful results in the near future. Figure 1 shows stride data from one of the footpads sensors, figure 2 illustrates changes in emotional response, figure 3 displays the electrocardiogram data, and lastly figure 4 contains the accelerometer data in the y axis.

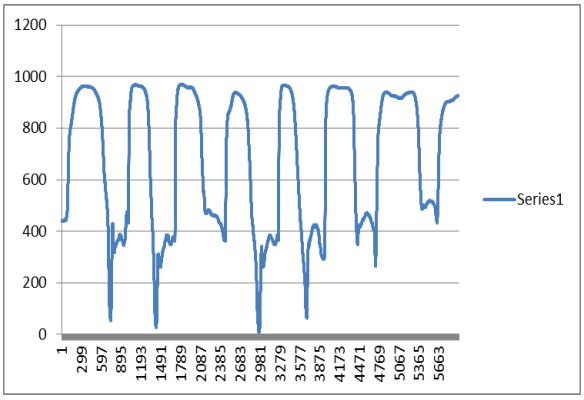

Figure 1: Stride Interval Data

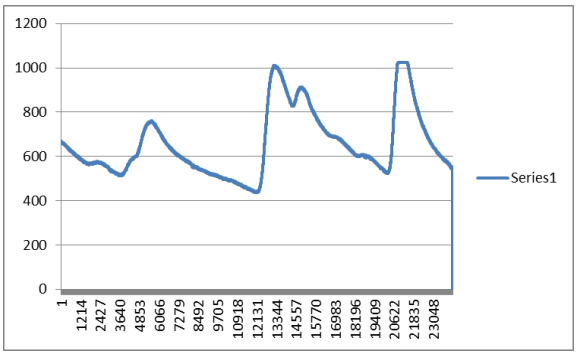

Figure 2: Emotional Response

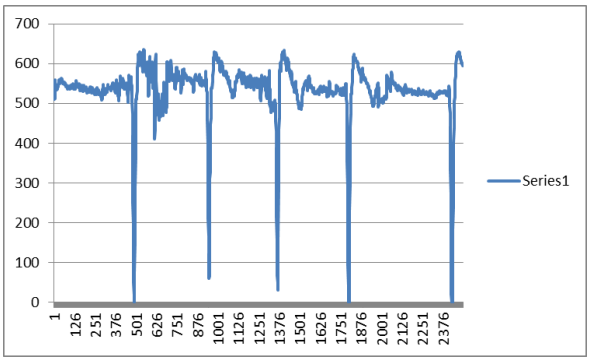

Figure 3: Electrocardiogram data

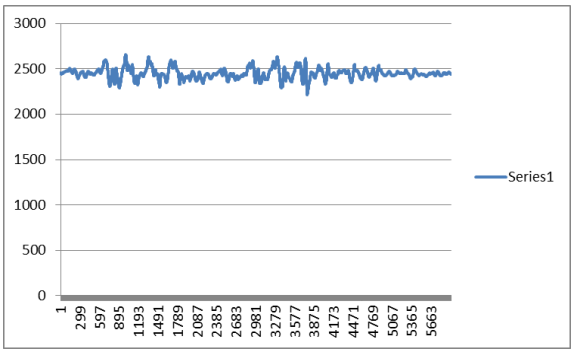

Figure 4: Accelerometry Data in Z axis

DISCUSSION

Unfortunately data collection is still ongoing so I cannot elaborate on results at this time. I will, however, continue working in the iMed lab to complete the study. The work done this summer was mostly understanding and repairing the anGait device which was left in a state of disrepair by previous students.

ACKNOWLEDGEMENTS

Subjects were screened at the Cumberlan Crossing Retirement Community. I would like to thank Dr. Sejdic for allowing me to work in his lab this summer and all of the Grad Students who helped me get the device working.

SYNTHESIS OF GRAPHENE FOR USE IN APPLIED ELECTRONIC DEVICES

Donald K. Voland and Minhee I. Yun
Nanoelectronics and Devices Laboratory, Electrical and Computer Engineering
University of Pittsburgh, PA, USA
Email: dkv3@pitt.edu

INTRODUCTION

Graphene, a two-dimensional plane of graphite, has become a lead interest in materials research across the globe [1]. Over the previous decade, graphene research has grown at a staggering pace. So far, graphene has exhibited a myriad of remarkable properties. Not only is graphene both the thinnest and strongest material known to man, but it also shows record thermal conductivity and stiffness. At the same time, graphene demonstrates superior electrical and optical properties such as a giant intrinsic mobility and high transmittance [1]. With improvements in the synthesis of graphene, engineers will have the capability to fabricate novel devices that will outperform previous generations in terms of sensitivity, cost, and applicability.

In order to fabricate the next generation of devices, a method for the controlled synthesis of mono/bi/few-layer graphene must be researched. Since equipment parameters such as size, max temperature, and flow rates vary from lab to lab, there is no standard recipe for graphene growth. The following discussion will focus on the process of determining the optimum conditions for which graphene can be grown with ambient pressure chemical vapor deposition (APCVD). The growth parameters that will be varied are the flow rates of hydrogen, methane, and argon, annealing, growth, and cooling times, and surface roughness.

EXPERIMENTAL

The graphene was grown on 1 cm^2 copper foil placed on a quartz boat in a 4' long, 2'' wide quartz tube in a Carbolite® furnace. As-given copper featured large ridges from the manufacturing process as well as surface oxidation. In order to remove oxidation and flatten the surface, the copper was lightly polished with KimWipes® soaked in dilute copper etchant (CE-100, Transene Company Inc.) for about an hour. Following the etching, the copper was cleaned using deionized (DI) water and blown dry. In these experiments, the growth temperature varied between 1000°C and 1057°C. To reach this temperature, the copper was slowly heated for about 40 minutes. Once at growth temperature, the copper was allowed to anneal for 30 to 60 minutes. The annealing process aided in further reducing surface roughness of the copper. Next, methane was introduced into the system. The flow rate of the methane could range between 1 SCCM and 50 SCCM while the H_2 and Ar ranged between 1-100 SCCM and 1-500 SCCM, respectively. Growth time varied between 5 seconds and 30 minutes. Air-cooling typically took 20 minutes to an hour, depending on how much and when the furnace was opened. By the end of the research, it was found that cooling could be quickly and safely done by opening the furnace shortly after growth was complete.

For characterization, the graphene was transported onto a SiO_2 substrate via a floating-PMMA transfer method. First, the copper foil was taped onto a piece of PET and 450 PMMA A4 (MicroChem) was spin-coated onto it for 5 sec at 500 rpm, followed by 30 sec at 1500 rpm. Once dry, the sample was cut away from the PET and placed in a CE-100 etchant bath for 1 hour to remove copper. After etching, the sample consisted of a thin layer of PMMA on graphene. Carefully, the sample was transferred through three DI water baths. Placed onto the SiO_2 substrate, the sample was then dried and placed in an oven at 80°C for 30 minutes to remove remaining water. Still warm, the substrate was placed in an acetone bath for about 10 seconds to remove the majority of the PMMA and a second bath for 30 minutes to remove residues. Finally, the sample was immediately blow-dried.

DISCUSSION

Over the course of the research, two general trends have been observed that are in accordance with recent discoveries. First, the synthesis of the graphene is an incredibly quick process. In Han's tests, the layer number would reach a maximum

value in which growth stopped [2]. Here, samples with growth times under a minute are nearly identical with those of 10+ minutes in terms of graphene thickness. Like Han, many believe that growth is a self-limiting process, determined by copper surface roughness and gas flow rates [2]. In Vlassiouk's tests, hydrogen was been shown to act as both a catalyst and an etchant [3]. Therefore, varying the H_2 flow rate can aid in adjusting how much carbon, the constituent atoms of graphene, copper is willing to absorb. Although growth time was an important factor in Han's and Vlassiouk's experiments, it did not seem to significantly influence synthesis past the first couple seconds for our system [2], [3]. Due to this, varying the growth time became less important as the research continued. To better control layer number, focus shifted towards flow rate adjustments.

Second, H_2 has proved to be a good catalyst for the growth of multilayered graphene while being a poor choice for single and bilayer growth. Choi suggested that due to copper's very low carbon solubility, only a few layers of carbon would be capable of being absorbed without the aid of a catalyst such as H_2 [4]. With H_2 present, copper's solubility is increased, making single and bilayer growth difficult without a vacuum [4]. With this information in mind, Choi developed a H_2-excluded process to limit growth to single and bilayer [4]. Tailoring the process for our equipment, few-layer graphene growth was accomplished.

Using a flow ratio of 500:5 ($Ar:CH_4$) for 10 minutes, the graphene shown in Figure 1 was grown. The height difference between the lower regions and the upper plains averages between 1.3 nm and 2 nm. When using this data to determine the number of layers, there are two possibilities to consider. First, if the lower regions are etched, then it can be assumed it is the SiO_2 that is shown and the thickness is in fact 1.3-2 nm. Since graphene on SiO_2 has spacing of 0.5-1 nm and graphene-graphene spacing is 0.335 nm, this would mean it is 2-6 layers [5]. However, if the lower region is the first layer of graphene, then there should be 2-4 layers. In a replication of the sample, the etching pattern was gone and large islands were visible with a thickness of 0.7-2 nm (2-6 layers). This suggests that the upper planes may be due to a large number of nucleation sites at which multiple layers can form. In order to come to a conclusion on the nature of the graphene, further testing must be completed.

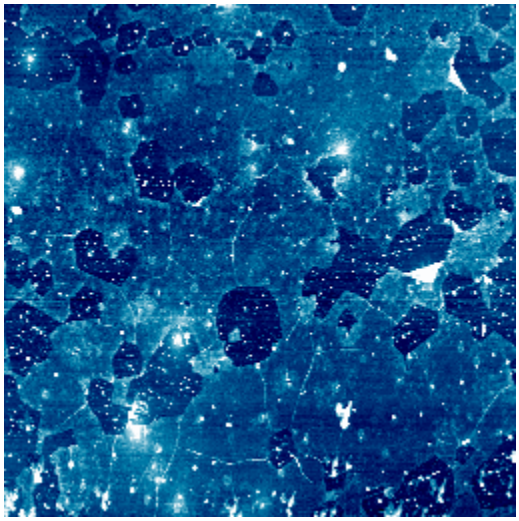

Figure 1: AFM scan of graphene grown via the H_2-excluded process. The lighter regions represent higher elevation.

FUTURE WORK

To fully characterize the graphene, additional testing must be done using AFM techniques and Raman microscopy. Knowing the true layer count will allow for controlled growth by the manipulation of flow rates. Finally, electrical and optical qualities of the graphene will be measured.

In the next phase of this research, the graphene synthesis method will be optimized for the creation of graphene suitable as the main component in the next generation of infrared (IR) sensors. Equipped with graphene, these sensors will have superior sensitivity and practicality. Avoiding the high costs of rare earth metals, advanced sensors will also be capable of widespread use. Furthermore, detectors incorporating these materials should be operable in ambient conditions with detection capabilities in the mid-IR range of 7 to 14 μm emitted from the human body. In the future, graphene IR sensors will have applications in biomedicine, astronomy, military, and more.

REFERENCES

1. A. Geim. *Science*, **324(5934)**, 1530-1534, 2009.
2. Han et al. *Nano Letters*, **11(10)**, 4144-4148, 2011.
3. I. Vlassiouk et al. *ACS Nano*, **5(7)**, 6069-6076, 2011.
4. M. Choi. *MIT*. 2012.
5. K. Xu et al. *Science*, **329**, 1188-1191, 2010.

THREE MAGNESIUM-RARE EARTH ALLOYS AS BIOMATERIALS

Devon Albert, Elmar Willbold and Frank Witte
Laboratory for Biomechanics and Biomaterials, Department of Orthopaedic Surgery
Hannover Medical School, Hannover, Germany
Email: dla16@pitt.edu, Web: http://www.lbb-mhh.de/

INTRODUCTION

Magnesium alloys are being extensively researched for use as orthopedic implants. The bone-like mechanical properties and *in vivo* degradability of magnesium alloys make them a desirable biomaterial. Furthermore, the presence of a magnesium alloy implant does not impair wound healing. Both tissue restoration and bone regeneration occur while the magnesium alloy degrades [1]. In fact, in vivo studies of magnesium implants have reported enhanced bone growth occurring as a result of the implant. However, Janning et al. concluded that enhanced bone growth around magnesium alloy implants is mainly due to the presence of magnesium hydroxide which results from the corrosion of any magnesium alloy [2]. Despite this, the introduction of rare earth elements below toxicity levels has been positively correlated with cell growth and proliferation [3-4].

Alloying magnesium decreases the element's corrosion rate, limiting the evolution of harmful hydrogen gas into the body [2]. Specifically, alloys containing rare earth elements have been shown to slow corrosion rates, making this type of magnesium alloy more biocompatible [5]. Because of the promise of rare earth elements as a component of biocompatible magnesium alloy implants, the purpose of this study is to observe the effect of magnesium lanthanum, magnesium neodymium, and magnesium cerium alloys on bone tissue.

METHODS

Nine female rabbits (New Zealand White) received magnesium alloy implants in both knee joints. Three types of magnesium alloys were randomly divided between the rabbits so that three rabbits obtained MgLa implants, three rabbits obtained MgNd implants, and three rabbits obtained MgCe implants. Surgery was performed on both knees of each rabbit to insert the magnesium alloy cylinders into the medial femur condyle. Animals were sacrificed at 4 weeks after surgery. All animals in each group were used for histomorphology providing 6 specimens with each type of implant and a total of 18 specimens.

The medial condyles were dissected en bloc from the knee joint and fixed in methyl-methacrylate. The tissue blocks were sectioned using a RM 2155 microtome. Five µm thin sections were cut and placed onto poly-L-lysine-coated glass slides. Sections from each specimen then underwent one of three types of staining such that each specimen produced at least one section with each type of staining. A von Kossa staining was used to detect bone mineral deposits in a section. A toluidine blue staining was used to detect osteoid. A tartrate resistant acidic phosphatase (TRAP) staining was used to detect osteoclasts.

Photomicrographs were taken with a Zeiss Axioskop 40. For each stain, a photomicrograph of one section from each specimen was evaluated using AxioVision software. In each section, a 750µm broad tissue seam around the implant hole was defined as the region of interest. However, cortical regions were selectively excluded from data analysis. Within the 750µm ring, the parameters bone volume/tissue volume (BV/TV), osteoid surface per bone surface (OS/BS), and osteoclast surface per bone surface (OcS/BS) were measured and determined according to international standards.

There was not a control group in this study. However, Janning et al. used an almost identical protocol to study $Mg(OH)_2$ implants in rabbits and obtained control data from 2 animals [2]. Based upon the similar study design and procedures, we feel the control results from Janning et al. can also be compared to our results.

RESULTS

The histomorphometric results are shown in Figure 1 below. The control group from Janning et al. had

higher parameter values (BV/TV 72.53±9.11%, OS/BS 25.00±11.45%, OcS/BS 3.89±0.72) than all of the implants [2]. Among the implants, MgLa had the highest values except for OcS/BS (BV/TV 60.31±13.40%, OS/BS 15.45±21.11%, OcS/BS 1.11±1.55%). MgCe had the median values except for OcS/BS which was the highest among the implants (BV/TV 58.42±7.66%, OS/BS 11.88±13.88%, OcS/BS 1.16±1.09%). MgNd had the lowest values (BV/TV 54.68±7.02%, OS/BS 6.38±9.34%, OcS/BS 0.54±0.56%). It is important to note that necrotic tissue was not observed in the bone around any implants.

DISCUSSION

This study demonstrated that the MgLa, MgNd, and MgCe implants were not toxic and did not result in the significantly enhanced bone growth within the immediate area of the implant as observed in previous studies. The amount of osteoid surface observed was greater for the control group than all of the implant groups. This is the opposite of the enhanced bone growth reported in similar studies [2,5] and could be a result of vascularization differences between the control group and implant specimens. However, Willbold et al. noted a similarly decreased level of osteoid after the RS66 alloy was implanted in rabbit bone for 4 weeks and attributed this finding to the alloy's slow corrosion rate [1]. Another possible explanation is a high concentration of magnesium inhibiting osteoblast activity. It is important to reiterate that these results include only the 750μm ring immediately around the implant. Enhanced bone growth was seen in some specimens outside of the region of interest, but was not included in the results. The reduction in OcS/BS values for the specimens with implants when compared to the control group was also found in the study published by Janning et al. [2].].

The MgNd implant had the lowest values for BV/TV, OS/BS, and OcS/BS which suggest the alloy has the slowest corrosion rate. However, all implants had high standard deviations for OS/BS and OcS/BS and a limited number of specimens so the comparative corrosion rates of the alloys should not be interpreted as definitive. Widening the region of interest around the implant and increasing the number of specimens could yield more significant results. Future research should also be conducted to quantify the corrosion rates of the alloys and determine the mechanism which prevented enhanced bone growth.

REFERENCES

1. Willbold et al. *Acta Biomat* **9**, 2013.
2. Janning et al. *Acta Biomat* **6**, 1861-1868, 2010.
3. Xin et al. *Biol Trace Elem Res* **152**, 82-90, 2013.
4. Wang et al. *Biol Trace Elem Res* **75**, 265-275, 2000.
5. Witte et al. *Biomaterials,* **26**, 3557-3563, 2005.

ACKNOWLEDGEMENTS

We would like to thank the members of the Labor für Biomaterialien for all of their help and support during this project.

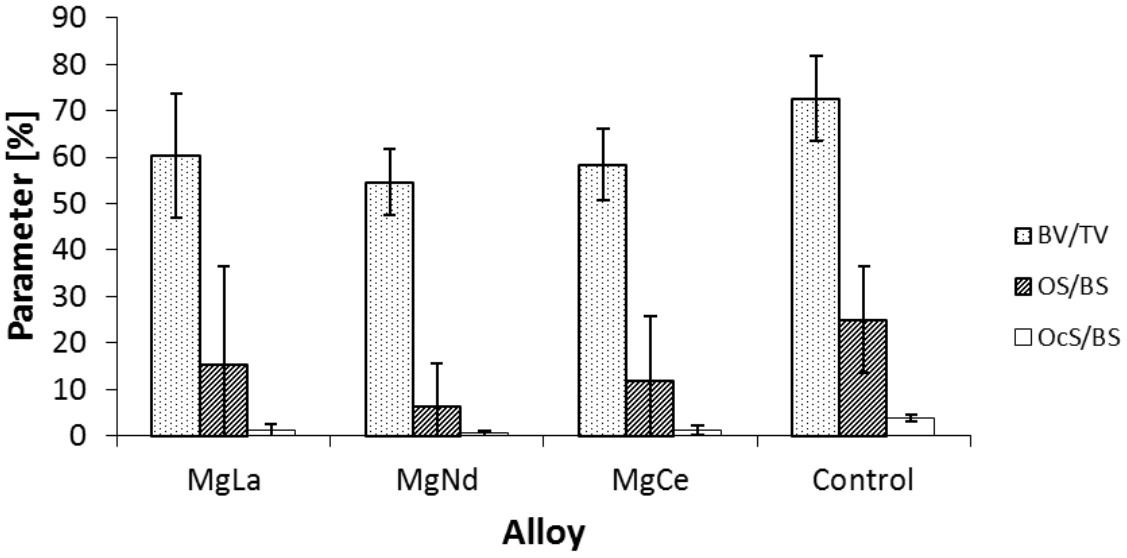

Figure 1: The average ± standard deviation BV/TV (dotted), OS/BS (diagonal lines), and OcS/BS (white) of the specimens with MgLa, MgNd, and MgCe implants as well as the control results from Janning et al. [2].

ANTIBACTERIAL EFFECTS AND CYTOTOXICITY OF VARIED SILICA NANOPARTICLES

Liza Bruk, Hendrik Fullriede, and Sebastian Grade
CrossBIT, Department of Prosthetic Dentistry and Biomedical Materials Science
Hannover Medical School, Hannover, Germany
Email: lab154@pitt.edu

INTRODUCTION

The present need for biocompatible, antimicrobial materials for use in dental implants is filled with anisotropic silica nanoparticles. Spherically shaped anisotropic silica nanoparticles are commonly used as dental fillers [1]. Silica nanoparticles are considered to be biocompatible and are approved by the FDA as generally safe. Hydrophilic silanol (SiOH) groups cover the surface, leading to repulsive interactions between the inorganic fillers and the hydrophobic monomers of the resin. This results in decreased mechanical properties – hardness, flexural strength, and wear resistance – of the composite material [2]. Surface functionalization of the silica fillers with organic methacrylate groups is applied to decrease the repulsive interactions and prevent this negative effect.

Commercially available silica nanoparticles are spherically-shaped, nonporous, and manufactured by flame pyrolysis. The silica nanoparticles are characterized by a hexagonal ordered pore system. These pores have different organic or inorganic antimicrobial agents – namely silver, chlorhexidine, and others – incorporated into them to provide the composite with antibacterial properties. Silver nanoparticles are known to be relatively nontoxic and safe antibacterial agents for the human body [3]. Chlorhexidine is a known antiseptic, disinfectant, and preservative [4].

METHODS

This study tested nine different silica particle types - SiO_2, SiO_2Ag, SiO_2CHX, SiO_2SO_3HCHX, SiOH, NH_2, H_2OSH, NH_2+CHX, SH+CHX. Silica nanoparticles were ultrasonicated for 10 minutes at 100% power for a homogenous suspension (Omnilab T710DH). The appropriate amount of particle suspension to achieve desired concentrations was put into labeled falcon tubes and the complementary volume of heated Muller-Hinton agar was added to the falcon tubes for total volume in each tube to equal 10mL. The concentrations tested were 50, 100, 200, and 300µg/mL. For each particle type and concentration, four plates of diameter 35mm were prepared with 2mL of the agar-particle mixture. Four plates without nanoparticles were used as negative controls. Following an overnight culture of 100µL of *S. aureus* in 5mL TBS medium, the bacteria's optical density (OD) was measured and diluted accordingly to achieve 1:1000 dilution of a 0.1 OD. Each agar plate was coated with 100µL of bacteria suspension and cultivated in humid atmosphere for 24hr at 37°C, after which observations of colony forming units were recorded and plates photographed using a gel documenter (Molecular Imager Gel Doc XR, Biorad).

The particle types that showed that most antibacterial effect were tested on *S. mutans* biofilm. Mature biofilm was grown using two different approaches: particles added to an overnight culture and biofilm grown by adding particles directly to a mixture of *S. mutans* and medium. For each method, one plate was grown without particles as a control, one with SiOH silica particles as a control, and two each with the two nanoparticle varieties. The concentration of nanoparticles in each instance was 500µg/mL. Antibacterial effect on biofilm formation was recorded by inverse confocal laser scanning microscope (Leica DM IRB, Leica).

Human gingival fibroblasts (HGFib) were cultivated and maintained in Dulbecco's Modified Eagle's Medium (DMEM) at 37°.

Cells were grown for 24hr in 96-well plates at an initial density of 3000 cells per well in 100µL of DMEM. Nanoparticles were mixed with DMEM to achieve concentrations that demonstrated antibacterial effect. The existing medium was replaced with 100µL of the DMEM-nanoparticle mixture in each well, with four wells for each concentration. Eight wells with only DMEM were used as the negative control. An MTT assay was performed according to manufacturer protocol to determine the percentage of living cells remaining after incubation with particles for 24hr at 37°C. First, 10µL of the staining solution are added to each well. After four more hours of incubation, 100µL of solubilization solution were added to each well and the well plate was again incubated overnight. The absorbance was measured at a wavelength of 580nm, with 650nm as a reference, using a fluorescence microplate reader (Infinite F200, Tecan). An additional well plate was prepared and assayed with only particle suspension and no cells, to eliminate error in absorbance readings from the absorbance of the nanoparticles themselves.

RESULTS

SiO_2, SiOH, SiO_2CHX, NH_2 and H_2OSH particles showed no effect on bacterial growth. SiO_2Ag particles showed an antibacterial effect starting at 100µg/mL. SiO_2SO_3HCHX particles showed an antibacterial effect starting at 100µg/mL. NH_2+CHX and SH+CHX particles showed an antibacterial effect starting at 50µg/mL.

In the case of nanoparticles added to biofilm after 24 hours of growth, the resulting biofilm was detached and impossible to document. In biofilm grown by adding nanoparticles directly into the bacteria suspension, both NH_2+CHX and SH+CHX nanoparticles showed a significant antibacterial effect on the biofilm at 500µg/mL.

At all concentrations, SiO_2Ag, NH_2+CHX, and SH+CHX showed almost complete cell death. Silica (SiOH and SiO_2) did not exhibit significant cytotoxicity. All other nanoparticle types had significant levels of cytotoxicity, with 22-53% live cells.

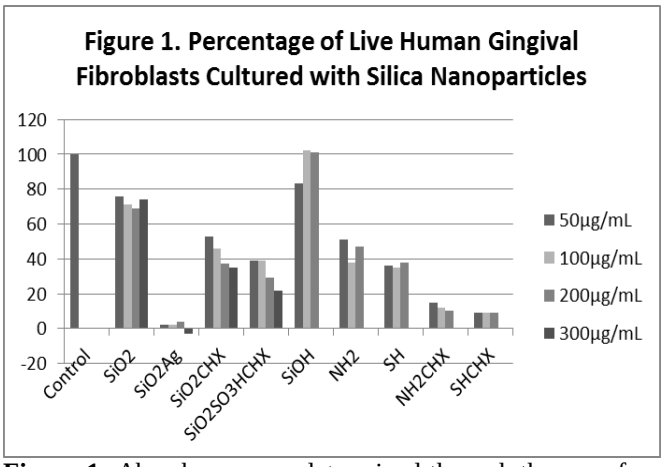

Figure 1: Absorbance was determined through the use of an MTT assay, at wavelengths of 580nm and 650nm (reference). Higher absorbance values indicate larger amounts of live cells; lower absorbance values indicate cells are dead and/or under stress. Percentage was determined in comparison to the negative control (cells in medium with no nanoparticles).

DISCUSSION

A previous study [5] showed silver nanoparticles to have effective antibacterial properties on four different bacteria in lower concentrations than those found to be effective in this study. The previous study showed SiO_2Ag nanoparticles to have a statistically significant antibacterial effect on *S. aureus* at 70µg/mL. Antibacterial effect on other bacteria types began at even lower concentrations. In the present study, the antibacterial effect of SiO_2Ag began at 100µg/mL. The previous study concluded a narrow therapeutic window between 10 and 20µg/mL. As *S. aureus* was the most resistant to the antibacterial effects of silver nanoparticles in the previous study, it may be helpful to retest with less resistant bacteria to determine a potential therapeutic window.

REFERENCES

[1] Klapdohr et al. *Monatsh Chem.* **136,** 21-45, 2005.
[2] Tian et al. *Dent. Mater*. **24,** 235-243 2008.
[3] Hwang et al. *FEBS Journal*, **279,** 1327-1338, 2012.
[4] Russell A.D. *Infection,* **14,** pp. 212-215, 1986.
[5] Grade et al. *Adv Eng Mater.,* **14,** 231-239, 2012.

A Microfluidic Study for Osteoblast Cell Responses

Graduate Student: Mahdis Shayan,
PI: Youngjae Chun, PhD
Undergraduate Researcher: Aniket Patel
BioManufacturing and Vascular Device Laboratory, University of Pittsburgh, Pittsburgh, PA

INTRODUCTION

Mirroring *in vivo* studies with *in vitro* experiments is a vital technique that is pertinent to studying various physiological processes at a more micro level. When performing *in* vitro studies, many problems are encountered. Diffusive limits in 2D culture models lead to intra-culture transport hindrance of media. 2D *in vitro* models lack the topology, dimensionality, and rigidity that cells respond to for *in vivo* studies. To overcome the limits of traditional 2D models, a 3D model microfluidic perfusion platform was developed and validated. It was hypothesized that the physiological microfluidic model equipped with a continuous flow and temperature control system will prove to be a successful platform technology, which will lead to further studies to determine the optimal fenestration geometry of stent grafts in a real-time, inexpensive and versatile way.

To test the function of the microfluidic system, osteoblasts were utilized. Their vitality while in the micro-incubation system was observed and the validity of the microfluidic system was then determined. To satisfy the metabolic needs of the osteoblasts, cell media (MEM) was put through a mini-pump at an optimal flow rate, thereby mimicking circulation. The osteoblasts were then stimulated with varying voltages in the range of 0.0-1.0 V to determine if an applied voltage has any effect on osteoblast vitality.

METHODS

1. *Design of microfluidic system:* A micro-incubation platform for RC-40 chambers, model DH-40iL, was ordered from Warner Instruments, Inc. Design of the microfluidic system included a platform, 35 mm culture dish with an adapter ring, and a cover. The assembly was mounted onto a microscope (name of microscope).

1.1 *Platform:* The 35 mm culture dish was placed directly onto the platform. Two resistive heating elements were inserted into the platform, in addition to a control thermistor. Input and aspiration tubes were connected to the platforms.

1.2 *Cover:* The cover served the purpose of providing an enclosed micro-incubation system. The window cover glass is positioned via a c=recessed annular lip and is held in place using a rubber o-ring. When in place, the cover glass seals a 36 mm window useful for illumination purposes. The cover components are shown below:

A) Gas entry port: connects to atmospheric control system

B) Heater block notches: accommodate heating blocks; also serve to orient the cover onto the platform

C) Access port: provides a vent for waste gasses or provides easy entry for special tubing

D) and E) Perfusion tubes: aspiration and input, respectively

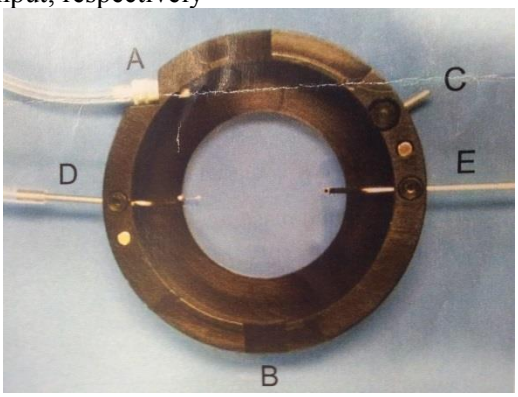

Figure 1. *Pictorial representation of cover.*

1.3 *Heat:* Warner Instrument's Single Channel Heater Controller (Model TC-324B) was used for thermal regulation of the culture disk inside the platform. Two resistive heating elements from the Heater Controller attached to the platform. Additionally, thermistors were placed on the platform to monitor the temperature of the micro-incubation system.

2. *Validation of microfluidic system:* Osteoblasts (specific type?) were placed into

the 35 mm culture dish with MEM media. The system temperature was set to 37 °C. The amount of CO_2 utilized was 5%, which maintained a pH of approximately 7 of the culture media. MEM media was pumped into the micro-incubation system via a variable mini-flow pump (Pump II – Low Flow, Control Company) at a rate of 0.36 ml/min. Cell vitality and morphology was monitored using time-lapse videomicroscopy, optical and SEM imaging.

3. *In vitro study:* MC3T3 cell culture was placed on culture dish containing a cast silk sample. The temperature of the micro-incubation system was set to 37° with 5% CO_2. Cell vitality and morphology was monitored using time-lapse videomicroscopy and subsequently via SEM imaging.

RESULTS

SEM images indicate that the miroincubation system properly worked to a certain degree. The MC3T3 were thriving for a period of 3 hours, but for any time beyond 3 hours it became visible that MC3T3 count was diminishing.

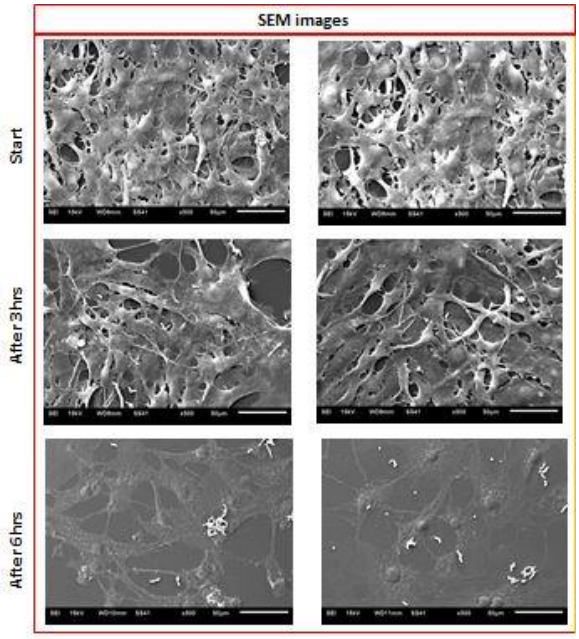

Figure 1. SEM images taken at two different location on the micro-incubation platform at 3 different time periods.

At the 6 hour time mark, the MC3T3 cell density is clearly declining. As the experiment continued, even less cells were observed.

DISCUSSION

The goal of the experiment was realized. The design of the microfluidic was validated for the time period of 3 hours. After the initial 3 hour time period, cell density began declining. The death of the MC3T3 cells after the 3 hour time period can be attributed to the contamination the cells experienced when performing the optical imaging. When the optical imaging was performed, the cover the micro-incubation platform needed to be removed, thereby exposing the cells to the air. Once the cells are exposed to the surrounding environment, contamination is always possible. After every 3 hours, the micro-incubation platform was opened and this largely contributed to the death of more cells as the experiment progressed.

Previous *in vivo* experiments that utilized cast silk as a base for cell growth showed similar results to the experiment performed for the first 3 hours. Cell behavior in 3D models has been shown to closely reflect cell behavior in *in vivo* studies for a short time period. To increase the time period that the *in vitro* study can mimic the *in vivo* study, the problem of contamination must be fixed.

REFERENCES

[1]Jelena Vukasinovic, Kacey Cullen, Michelle LaPlaca and Ari Glezer,. 2009. A microperfused incubator for tissue mimetic 3D cultures. Biomed Microdevices, 11:1155-1165.

[2] Cyril Picard, Vanessa Hearnden, Marzia Massignani and Sarra Achouri. 2010. A micro-incubator for cell and tissue imaging. BioTechniques, 48:135-1358.

ACKNOWLEDGEMENTS

All work was done under the guidance of Dr. Chun and Mahdis Shayan at the Materials Science Engineering Laboratory at the University of Pittsburgh.

Multi-Armed Bandit with Correlated Rewards

David Eckman (dje14@pitt.edu) and Denis Saure (dsaure@pitt.edu)
Deptartment of Industrial Engineering, University of Pittsburgh

I. Introduction

An existing gap in the literature of multi-armed bandits (MABs) is for settings with correlated arms in which the rewards of one arm provide information about those of other arms. Many traditional MAB policies assume independence between arms and therefore cannot exploit this information. As a result, these policies may suffer excessive exploration or converge upon a suboptimal arm. A working framework for correlated MABs would be valuable for settings in which the assumption of independence between arms is unrealistic or when the selection of arms is combinatorial. Such a framework could be also used to solve MABs with objective functions characterized by both the mean and covariance of rewards. A straightforward application would be the selection of an optimal assortment of webpages to display in response to a user query. An information retrieval system would use a MAB subroutine to select webpages in a way that maximizes the number of "click-throughs" for a fixed level of diversity. The similarity, or novelty, of a page when compared to others would then be described by the correlation between arms.

II. Problem Formulation

We study a variation of the MAB in which an operator attempts to interdict the efforts of an oracle-like adversary by learning from the adversary's prior selections. Formally, there are K arms with rewards $X_t = [X_{1,t}, \ldots, X_{K,t}]^T$ distributed according to a multivariate normal (MVN) $\mathcal{N}_K(\mu, \Sigma)$ with mean vector $\mu := [\mu_1 \ldots \mu_K]^T$ and covariance matrix $\Sigma := (\Sigma_{ij})_{K\times K}$. In this matrix, the diagonal elements denote $\Sigma_{ii} = \sigma_i^2$, the variance for rewards of arm $i \in \{1, \ldots, K\}$, and the non-diagonal elements denote $\Sigma_{ij} = \sigma_i \sigma_j \rho_{ij}$, the covariance of rewards for arms i and j, $i \neq j$. At a time period t, the operator selects a subset $\mathcal{S}$ of $M < K$ arms to block and leaves the remaining $K - M$ arms for the adversary. The adversary and operator then observe realizations for all unblocked arms and the adversary obtains the maximum reward: $\max_i \{X_{i,t} \,|\, i \notin \mathcal{S}\}$. Define $\mu_{\mathcal{S}_k}$ to be the expectation of the maximum reward among all unblocked arms when the controller selects subset $\mathcal{S}_k$, $k \in \{1, \ldots, {}_KC_M\}$ where ${}_KC_M = \binom{K}{M}$.

The operator's objective is to learn the set of M vital arms which minimize the expected maximum reward over all unblocked arms, thereby minimizing the adversary's *total reward* calculated by the equation

$$E[S_t] = \sum_{k=1}^{{}_KC_M} \mu_{\mathcal{S}_k} E[T_t(\mathcal{S}_k)]\,,$$

where S_t is the sum of observed rewards up to time t, and $T_t(\mathcal{S}_k)$ is the number of times the operator selects subset $\mathcal{S}_k$ in the first t time periods. A complement to the measure of total reward is *total regret*, the expected loss for a policy given that it does not always select the optimal subset of arms. Total regret is given by the equation $R_t = E[S_t] - \mu_{\mathcal{S}_{k^*}} t$, where $\mathcal{S}_{k^*}$ is the subset which minimizes the maximum reward over arms not in $\mathcal{S}_{k^*}$.

We consider the case where $M = K - 2$, implying the operator leaves two arms for the adversary. [Clark, 1961] presented an exact formula for ν_1, the expectation of the maximum of two normal random variables. Clark's formula shows that ν_1 depends on components of both the mean vector (μ_1 and μ_2) and the covariance matrix (σ_1, σ_2, and ρ). For fixed means and variances, ν_1 is maximized when $\rho = -1$ since when arms are negatively correlated, it is more likely one of the arms will take a high value for a given realization. Because of this dependency on ρ, it is possible for a policy that assumes independence ($\rho = 0$) to converge upon a sub-optimal solution.

III. Methodology

A. Bayesian Framework

We take a Bayesian approach, learning from past observations by maintaining priors distributions for μ and Σ and using incomplete data methods to draw inferences about the posterior distributions. We use the well-known conjugate priors for the multivariate normal: an inverted-Wishart given by $p(\Sigma) \sim \mathbf{IW}(\Psi, m)$ and a MVN given by $p(\mu|\Sigma) \sim \mathcal{N}_K(\nu, (1/\kappa)\Sigma)$, for hyperparameters Ψ, m, ν, and κ.

Let Y be an $T \times K$ matrix in which each row $y_1, \ldots, y_K$ is an independent realization of the distribution $\mathcal{N}_K(\mu, \Sigma)$. For complete observations we can calculate $\bar{y} := (1/N)\sum_{i=1}^N y_i$ and $S := (1/N)\sum_{i=1}^N (y_i - \bar{y})(y_i - \bar{y})^T$, the sample mean and sample covariance, respectively. From [Schafer, 2010], the updated posterior densities for Σ and μ are

$$p(\Sigma|y) \sim \mathbf{IW}\left(\Psi + NS + \frac{N\kappa}{N+\kappa}(\bar{y} - \nu)(\bar{y} - \nu)^T, N + m\right),$$

$$p(\mu|\Sigma) \sim \mathcal{N}\left(\frac{1}{N+\kappa}(N\bar{y} + \kappa\nu), \frac{1}{N+\kappa}\Sigma\right).$$

When data is missing, we partition each row y_i into disjoint subsets y and z corresponding to the observed and missing data, respectively. To complete each observation, we turn to algorithms which generate multiple imputations of z.

B. Data Augmentation Algorithm

The data augmentation (DA) algorithm proposed by [Tanner and Wong, 1987] is a Markov chain Monte Carlo (MCMC) algorithm for imputing missing values. The algorithm iteratively updates a mean vector $\hat{\mu}$ and covariance matrix $\hat{\Sigma}$ which serve as estimates of the underlying MVN distribution. The algorithm begins by drawing a set of missing values from the conditional $p(z|y,\theta)$ where $\theta = (\hat{\mu}, \hat{\Sigma})$ is the current estimate of the true parameters. The augmented observation $x = (y, z)$ is then used to update the hyperparameters of the posterior density for $p(\theta|y,z)$. A new $\hat{\mu}$ and $\hat{\Sigma}$ are then drawn from the updated posterior and the process is repeated, thereby creating a Markov chain of values (z_i, θ_i) which converges in distribution to $p(z,\theta|y)$. The process is repeated for rm iterations where m is the number of desired imputations and r is number of iterations after which the Markov chain has converged. The imputed values for every rth iteration are effectively independent draws from $p(z,\theta|y)$, [Schafer and Olsen, 1998]. These m imputations then form a mixture of posterior densities which are averaged to determine our estimate of $p(\theta|y)$.

C. Sequential Imputation Algorithm

Another algorithm related to DA is the sequential imputation (SI) algorithm proposed by [Kong et al., 1994]. Unlike DA, the SI algorithm sequentially imputes the missing data points from each observation using the empirical mean and covariance. The algorithm maintains m independent augmented data sets, each with an associated weight $w(j)$, $j \in \{1,\ldots,m\}$, which is initially set to $p(y_1)$. After each time period, the weights are updated as $w_t(j) = w_{t-1}(j)p(y_t|y_1, z_1^*, \ldots, y_{t-1}, z_{t-1}^*)$. The posterior distribution $p(\theta|y)$ again can be estimated by the weighted average of the mixture of updated posteriors from the data sets. Normalizing the weights between time periods ensures greater accuracy since the weights can otherwise diminish rapidly.

IV. Results

We tested four ϵ_t-*greedy* policies [Sutton and Barto, 1998] in which the operator either selects the pair with the lowest index or selects a pair at random with probability $\epsilon_t := cK/t$, where c is an exploration constant.

NoClark–Ind: Assumes independence between pairs of arms. Uses empirical averages as an index for a pair of arms. Updates the sample average and number of times a pair has been tested.

Clark–Ind: Assumes arms are individually independent, but information for a pair can be used to update indices on the subordinate arms. Uses ν_1 as an index for each pair of arms based on the estimated parameters of subordinate arms. Updates the sample average, sample variance, and number of times an arm has been tested.

Clark–Dep–DA: Assumes arms are correlated. Uses ν_1 as an index for each pair of arms based on the estimated parameters of subordinate arms. Uses the DA algorithm to impute the "latent" rewards of the unobserved arms.

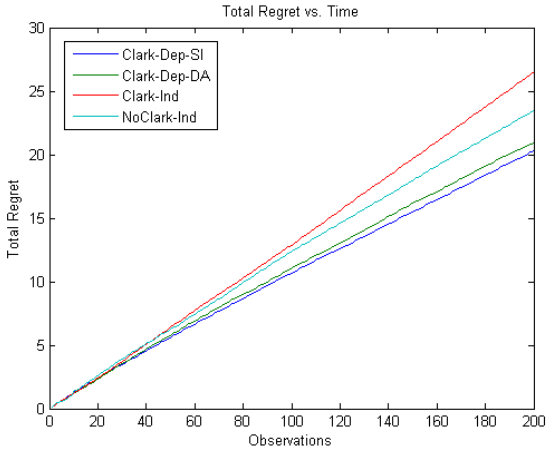

Fig. 1. Total Regret: $T = 200$, $m = 50$, $c = 0.25$.

Clark–Dep–SI: Assumes arms are correlated. Uses ν_1 as an index for each pair of arms based on the estimated parameters of subordinate arms. Uses the SI algorithm to impute the "latent" rewards of the unobserved arms.

We simulated five arms with equal means of zero and a positive-definite covariance matrix exhibiting both positive and negative correlation between arms. This meant that the only differences between pairs of arms came from the variances and correlation of the subordinate arms since Clark's formula reduces to $\nu_1 \propto \sqrt{\sigma_1^2 + \sigma_2^2 - 2\sigma_1\sigma_2\rho}$. We calculated the total regret for each of the policies over a horizon of 200 time steps. When averaged over 25 replications, the ranking of policies in order of increasing total regret is 1) Clark–Dep–SI, 2) Clark–Dep–DA, 3) NoClark–Ind, and 4) Clark–Ind.

V. Discussion

Clark–Ind struggled to discern the optimal pairings of arms since it could not incorporate ρ into its estimate of ν_1. Between the two proposed adaptive policies, Clark–Dep–SI slightly outperformed Clark–Dep–DA and was far less computationally expensive to simulate. An unexpected result was that NoClark–Ind significantly outperformed Clark–Ind. A possible explanation is that NoClark–Ind could eventually rank pairs of arms based on the observed rewards despite incurring slightly more regret than Clark–Ind up to time period 40.

References

[Clark, 1961] Clark, C. E. (1961). The greatest of a finite set of random variables. *Operations Research*, 9(2):145–162.

[Kong et al., 1994] Kong, A., Liu, J. S., and Wong, W. H. (1994). Sequential imputations and bayesian missing data problems. *Journal of the American Statistical Association*, 89(425):278–288.

[Schafer, 2010] Schafer, J. L. (2010). *Analysis of incomplete multivariate data*. CRC press.

[Schafer and Olsen, 1998] Schafer, J. L. and Olsen, M. K. (1998). Multiple imputation for multivariate missing-data problems: A data analyst's perspective. *Multivariate Behavioral Research*, 33(4):545–571.

[Sutton and Barto, 1998] Sutton, R. S. and Barto, A. G. (1998). *Reinforcement learning: An introduction*, volume 1. Cambridge Univ. Press.

[Tanner and Wong, 1987] Tanner, M. A. and Wong, W. H. (1987). The calculation of posterior distributions by data augmentation. *Journal of the American Statistical Association*, 82(398):528–540.

THE CHARACTERIZATION OF A PURE INTEGER PROGRAM THROUGH A LINEAR PROGRAM

Michael Nites, Andrew Shaefer and Oleg Prokopyev
Computational Optimization Laboratory, Department of Industrial Engineering
University of Pittsburgh, PA, USA
Email: mpn10@pitt.edu

INTRODUCTION

Integer programs have many applications in industry, specifically in production planning, scheduling, and telecommunications networks. A pure integer programming problem is an optimization problem where all variables are restricted to be integers. Integer programs are much more difficult to solve than linear programs because of this restriction. It may be possible to better understand the mechanics of an integer program by relating it to a linear program.

Previous literature has focused on expressing the integer programming objective value as a function of its right-hand side. Trapp, Prokopyev and Schaefer (2013) focused on characterizing the function of a pure integer program through its value on the set minimal vectors with respect to their objective function level set. This is applicable because in stochastic integer programming, the level-set approach allows two-stage pure integer programs with stochastic right hand sides to be easily solved. The research presented accounts for this level set approach but explores a different option by characterizing an integer program through a linear program.

METHOD

Consider a standard pure integer programing (IP) problem with n decision variables and m constraints given by

$$\max\left\{\sum_{1\le j\le n} c_j x_j \mid \sum_{1\le j\le n} a_{ij}x_j \le b_i, i \le i \le m\right\} \qquad (1)$$

where x_j is the number of items of item j, c_j is the profit of item j, a_{ij} is some limiting factor i for item j, and b_i is a bound for limiting factor i. We say that $a_j = \left(a_{1j}\ a_{2j}\ \dots a_{mj}\right)^T$ and $b = (b_1\ b_2\ \dots b_m)^T$. The bound $b \in \hat{B}$ and $\hat{B} = \bigotimes_{i=1}^{m} [0, b_i]$. We assume that $0 \le a_j \le b$ and $c_j \ge 0$ for all j. We note that an optimal solution exists.

Now, consider its superadditive dual which is defined in Wolsey (1981). It is given by

$$\begin{aligned} &\min\{F(b)\} && (2a)\\ &F(a_j) \ge c_j, 1 \le j \le n, && (2b)\\ &F \text{ is a superadditive over } \hat{B}, && (2c)\\ &F \text{ is nonincreasing}, && (2d)\\ &F(0) = 0. && (2e)\end{aligned}$$

It is well known that strong duality holds, so that if x^* solves (1) and F^* solves (2), then $cx^* = F^*(b)$.

Consider the following linear program where

$$\begin{aligned} &\min \phi_b && (3a)\\ &\phi_{a_j} \ge c_j, 1 \le j \le n, && (3b)\\ &\phi_{\beta_1+\beta_2} - \phi_{\beta_1} - \phi_{\beta_2} \ge 0, \forall \beta_1, \beta_2, \beta_1 + \beta_2 \in \hat{B}, && (3c)\\ &\phi_{\beta_2} - \phi_{\beta_1} \ge 0, \forall \beta_1, \beta_2 \in \hat{B}, \beta_2 \ge \beta_1, && (3d)\\ &\phi_0 = 0. && (3e)\end{aligned}$$

where $\phi_\beta \in \mathbb{R}_+$ for all $\beta \in B$. It is convenient to note that whenever F is finite, the superadditive dual of the integer program given in (2) is equivalent to the linear program given in (3).

Then, the dual of (3) is given by

$$\pi_j - \sum_{\substack{\beta\in\hat{B}\\ \beta\ge a_j\\ \beta\ne a_j}} \left(\sigma_{a_j,\beta} + \sigma_{\beta,a_j} + \mu_{a_j,\beta}\right) + \sum_{\substack{\beta\in\hat{B}\\ \beta\le a_j\\ \beta\ne a_j}} \left(\sigma_{\beta,a_j-\beta} + \sigma_{a_j-\beta,\beta} + \mu_{\beta,a_j}\right) \le 0, \qquad (4a)$$

$$j = 1, \dots, n$$

$$\sum_{\substack{\beta\in\hat{B}\\ \beta\ge a_j\\ \beta\ne a_j}} \left(\sigma_{\bar{\beta},\beta} + \sigma_{\beta,\bar{\beta}} + \mu_{\bar{\beta},\beta}\right) + \sum_{\substack{\beta\in\hat{B}\\ \beta\le a_j\\ \beta\ne a_j}} \left(\sigma_{\beta,\bar{\beta}-\beta} + \sigma_{\bar{\beta}-\beta,\beta} + \mu_{\beta,\bar{\beta}}\right) \qquad (4b)$$

$$\le 0, \forall \beta \in \hat{B}, \beta \ne a_j, b, 0,$$

$$\sum_{\substack{\beta\in\hat{B}\\ \beta\geq a_j\\ \beta\neq a_j}}(\sigma_{b,\beta}+\sigma_{\beta,b}+\mu_{b,\beta})+\sum_{\substack{\beta\in\hat{B}\\ \beta\leq a_j\\ \beta\neq a_j}}(\sigma_{\beta,b-\beta}+\sigma_{b-\beta,\beta}+\mu_{\beta,b})\leq 1, \tag{4c}$$

$$\sum_{\substack{\beta\in\hat{B}\\ \beta\geq a_j\\ \beta\neq a_j}}(\sigma_{0,\beta}+\sigma_{\beta,0}+\mu_{0,\beta})+\sum_{\substack{\beta\in\hat{B}\\ \beta\leq a_j\\ \beta\neq a_j}}(2\sigma_{\beta,\beta}+\mu_{\beta,0})\leq 0, \tag{4d}$$

$$\pi_j\geq 0,\forall j=1,\dots,n, \tag{4e}$$

$$\sigma_{\beta_1,\beta_2}\geq 0,\forall\beta_1,\beta_2\in\hat{B}, \tag{4f}$$

$$\mu_{\beta_1,\beta_2}\geq 0,\forall\beta_1,\beta_2\in\hat{B}, \tag{4g}$$

$$\lambda\geq 0. \tag{4h}$$

In this case, it is also well known that strong duality holds. Given the transformation from (1) to (4), it is possible to characterize the integer program in terms of the linear program if a solution to (4) can be found. This is because (1) and (2) have the same solution via superadditive duality, (2) and (3) are the same problem though structured differently, and (3) and (4) have the same solution via linear programming strong duality.

Given a solution $\hat{x}$ to (1), it is proposed that if (x^*,σ^*,μ^*) is defined as

1. $\pi_j^*=x_j^*$ for all j
2. $\sigma_{a_j,b}^*=x_j^*$
3. $\sigma_{a_j,\beta}^*=0$ for all $\beta\neq b$
4. $\sigma_{\beta,\beta'}^*=0$ if $\beta\neq a_j$ or $\beta'\neq b$
5. $\sigma_{b,0}^*=1$
6. $\mu_{\beta_1,\beta_2}^*=0$ for all β_1,β_2,

then (x^*,σ^*,μ^*) is an optimal solution to (4). Though a formal proof has been omitted, proving that the proposed optimal solution is true first entailed plugging in the solution into (3b-e) and (4b-h) to check for primal and dual feasibility. This was achieved since each statement remained true after plugging in the proposed solution. Since the proposed solution was both primal and dual feasible, it was proven that the solution is optimal by proving each condition to hold true under the conditions of complementary slackness for a linear program. Complementary slackness is important because

DISCUSSION

Although we have proposed an optimal solution to (4), it is highly degenerate. This means that for an integer program that has relatively few constraints, the equivalent linear program is many times larger with many of the variables equal to zero. For example, the constraint given in (3c) represents a constraint for every combination of β_1 and β_2 that sums to value still in $\hat{B}$. Thus, degenerate linear problems are much more difficult to solve and therefore this particular dual may not be the most computationally efficient.

FUTURE WORK

Because the degeneracy of the solution to (4) makes it more difficult to solve, it may not have a direct application that can be successfully used. It is largely theoretical in nature and lays the foundation by providing an example of the characterization of an integer program through a linear program in lesser-understood field. Future work that attempts to build off of this work should emphasize finding another possible dual to (3). By finding something that is much smaller in nature and more comparable in size to (1), it may be possible to apply it to many different circumstances.

REFERENCES

1. Trapp AC, Prokopyev OA, Schaefer AJ (2013) On a Level-Set Characterization of the Value Function of an Integer Program and Its Application to Stochastic Programming. *Operations Research*. 61(2):498-511.
2. Nemhauser GL, Wolsey LA (1988) *Integer and Combinatorial Optimization* (John Wiley & Sons, Inc., New York).

IMPINGING JET EFFECTS OF TURBULENT FLOWS

ALEX VALENTINO, TYLER LANDFRIEND, DR. MARK KIMBER
Swanson School of Engineering, University of Pittsburgh, PA, USA
Email: AValentino917@gmail.com

INTRODUCTION

Turbulent jets are common in various industrial and engineering applications, based on the surroundings of the jet hydrodynamics, jets are classified as either free or confined jets. It's been debated that significant differences exist between confined jets and free jets. In most practical applications we are dealing with jets confined by walls and other objects which in turn results in behaviors that are different from the well-known behaviors of a free jet. [1]

There has been a large interest in the behavior of confined jet flow with the new designs of the Generation IV Very High Temperature Reactor (VHTR). One of the main issues that needs to be addressed related to the flow hydrodynamics of the VHTR is the issue of turbulent mixing of coolant jets exiting from the reactor core into the lower plenum. [1]

HOT WIRE ANEMOMETRY

To measure the mean and fluctuating velocities in fluid flows we used a Hot-Wire Anemometer from Dantec Dynamics. The specific anemometer we used was a Tri-Axial Constant Temperature Anemometer. This type of CTA is used in 3D flows and can give us the mean and fluctuating velocities in the U,V and W directions. The probe is extremely sensitive due to its 5 micrometer diameter wires which detect the change in flow velocity and outputs a voltage in which we can turn into a velocity when the probe is properly calibrated.

In order to calibrate, the Dantec Three Wire Probe is initially placed inside a wind tunnel with the probe stem parallel to the flow of the tunnel. Then each probe wire reads a voltage from 12 wind tunnel frequencies and the velocities can then be calculated from Kings Law (1). [2]

$$U_{eff} = \frac{(E-c)^{\frac{2}{b}}}{a}$$

Coefficients a,b and c are determined from a Power Law fit of the expected velocity of the wind tunnel via a pitot tube and the voltage read from the probe. U_{eff} is the effective cooling velocity acting on the three sensors. In order to transform the coordinate system to the velocity acting on the three sensors to the velocity of the flow in respect to the jet in our set up, we use Dantec's manufactured yaw k^2 and pitch h^2 factors of 0.02 and 1.05 repectively. Using various transform matrices given by fundamental anemometry theory we are able to calibrate the probe the read out velocities with respect to the jets orientation.

TEST SET-UP

The tests occur in a tightly sealed plexi-glass box. The box is 48"x36"x36", inside the box are stages that move in three directions (X,Y,Z). Attached to the stages is the three wire probe and the stages are controlled by the computer using Matlab and a stepper motor. At the top of the box setup there is a 0.875" in diameter jet which can blow air up to a Reynolds Number of ~50,000. Then a plate is inserted underneath the jet inside the box which acts as the impinging source. [3]

RESULTS

After running multiple tests of different Reynolds numbers and plate heights we were able to map out the velocity contour for the entire test set up. Figure (1) shows us the velocity contour of a test with the impinging plate 8 jet diameters away from the jet at a Reynolds number of 2e4.

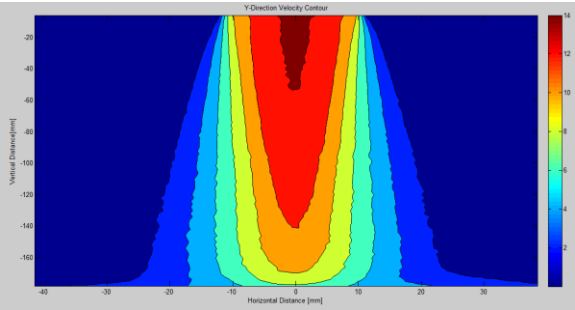

Figure 1: Velocity Contour of Impinging Test at Reynolds Number of 20000

The Y axis represents the vertical displacement of the set-up with 0 being the outlet of the jet. The X axis represents the horizontal distance of the XY plane with the 0 point being the centerline. The gradient represents the magnitude of velocity in [m/s]. As the probe gets closer to the plate the velocity decreases until the velocity hits 0 m/s at the plate.

We also determined the turbulence kinetic energy (TKE) of the system. The TKE is the mean kinetic energy per unit mass associated with the eddies in turbulent flow. In the Reynolds-averaged Navier Stokes equations, the TKE can be quantified by the mean of the turbulence normal stresses; Equation (2). [4]

$$k = \frac{1}{2}\left(\overline{(u_1')^2} + \overline{(u_2')^2} + \overline{(u_3')^2}\right)$$

Figure 2 show the Turbulent Kinetic Energy of 4 tests with plate heights at 4 spacings.

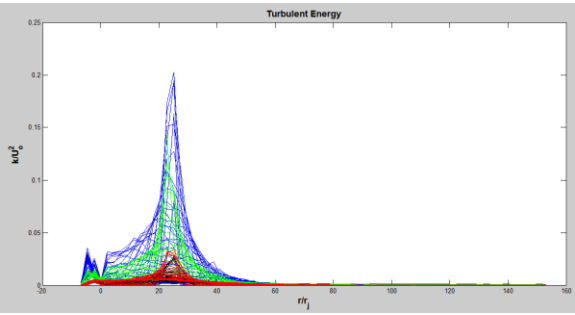

Figure 2: Turbulent Kinetic Energy of all the Plate heights at a Reynolds Number of 20000

The plot is normalized with respect to the maximum velocity for each row. The lines closer to 0 on the Y axis are the points closer to the jet inlet. The Turbulent Energy peaks at 20 mm in the radial direction. This peak occurs at the edge of the get because that is the point where the greatest eddies are occurring.

FUTURE WORK

The final part of this test is to analyze the second and third moments that are resulted from impinging flow. We are currently in the post-processing stage of this part and we are planning on having results with in the end of the next month. Once we have the moment results, I will be assisting in publishing a paper about the impinging jet results for the International Journal of Heat and Mass Transfer.

After this paper is written the next step will be to start on non-isothermal testing. For this type of testing a new containment box will need to be constructed. The goal is also to completely automate the system to improve accuracy as well as consistency of the results.

REFERENCES

[1] Mazumdar, Sagnik, Tyler Landfried, Anirban Jana, and Mark Kimber. "Computational Study of Confined Isothermal Turbulent Round Jets." *NURETH Conference*. n. page. Print.

[2] Jorgenson, Finn E. . "How to Measure Turbulence with Hot-Wire Anemometers." *Dantec Dynamics*. n. page. Print.

[3] Hussein, Hussein J, Steven P Capp, and William K George. "Velocity Measurements in a High-Reynolds-Number Momentum-Conserving, axlsymmetric, Turbulent Jet." n. page. Print.

[4] Pope, S. B., (2003) 'Turbulent Flows', Cambridge: Cambridge University Press

ACKNOWLEDGEMENTS

I would like to thank Dr. Mark Kimber as well as Graduate Student Tyler Landfried for allowing me to work with them this summer and gain excellent Mechanical and Nuclear engineering experience

MOTION OF A RIGID BODY WITH A CAVITY FILLED WITH VISCOUS FLUID

Jeremy Murphy

Swanson School of Engineering, Department of Mechanical Engineering and Materials Science

University of Pittsburgh, PA, USA

Email: jwm60@pitt.edu, Web: http://www.engineering.pitt.edu/mems/

INTRODUCTION

Proper characterization of the motion of a rigid body with a cavity filled with viscous fluid is a problem which challenges both mathematicians and engineers due to the complex physical phenomena at work. The purpose of this project is to supplement the extensive mathematical and numerical work done by Dr. Galdi, Dr. Zunino, and their team of PhD and graduate students at the University of Pittsburgh by designing an experiment and visual aids that illustrate the predicted behavior of the system, as well as to familiarize the author with the methods used in obtaining their results.

The results of this work that are of particular interest to this project pertain to the rotation of a rigid body which has two principal moments of inertia that are the same and one that differs (as in a cylinder), and contains a cavity completely filled with Newtonian viscous fluid. Among many important results, Dr. Galdi and Dr. Zunino found in their numerical study that if the body is arranged such that its principal axes do not initially line up with its rotational axes, that given enough rotational time these axes will coincide[1].

METHODS

In order to visualize the results of the numerical simulation, a Matlab script was written by Dr. Zunino which took the angular velocity data produced by the simulation and transformed it into a series of time-discretized angular displacements. This collection of displacements was transformed using linear algebra into a rotation matrix that would rotate points in 3D Euclidean space about the origin of this space. Since the velocity data was taken with reference to the frame attached to and rotating with the body, it was transformed using a special function to be viewed from a stationary inertial frame. This rotation matrix was then applied to points representing the vertices of a cube centered on the origin of its 3D space at each time interval and the graphics recorded. The end result was a short movie showing the rotation of the cube as dictated by the numerical data.

This result proved to be informative and appropriate, however it needed to be optimized in aesthetics and generality. To accomplish this, the cube of the original code was replaced with vectors corresponding to the reference frame attached to the body. These vectors were rotated using the same matrix used on the cube, and were labelled along with vectors representing the initial angular velocity and the angular velocity at the current time.

To bring the results of the theoretical predictions into a practical sense, an experiment was designed to mimic the particular case mentioned in the introduction. In order to study pure rotation, a device similar to a gyroscope was developed. The first prototype encompassed a rigid body made from PVC pipe in the shape of a cylinder, in which were drilled holes to fill the body with fluid. This body had multiple

holes drilled at different angles with its vertical principal axis to allow for rotational and principal inertial axis separation.

The body was mounted within an inner square ring made of wood via axles with ball bearings, and sized such that it contained a volume of approximately 1.5L of water. This inner ring was similarly mounted in an outer square ring, and the outer ring between two wooden supports which were fixed to a table edge via C-clamps. The rings and body were mounted such that each allowed a rotation about an axis perpendicular to the other two, resulting in free 3D rotation.

Elimination of friction was of extreme importance to consider only the effects of the fluid on the rigid body, so mounted deep-groove ball bearings were used.

The body was then set into rotation about its axis using a gear motor with a known rotational speed, and about the other axis by applying a force to the surrounding rings. The motion of the body was recorded using a stationary camera and viewed to study the behavior of the body.

RESULTS

The modified Matlab code proved to be more aesthetically pleasing by reducing the delay between frames of the recorded video due to simplifying the visuals. The visualization was also generalized by displaying a reference frame that could be attached to any body, regardless of shape and size.

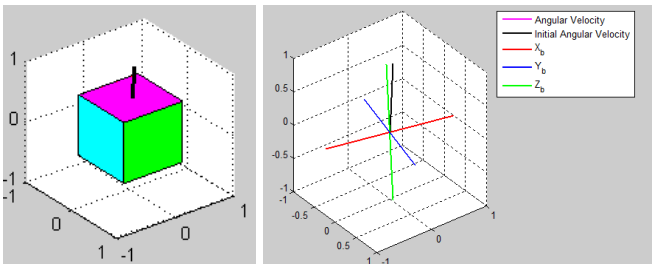

Figure 1: Original result of Matlab code (left) vs. new result (right).

The video from the first prototype of the experimental device indicated that it would indeed serve its intended purpose to facilitate rotation of the body with fluid inside. The rotation, however, was far too slow as a result of friction in the bearings. The device was also found to be imbalanced and favored a particular arrangement due to gravity.

DISCUSSION

The new result of the code will be useful in taking complicated and extensive data and displaying it in a simple, informative manner. It can particularly be used to present results to non-experts with an interest in the topic and serve as the foundation for research of applications of the results of this study.

The friction in the first prototype was a result of multiple factors. The small size of the bearings requires extremely precise sizing and machining of the shafts to maintain their effectiveness. Excessive misalignment of the shafts also contributed, due to slightly slanted holes in the wooden frame and slightly inconsistent positioning of the bearing mounts.

The imbalance of the device could be fixed temporarily with counter weights, but the more proper solution will be to use precise alignment techniques. This project will be ongoing into the fall semester which will culminate in a final experiment design based on the prototype that will be used to properly test the results of Dr. Galdi, et. al.

REFERENCES

[1] Galdi, Paolo and Paolo Zunino. *On the motion of a rigid body with a cavity containing a Newtonian fluid – A numerical study*. University of Pittsburgh. August 14, 2012.

CALCIUM CHANNELS IN SYNAPTIC STRUCTURE

Sarah Higbee, Markus Dittrich and Stephan D. Meriney
Pittsburgh Supercomputing Center
University of Pittsburgh & Carnegie Mellon University
Email: seh97@pitt.edu

INTRODUCTION

There are many unknowns when it comes to the functioning of synapses. The small size of synaptic vesicles, calcium channels, and their components makes direct study difficult, so computer simulations are valuable for testing possible models of their workings.

This project studied a model of a single active zone enclosed by a membrane, with two parallel rows of vesicles outside of two rows of channels, as in a frog. The rows are equidistant from the midline between them. In this model, vesicles have twenty pairs of calcium sensors on their undersides, and release their payload of neurotransmitters when three pairs (six sensors total) are simultaneously bound to ca2+ [1]. The vesicles also have 144 ca-binding "Y" sensors surrounding the ca sensors in a ring, whose function isn't important to the data reported here outside of their minor impact on the free calcium population.

In order to view the behavior of the model, two versions of a simulation were run, one varying the number of calcium channels and the other varying their placement. The ratio of fusions from the first action potential to fusions from the second (the pulse ratio) should increase, then decrease, as the number of channels increases [2]. The effect of channel distance on pulse ratio should be similar.

METHODS

The model was constructed at the molecular level using the software Mcell version 3.1, and run on Salk, an SGI Altix 4700 shared-memory NUMA system with 144 Itanium2 processors. Varying probabilities of ca release simulated the action potential; two action potentials occurred during the 13 ms-long simulation. In the simulations that varied the number of channels, the distance of the channels remained constant at 0.0358 nm from the midline. The desired number of the fixed-position channels was removed randomly for each test. In those that varied the channel distance, the number of channels was fixed at 26. All channels were equally distant from the midline. In both cases, the buffer filling the synapse was stationary.

DATA PROCESSING

The program output displayed the times at which each sensor on each vesicle was bound to a calcium ion. These were counted after the fact. A vesicle with sufficient bound sensors was assumed to have fused, and to have remained fused for the rest of the simulation.

Results were averaged over 100 trials.

RESULTS

As expected, vesicle fusion increases with increased channel saturation, with the second pulse releasing slightly fewer than the first. Both of these conditions are true of the position-varying runs as well (graph not shown).

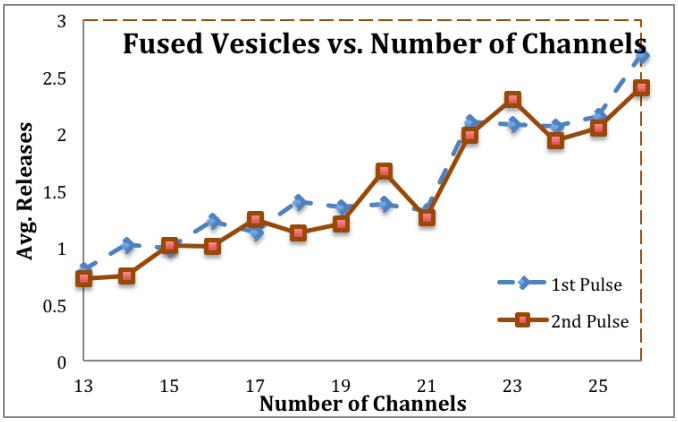

Fig. 1: Shows the average number of vesicles fused during a single action potential, for a range of thirteen to twenty six channels. The red line with blue points is the response to the first action potential, and the blue line with red points is that of the second.

In fig. 2 below, pulse facilitation seems to increase slightly, then slightly decrease as number of channels increases.

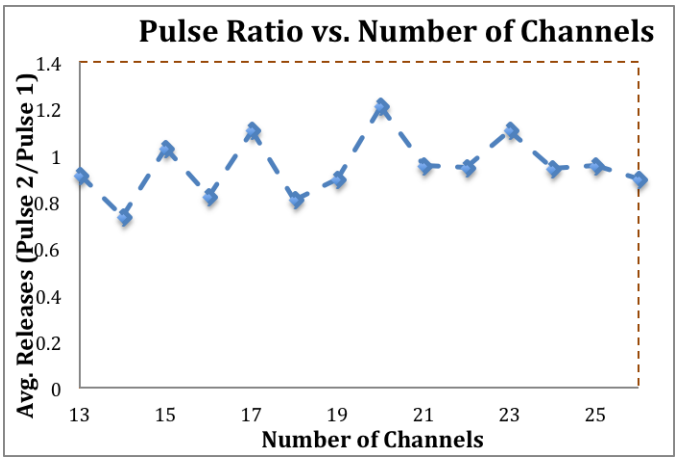

Fig 2: The ratio of the average number of vesicles fused during a first action potential to the average number of vesicles fused during a second action potential shortly after the first.

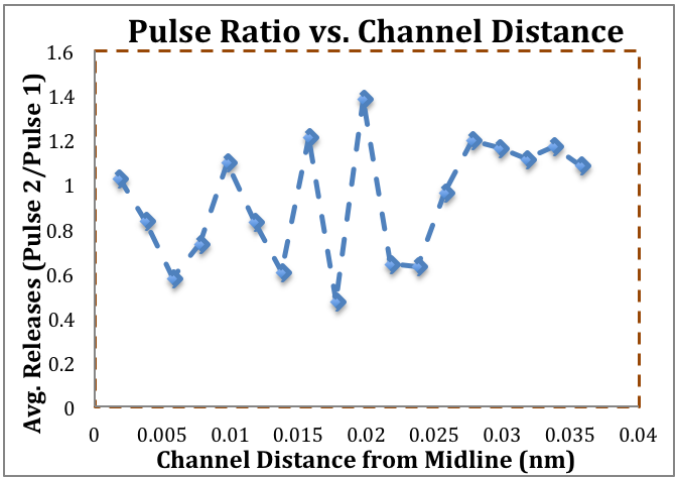

Fig. 3: As Fig. 2, but with channel distance instead of channel number.

Standard deviation bars would have engulfed all graphs, but fig. 3 has the most obviously distorted curve. If nothing else, it suggests that channel distance has but a small effect on vesicle release.

DISCUSSION

This data doesn't seem inconsistent with expectations, but doesn't strongly support it yet. The error is too high. Still, these results show interesting, suggestive curves, and if developed a bit more could provide a good basis for comparison of this model with others.

With more collected trials to average, the uneven data curves could be smoothed out. In addition, a wider range of quantities of channels would clarify the shape of the curve in fig. 2.

REFERENCES

1. Dittrich et al. (2013). An Excess Calcium Binding Site Model Predicts Neurotransmitter Release at the Neuromuscular Junction. *Unpublished manuscript*
2. *Personal communication.*

IN VIVO THREE DIMENSIONAL KINEMATICS OF THE KNEE DURING DOWNHILL RUNNING

Greta Brecheisen, Eric Thorhauer and Scott Tashman
Orthopaedic Biodynamics Laboratory, Department of Orthopaedics
University of Pittsburgh, PA, USA
Email: grb35@pitt.edu

INTRODUCTION

The anterior cruciate ligament (ACL) attaches from the lateral femoral condyle to the anterior tibial plateau. This ligament is essential to knee stability as it prevents anterior shifts of the tibia, excessive tibial internal rotation, and hyper extension of the knee [1].

Approximately 200,000 ACL injuries occur annually in the US and around half will undergo an elective surgery to repair the damage [2]. ACL reconstruction is often performed to improve stability and future joint health as patients with an ACL deficiency exhibit a higher prevalence for osteoarthritis (OA) versus the uninjured population [6].

Osteoarthritis is an important consideration for those who undergo ACL reconstructions. OA is a progressive degenerative joint tissue disease [8]. Radiographic evidence of OA has been found in 13-65% of patients 3-12 years after ACL reconstruction [2]. Ultimately, reconstructions that mimic the natural knee environment will minimize the risk of developing OA. There are multiple surgical methods in use for ACL reconstructions, but long term ramifications of each procedure remain largely unknown [2].

This study examined the kinematics of both the affected knee (after ACL reconstruction) and control knee (contralateral limb) in an attempt to better characterize in vivo knee kinematics post-ACL reconstruction.

METHODS

A total of 41 subjects (15 female, 26 male) were analyzed for this study. The ACL reconstructions utilized quadriceps tendon grafts placed anatomically**.** Patients were randomly assigned a single bundle (SB) or double bundle (DB) reconstruction (20 SB, 21 DB). Due to the ongoing nature of this clinical trial and the need to maintain blinding, the two groups were combined for this preliminary analysis.

All subjects performed downhill running on a treadmill at 3.0 m/s (10 degree decline). Data was recorded from shortly before foot strike to mid stance for both limbs. A dynamic stereo X-ray system captured the motion at 150 frames/sec [5].

The subjects were tested post-surgery once their rehabilitation regimes had been completed and a return to light physical activity had been approved by a physician. Time between the reconstruction and testing ranged from 4-10 months, with an average duration of 6.5 months.

CT scanning was used to develop subject-specific 3D models of the femur and tibia for both knees using the program Mimics (Materialise, Leuven Belgium).

DATA PROCESSING

The 3D model of each bone created from the CT scan was aligned to the collected x-rays using a model based tracking system proven to have an accuracy of ±0.2 mm [4]. This alignment allowed for the assessment of the three-dimensional movements of the knee joint and a kinematics analysis of the knee. Heelstrike was set as time zero for all evaluations.

The following rotations and translations of the tibia relative to the femur using body-fixed axes were examined: flexion/extension, abduction/adduction, internal/external rotation, anterior-posterior (AP) translation, and lateral-medial (LM) translation [2]. Both AP and LM translation evaluated the relative movement of the tibia. Hence, at heelstrike, translation was set to zero millimeters for both of these movements.

Differences in six degree of freedom kinematics were assessed with a 2-way repeated measures ANOVA test (SPSS v20 software)(α = 0.05). When significant differences were found, post-hoc paired t-tests were performed to identify differences at specific time points.

RESULTS

There was no significant difference between the control and affected sides for either AP translation (α=0.128) or LM translation (α=0.460).

The limbs did, however, display a significant difference in flexion angle ($\alpha < 0.001$) as the reconstructed knee was more extended post-heelstrike. In addition, abduction/adduction and internal/external rotations also experienced significant differences between limbs (α<0.001, and α=0.004 respectively). The affected side was more adducted and externally rotated in comparison to the control knee. Figure 1A displays the flexion of the affected knee and contralateral side, Figure 1B abduction/adduction and Figure 1C internal/external rotation.

DISCUSSION

The results of this preliminary analysis suggest that the anatomical reconstruction techniques utilized for this study may not fully restore normal knee kinematics. Results were generally similar to previous research that identified greater adduction and external rotation in the reconstructed limbs [2].

Any change in knee kinematics is important to consider when evaluating the effectiveness of anatomical ACL reconstructions. Excessive internal tibial rotations have been shown to speed cartilage thinning and thus quicken the onset of OA [6]. The use of an anatomical ACL placement did not eliminate these motions. In regards to flexion, the primary motion of the knee, the clinical significance of the significant discrepancy between sides is uncertain, but of some concern. Any change in cartilage loading might accelerate thinning and quicken the onset of OA [7].

One possible cause for the difference in flexion angle between the affected and contralateral side is weakness of the quadriceps muscles. Lewek found that weaker muscles post-ACL reconstruction resulted in decreased flexion angles at peak flexion [3]. This trend is clearly displayed in Figure 1A. As the subjects were an average of 6.5 months post operation and still recovering, muscle weakness of the injured leg is highly probable. This suggests that further improvements in rehabilitation strategy may be needed to improve short-term kinematics. Longer (2-year) follow-up with thorough outcomes and imaging is planned for these subjects, which should provide greater insight into the significance of the study findings. Future analyses will also investigate whether double-bundle reconstructions lead to better restoration of normal kinematics than more traditional single-bundle methods.

Ultimately, while positive steps have been made, further research is necessary to assess and optimize surgical methods for ACL reconstructions. Only through additional research and innovation can the best protocols for reconstruction and rehabilitation be developed.

REFERENCES

[1] National Academy of Sports Medicine. www.nasm.org

[2] American Academy of Orthopaedic Surgeons. *Anterior Cruciate Ligament Injury: Surgical Considerations.* July 2007.

[3] Lewek et al. *The effect of insufficient quadriceps strength on gait after anterior cruciate ligament reconstruction.* Clinical Biomechanics. Vol 17. 2002.

[4] Anderst W et al. Med Eng Phys, Jan;31(1):10-6, 2009.

[5] Tashman S. et al. Dynamic function of the ACL-reconstructed knee during running. Clin Orthop Relat Res. 2007 Jan;454:66-73.

[6] Andriacchi T.P. et al. *Rotational Changes at the Knee after ACL Injury Cause Cartilage Thinning.* Clinical Orthopaedics and Related Research. Vol 442. 2006.

[7] Georgoulis A.D. *ACL injury and reconstruction: Clinical related in vivo biomechanics.*Orthopaedics and Traumatology. 2010.

[8] Hunter D. *Osteoarthritis.* Best Practice & Research Clinical Rheumatology. Vol 25, Issue 6, December 2011. 801-814.

ACKNOWLEDGEMENTS

This study received funding from NIH grant 5R01AR056630-02. It was administered by the National Institute of Arthritis and Musculoskeletal and Skin Diseases.

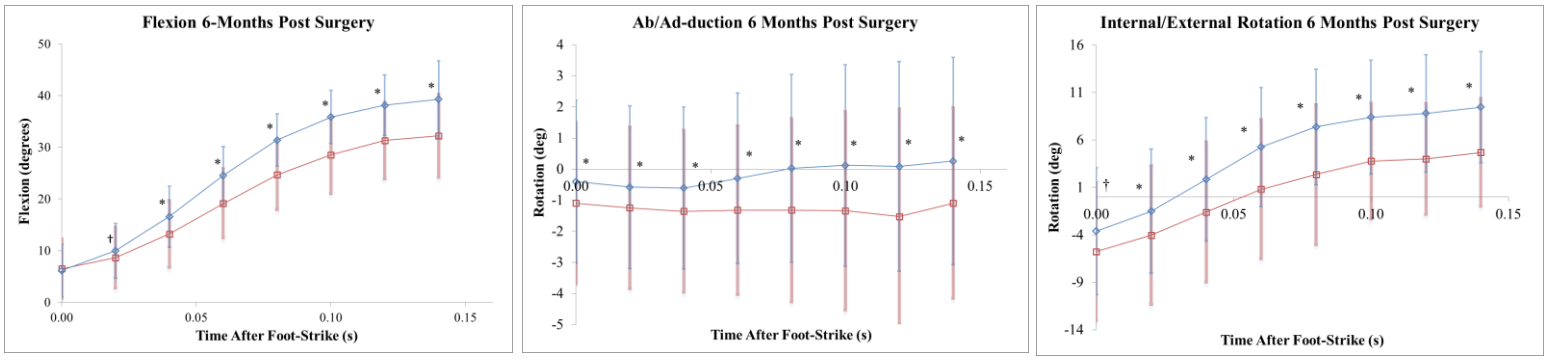

(A) (B) (C)

Figure 1: Affected (red squares) and control (blue diamonds) knees from heelstrike. Statistical significance (α<0.05) is denoted with an asterisk and marginal significance (α<0.10) with a cross. Figure 1A depicts degrees flexion, Figure 1B displays abduction and adduction of the tibia, and Figure 1C shows degrees of internal and external rotation.

PRL-3 mediates colony formation of mouse tumor cells *in vitro*

Timothy N. Thompson, Julie M. Chandler
Lagasse Laboratory, McGowan Institute of Regenerative Medicine
University of Pittsburgh, PA, USA
Email: tnt15@pitt.edu , Web: http://www.mirm.pitt.edu/lagasse/

Introduction

The metastasis of cancer tumors is responsible for the majority of deaths caused by cancer. During metastasis cells undergo changes such as declined adhesion and enhanced motility as well as degradation of the basal membrane [1]. This allows tumor tissue to relocate to sites throughout the body and spread the cancer making surgery difficult or impossible

PRL-3 is overexpressed in the majority of metastatic tumors. Saurabh et al. showed alteration in PRL-3 due to gene amplification in patients with metastatic disease [2]. In addition, Zeng et al. examined the effect of PRL-3 expression in nonmetastatic ovary cells on invasiveness and motility. The phosphatase activity of PRL-3 was required for optimal cell migration. Cells with wild-type active PRL-3 greatly increased motility whereas catalytically inactive PRL-3 mutants did not [3]. Wang et al. examined the role of PRL-3 in epithelial-mesenchymal transition (EMT), an important component of tumor metastases. They found that PRL-3 caused possible activation of PI3K-Akt, leading to down-regulation of adhesion proteins such as E-cadherin, γ-catenin, and integrin β_3 leading to EMT [4]. The purpose of this project is to further examine the phosphatase of regenerating liver-3 (PRL-3) gene's role in metastatic growth of tumor cells by qualitatively and quantitatively observing tumor colony formation *in vitro*.

Methods

Wild type (WT) mouse colon cancer cells and PRL-3 knockout (KO) mouse colon cancer cells were plated on LA7 rat mammary stroma cells in separate 25 cm^2 culture flasks (Corning Inc.). This co-culture system has previously been used to expand human colon cancer cells derived from human metastatic colon cancer [5]. The cells were previously collected from mice where colon tumors were induced using an AOM-DSS model. WT and KO Mice were injected once with 12.5mg/kg of Azoxymethane (AOM) to initiate tumors followed by 3 rounds of 2.5% Dextran Sodium Sulphate (DSS) in the drinking water to drive tumor progression.

WT and PRL-3 KO cells were grown separately in culture flasks until they reached a confluency of about 70%. The cells were collected and counted using a hemocytometer (Bright Line®). 1.2 million cells were plated on a 24 well-plate (Corning Inc.). The cells were plated evenly on 16 of the 24 wells of each plate to serve as control and triplicate wells for each of four time points.

The day after plating (day 1) four wells of each plate were collected for flow cytometry analysis to count the baseline number of cells in each well. Each well was collected in separate flow tubes. The tube corresponding to well one of each group was split between two tubes. WT and KO tube 1 received only a Sytox Blue (InVitrogen™) live/dead stain. Tube 2, 3, 4 and 5 received Sytox Blue and EpCAM-APC-Cy7 (Bio Legend®) stains. Negative and EpCAM-APC-Cy7 compensations tubes were prepared with flow beads (BioScience). Cells/beads in each tube were suspended in 400µL of flow buffer. The Flow Cytometer (Miltenyi MACSquant®) was calibrated and the voltages were set using the single stained compensation tubes and WT and KO tube 1 were used for Sytox Blue compensation. The samples were run through the flow cytometer, 225µL of KO and WT tube 1 and 325µL of KO and WT tubes 2, 3, 4, and 5. A defined volume allowed us to quantitatively measure the number of EpCAM+ cells. This procedure was repeated on days 4, 8, and 11

Data Processing

The cell counts obtained from the flow cytometer were analyzed using FlowJo software (Tree Star©). The populations were first gated to include live (Sytox Blue-) and single cells. Subsequently, the number of EpCAM+ cells were counted and recorded at days 1, 4, 8, and 11 and placed into a graph in Excel to compare the growth between the WT and KO groups. Pictures were also taken twice a week as the colonies grew in the 25 cm^2 flasks to give qualitative results. A t-test was used to find the

significance in the difference between WT and KO growth at each day.

Results

Data obtained shows decreased growth in the PRL-3 KO group compared to the WT Group. Visual observation of the 25 cm^2 flasks also shows less colony formation in the PRL-3 KO cells. Figure 1 shows a comparison between the WT and KO growth over several days. WT cultures show more colony formation compared to the KO cells.

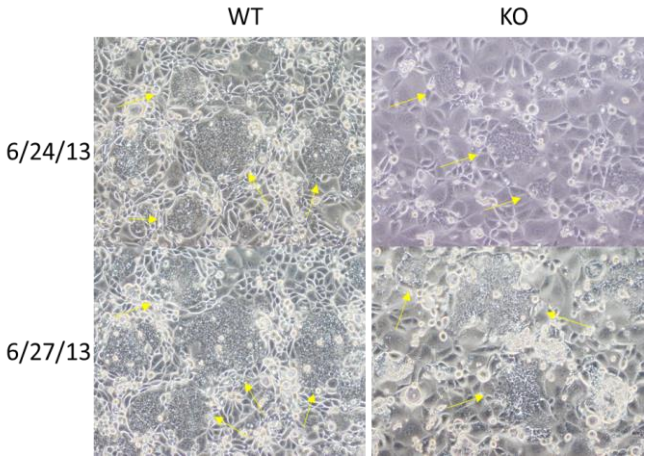

Figure 1: Wild type and knock-out cells. Growth patterns shown over a period of 3 days.

Figure 2 shows the EpCAM positive (mouse tumor cells) and negative (rat feeder layer) populations and a decrease in the percent of EpCAM positive cells present over the course of 11 days as well as a lower percent in the PRL-3 KO group compared to the WT group. Table 1 shows the average number of EpCAM+ cells present in the KO and WT groups at each day and their respective standard deviations. Figure 3 graphically displays the growth curves of WT and KO cells using total EpCAM+ cells at each day.

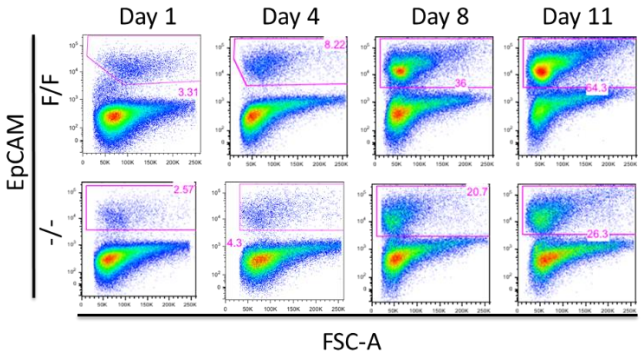

Figure 2: The flow cytometry output of the population of live and single EpCAM+ and EpCAM- cells. The percent of EpCAM+ cells is greater for the WT over the KO at each day.

Table 1: The average number of EpCAM+ cells were calculated from triplicate wells/tubes at each day.

Day	MsTu KoA	StDev	MsTu WtA	StDev
1	4279	111	11697	782
4	5679	187	21660	1790
8	8532	1930	59142	3614
11	22169	1332	82971	9729

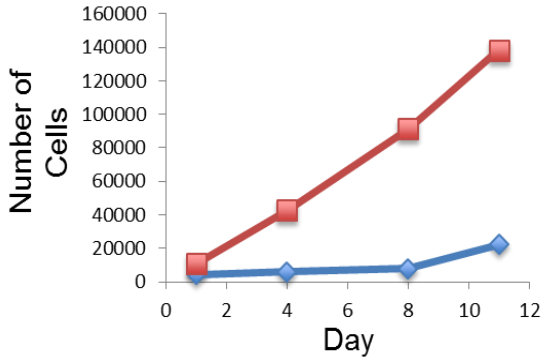

Figure 3: Growth of the WT tumor cells (red) compared to the growth of the KO tumor cells (blue). By day 11 there were approximately 6 times as many WT cells as KO cells.

Discussion

The data collected is consistent with findings in current literature that the overexpression of PRL-3 in tumors plays a key role in the metastasis of tumor cells to foreign areas of the body. The decreased number of cells seen over the course of 11 days in the PRL-3 KO group can be attributed to the decrease in colony formation seen in the pictures. A higher colony formation in the WT may be evidence of the metastatic characteristic of increased motility and invasiveness observed by Zeng et al in ovarian cells as well as activation of the EMT pathway through PI3K-Akt activation as hypothesized by Wang et al. [2, 4]

To further investigate the significance of PRL-3 in metastasis future studies will use a PRL-3 inhibitor on WT cells to examine if a similar growth pattern is observed between KO and inhibitor treated WT cells. This would not only confirm that the results of the PRL-3 KO are specific but that PRL-3 may be a suitable target for advanced cancer therapies.

References

1. D. Hanahan et al, *Cell* **100**, 57–70, 2000
2. Saurabh et al. *Science* **294,** 1343-1346, 2001.
3. Zeng et al, *Cancer Res* **63**, 2716-2722, 2003
4. Wang et al, *Cancer Res* **67,** 2922-2926, 2007
5. Odoux et al, *Cancer Res* **68**, 6932–6941, 2008

ESCHERICHIA COLI EXPRESSION, PURIFICATION AND ARTIFIICAL CHAPERONE REFOLDING OF RECOMBINANT SQSTM1/p62 ZZ-DOMAIN PROTEIN FRAGMENTS FOR STRUCTURE/FUNCTION STUDIES

Matthew J. Pincus[a], Patrick R. Bartlow[a], Qin Tong[a], Hye-Yeong Kim[b], Xiang-Qun Xie[a]
[a]Department of Pharmaceutical Sciences, [b]Department of Radiology, University of Pittsburgh, PA, USA
Corresponding authors: a. mjp100@pitt.edu, d. xix15@pitt.edu

INTRODUCTION

Sequestosome 1 (p62/SQSTM1) is a multifunctional adapter protein with roles in selective autophagy, cell signaling pathways, and tumorigenesis [1]. Recent studies suggest that p62 plays a significant role for autophagy in tumor suppression or promotion, liver and lung disease, myopathies, heart diseases, lysosomal storage disorders, and cancers such as multiple myeloma [2]. Ultimately, we aim to develop novel chemical compounds that target p62, specifically inhibitors of its zinc finger (ZZ) domain.

Pre-clinical drug development requires the characterization of the p62 protein-inhibitor interactions by heteronuclear single quantum coherence (HSCQ) nuclear magnetic resonance (NMR) spectroscopy, which will employ p62 protein fragments containing the ZZ-domain. While several published NMR and crystallographic studies examine other domains of p62, none describe the successful expression and purification the proteins containing the p62-ZZ domain. Therefore, the aim of this project was to develop methods for the bacterial expression and purification of p62-ZZ protein fragments for use in pre-clinical HSQC NMR studies. Namely, soluble protein expression in *Escherichia coli* strains was attempted, along with expression as insoluble aggregates (inclusion bodies) followed by artificial chaperone refolding, as described elsewhere [3]. Protein fragments containing the p62(PB1-ZZ-p38) domains and p62(ZZ-p38) domains were selected to allow for the examination of multi-domain interactions during future NMR studies.

METHODS

Expression Vector Selection and Plasmid Construction—With the aim of achieving soluble protein expression, pGEX-2T (GE Healthcare), pET32a (Novagen), and pET21b (Novagen) expression vectors were selected, which feature N-terminal glutathione s-transferase (GST), N-terminal thioredoxin and S-tag, and C-terminal hexahistidine (his6) fusion proteins, respectively. Plasmids were constructed using standard microbiological techniques.

Small-scale Culture Growth—Various strains of chemically competent *E. coli* bacteria were transformed with the plasmid preparations described above by standard microbiological techniques. The transformed cells were used to grow 2 mL starting cultures (LB growth media) and subsequently 5 mL cultures in M9 minimal growth media, as described elsewhere [4,5]. In general, cultures of *E. coli* BL21 (DE3) CodonPlus were grown to OD_{600}=0.6 prior to induction with 0.05-1.0 mM isopropyl β-D-thiogalactoside (IPTG). Cultures were incubated for an additional 4 hours at 37 °C, then overnight at 25 °C. During growth of *E. coli* Arctic Express (DE3) and Arctic Express (DE3) RP (strains genetically engineered to promote soluble expression at lower temperatures), cultures were transferred to a shaker at 12 °C and allowed to equilibrate for 1 hour before induction with 0.05-1.0 mM IPTG at OD_{600}=1.0. Arctic Express cultures were grown for 72 hours after induction.

Expression Screening—After bacterial culture growth was completed, cells were harvested by centrifugation and separated into total protein (complex lysate), soluble protein, and insoluble debris (inclusion body) fractions. Fractionation steps included lysis (by sonication in a standard lysis buffer), resuspension and membrane protein solubilization (using a nonionic detergent-containing buffer), high-salt removal of nucleic acids, and a final wash. Samples were analyzed by sodium dodecyl sulfate polyacrylamide gel electrophoresis (SDS-PAGE). Soluble expression was verified by Western Blot and matrix-assisted laser desorption/ionization (MALDI) mass spectrometry.

Large-Scale Inclusion Body Extraction—Using the growth conditions and fractionation methods described above, 1-L cultures of BL21 (DE3) CodonPlus expressing pET21b-p62(116-192)-his6 and p62(ZZ-p38) constructs were grown and harvested, and the insoluble inclusion material was separated. Inclusion bodies were solubilized and denatured in a buffer containing 8 M urea and 10 mM β-mercaptoethanol.

Purification and Refolding—Solubilized inclusion bodies were purified by immobilized metal affinity chromatography (IMAC) using a GE Healthcare HisTrap HP column under denaturing conditions (6 M urea, ~5 mM β-mercaptoethanol). The eluate was concentrated and added (in three discrete pluses over 3 hours) to an artificial chaperone refolding buffer containing 0.1 M tris-HCl, 1 M arginine, 5 mM GSH, 1 mM GSSG, 20 mM methyl-β-cyclodextrin, and 3 mM cetyl trimethylammonium bromide (pH 8). The refolding solution was allowed to incubate for 72 hours at room temperature. After dialysis into a native (non-denaturing) IMAC buffer, the refolded protein was recaptured by IMAC over a GE Healthcare HisTrap HP column, and the purity of the eluate was assessed by SDS-PAGE.

Confirmation of Biological Activity—For solubly-expressed protein fragment, biological activity was assessed by enzyme-linked immunoabsorbent assay (ELISA) with immobilized IDR-1 peptide, a ligand known to bind to the p62-ZZ domain, and anti-His primary antibody (1° ab). Correct refolding of the insolubly-expressed protein fragment was assessed by measuring binding activity with IDR-1 peptide by surface plasmon resonance (SPR) imaging (BiaCore, GE Healthcare).

RESULTS

The results of the protein expression screenings are presented in Table 1. IPTG induction conditions were varied between 0.05 and 1.0 mM (not listed in Table 1), but ultimately showed no significant effect on protein expression.

Soluble protein expression was achieved only with the pET32a-p62(116-192)-his6 vector (a p62(ZZ-p38) fragment) in Arctic Express (DE3) RP. After scale-up to a 2 L culture and preliminary IMAC purification of the soluble fraction, this protein fragment's binding affinity for IDR-1 ligand was assessed by ELISA, using an anti-His primary antibody, as depicted in Figure 1:

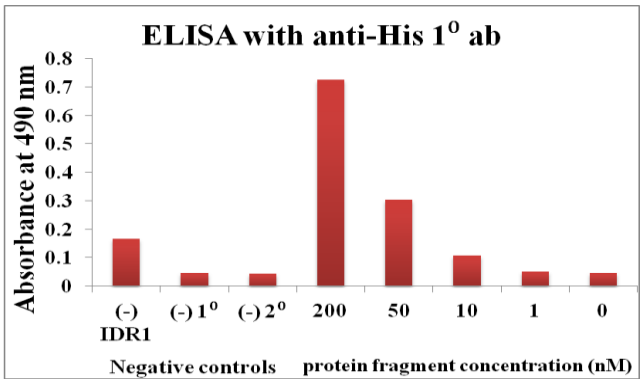

Figure 1: ELISA binding assay for protein concentrations 0-200nM. (-) IDR1, (-)1°, and (-)2° negative controls indicate non-specific binding levels with no IDR1, 1° ab, and 2° ab, respectively

Although insoluble protein expression was achieved several ways, pET21b-p62(22-192)-his6—a p62(ZZ-p38) fragment—in BL21 (DE3) Codon Plus was selected for further development because it does not contain a large GST tag that would inhibit refolding kinetics. The effectiveness of the purification and refolding scheme described above was evaluated after each step by SDS-PAGE. The final refolded p62(ZZ-p38) fragment's binding activity with IDR-1 ligand was assessed by SPR, as depicted in Figure 2:

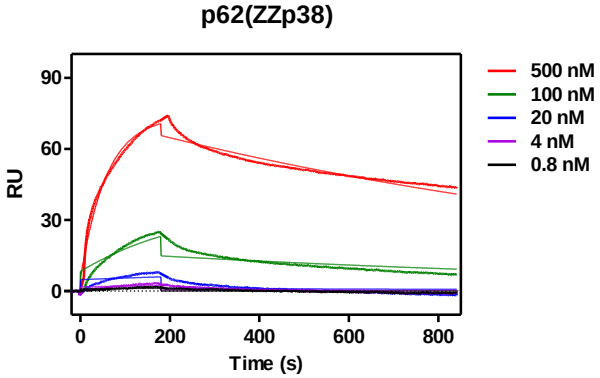

k_a ($M^{-1}s^{-1}$)	k_d (s^{-1})	K_D (M)
2.60×10^4	7.42×10^{-4}	3.12×10^{-8}
$\pm 1.02 \times 10^4$	$\pm 3.80 \times 10^{-5}$	$\pm 1.37 \times 10^{-8}$

Figure 2: SPR sensorgram showing dose-response curves for 0.8-500nM protein and calculated k_a, k_d, and K_D values.

DISCUSSION

The ELISA results for the solubly expressed p62(ZZ-p38) fragment (Figure 1) indicate low levels of nonspecific binding and increasing levels of specific protein-ligand binding at higher protein concentration, which tentatively indicates functional activity of this fragment. It is noted, however, that we have not yet observed saturation binding, so assay optimization is in progress. Pending these results, a procedure for the cleavage of the thioredoxin- and S-tags will be developed, which is made possible by the inclusion of a thrombin cleavage site in the construct design.

Likewise, the dose-response curves of the SPR sensorgram indicate greater binding at higher concentrations of protein. In addition, the calculated k_a, k_d, and K_D values are within the same order of magnitude as those measured for refolded, bacterially expressed full-length p62-his6 (not discussed here). While this suggests correct refolding and functional activity, repeat experiments should be conducted with commercially produced p62 as a positive control.

Altogether, this study represents a major step in the development of a robust protein expression protocol for p62-ZZ domain fragments for structural and functional studies. Future experimental work should aim to doubly confirm the functional activity of the p62(ZZ-p38) fragment by NMR and SPR analysis of the solubly expressed fragment, as well as ELISA of the insolubly expressed, refolded fragment.

REFERENCES

1. Nezis, Ioannis P., and Herald Stenmark. *Antioxid. Redox Signaling*, **17**, 786-793, 2012
2. Yang Z and Klionsky DJ. *Nat Cell Biol*, **12**, 814-822, 2010
3. Schröder-Tittmann, Kathrin. et al. *Biochemistry*, **49**, 7956-7965, 2010.
4. Chowdhury, Ananda et al. *Protein Expres Purif*, **83**, 128-134, 2012
5. Zheng, HaiAn et al. *Biopolymers*, **83**, 46-61, 2006

ACKNOWLEDGEMENTS

The author would like to acknowledge Prof. Xie and his research team members, and Dean Shuman for providing support through the SSOE Summer Research Fellowship. In particular, I would like to thank Patrick Bartlow for his supervision on this project, Qin Tong for plasmid construction and cloning, and Hye-Yeong Kim for SPR data.

Table 1: Protein Expression Screening

Construct and Vector	Bacterial Strain	Growth Condition	Result
pET21b-p62(16-192)-his6	BL21 (DE3) Codon Plus	Standard C+ growth at 37°C	No detectable expression
		~72 hr (post induction) cold-culture growth at 16°C	No detectable expression
	Arctic Express (DE3)	Standard AE growth at 12°C	No detectable expression
pGEX-2T-p62(16-192)	BL21 (DE3) Codon Plus	Standard C+ growth at 37°C	Expression as IBs
	Arctic Express (DE3)	Standard AE growth at 12°C	Expression as IBs
	Arctic Express (DE3) RP	Standard AE growth at 12°C	Expression as IBs
pET21b-p62(23-192)-his6	BL21 (DE3) Codon Plus	Standard C+ growth at 37°C	No detectable expression
pET32a-p62(23-192)-his6	Arctic Express (DE3) RP	Standard AE growth at 12°C	Expression as IBs
pET21b-p62(116-192)-his6	BL21 (DE3) Codon Plus	Standard C+ growth at 37°C	Expression as IBs
	Arctic Express (DE3) RP	Standard AE growth at 12°C	No detectable expression
pET32a-p62(116-192)-his6	Arctic Express (DE3) RP	Standard AE growth at 12°C	Soluble Expression
pGEX-2T-p62(116-192)	Arctic Express (DE3) RP	Standard AE growth at 12°C	No detectable Expression

NOTE: "Standard C+ growth" and "Standard AE growth" refer to the growth conditions described in the Methods for the BL21 (DE3) Codon Plus and Arctic Express (DE3)/Arctic Express (DE3) RP *E. coli* strains, respectively. Expression as "IBs" indicates protein expression as insoluble aggregates (inclusion bodies).

Determining the Threshold of Beneficial Walking in Patients with Knee Osteoarthritis

Paige Kendell
Human Movement Research Laboratory, School of Rehabilitation and Health Sciences, Department of Bioengineering
University of Pittsburgh, PA, USA
Email: pek29@pitt.edu

INTRODUCTION

Knee osteoarthritis (OA) is a condition that affects close to 27 million people in the United States' elderly population [1]. Walking has shown to be an effective therapy for the pain and loss of function that are common symptoms of knee OA. However, too much walking increases the joint forces exerted in the knee. The main focus of this project is to use biomechanical data collected from a patient population along with patient-specific models created in OpenSim to analyze joint contact forces in the knee. The relationship between joint contact forces and rate of disease progression will be analyzed to determine the threshold beyond which too much walking is harmful.

C. Richards and J.S. Higginson analyzed contact forces in patients with varying degrees of knee OA through the use of gait data collected via Motion Analysis [2]. They used OpenSim to derive muscle forces and joint reaction forces to estimate knee contact forces. However, this study did not look at the relationship between the duration of walking and the increase in the knee contact forces.

METHODS

30 patients are involved in this study. Each patient has unilateral knee OA and met criteria set in place by the American College of Rheumatology (ACR) to participate in the study. If a subject qualifies based on the ACR standards, they will be given a definitive grade of OA based on radiographs read by radiologists. In addition to the grading system, each patient must be able to walk for a minimum of 45 minutes at a speed of 1.4 m/sec.

The biomechanical analysis is being done in the Human Movement Research Laboratory (University of Pittsburgh). Prior to data collection, each patient's age, height, weight, heart rate and blood pressure is being recorded. The mechanical data is being collected via Vicon (Oxford Metrics LTD), a video motion capture system. 14 mm spherical reflective markers are placed on predetermined anatomical landmarks on the lower extremities to track motion in the sagittal, frontal, and transverse planes. Calibration markers are also being placed on the subjects which are then removed after capturing a static trial. Throughout the walking trials, kinematic data is being collected at 60 Hz. Ground reaction forces are also being collected at 1200 Hz using a split-belt treadmill (Bertec force plates). During testing, blood is drawn from each subject every 15 minutes and is to be used as a biomarker.

DATA PROCESSING

The motion capture data sets will be processed and filtered using Vicon Nexus software. Each marker will be labeled and accounted for in Vicon. The marker trajectories will be labeled for each patient's static and dynamic trials. Each Vicon model will be cleared of unlabeled trajectories, any outstanding gaps will be filled and Butterworth filters will be run on the data. Each trial will be trimmed to encompass one left and right gait cycle. Next, a C3D file will be exported from Vicon to be used in conjunction with Matlab (MathWorks, Inc.).

A Matlab OpenSim Pipeline Tool file folder will be downloaded from simtk.org. The BTK toolbox will be added to the proper Matlab directory. When needed, changes to the start frames, end frames, and coordinate system transformations will be made to the btk_loadc3d.m and btk_c3d2trc.m files. The patients' static and dynamic C3D files will be run through the latter Matlab files to create trace (.TRC) and motion (.MOT) files. [3, 4].

OpenSim, 3D musculoskeletal modeling software capable of producing joint reaction forces, will use the .TRC and .MOT files as inputs. Along with .TRC and .MOT files, a series of XML files will be created. The files will include a scale setup file, an

inverse kinematics file, and an inverse dynamics file.

The scale setup file will contain information about the subject's mass, height, the markers used and frames over which to apply the scaling to. This scale setup file will also reference an .OSIM file which will contain information used to develop an initial musculoskeletal model. For this study, the original .OSIM file that will be used is the Hamner-Arnold model (simtk.org). Changes will be made to the Hamner-Arnold .OSIM file that reflect the correct set of markers used in the study.

After the scaling process, inverse kinematics will be run on each model and this will produce a file containing different joint angles. Moments will be generated by running inverse dynamics. The results from these two processes will then be combined to generate joint reaction forces.

RESULTS

In using OpenSim to generate joint angles, some differences will be observed in the numerical values produced by this program and those produced by Vicon. The angles that will be produced by OpenSim will be ~10° greater for each time frame than those given from Vicon. The main attribution to the difference in angles is hypothesized to be the way these software filter the initial data. Regardless of the initial angle produced by OpenSim, the trend of the graph matches accepted research standards.

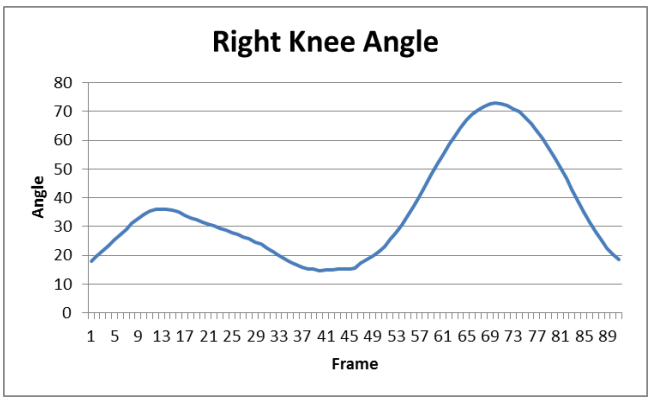

Figure 1: OpenSim filtered and processed kinematic data for a normal patient's right knee over one gait cycle.

For example, figure 1 displays a graph that is representative of standard knee flexion angles during gait. Patient "A" begins in 18° of flexion. At the end of loading response they are in 36° of flexion. They then extend to a similar angle of that at the beginning of the cycle. The peak flexion angle this patient achieved during swing phase was 73°.

DISCUSSION

When comparing the results given from OpenSim, the joint angles follow the same trends during gait as literature values. From initial contact to loading response, Patient A's knee angle increased by 18° compared to accepted values of 10 to 15°. Through preswing and initial swing, Patient A flexes 73°, which is comparable to the standard preswing angle increase of 40° and then an additional 20° during initial swing. The knee extends to neutral again during midswing and terminal swing [5].

The main goal of this project was to obtain joint reaction forces during gait for subjects. This is an ongoing project and the joint reaction forces are still in the process of being generated.

REFERENCES

1. Centers for Disease Control and Prevention (CDC). Prevalence of disabilities and associated health conditions among adults - United States, 1999. MMWR Morb Mortal Wkly Rep. 2001; 50: 120-5.
2. Richards, C. and Higginson J.S. Knee contact forces in subjects with symmetrical OA grades: differences between OA severities. Journal of Biomechanics, 2010, 43(13): 2595-2600.
3. Shimba T., *An estimation of center of gravity from force platform data*, Journal of Biomechanics, 1984, 17(1), 53–60.
4. Zatsiorsky V.M., Kinetics of Human Motion, Human Kinetics Publishers, Champaign, IL, 2002.
5. Perry, Jacquelin. Normal Gait. Atlas of Limb Prosthetics: Surgical, Prosthetic, and Rehabilitation Principles. Digital Resource Foundation for the Orthotics and Prosthetics Community. 2002.

ACKNOWLEDGEMENTS

Dr. Arash Mahboobin of the Human Movement and Balance Laboratory (University of Pittsburgh) for his guidance through OpenSim.

INCREASED VARIABLIITY OF KNEE MOTION AMONG KNEE OSTEOARTHRITIS PATIENTS WITH EPESODIC REPORTS OF INSTABILITY

Megan E. Robinson
Human Movement Research Laboratory, Departments of Physical Therapy & Bioengineering
University of Pittsburgh, PA, USA
Email: mer97@pitt.edu

INTRODUCTION

Knee osteoarthritis (OA) is a prevalent issue for many people as they become older. It can affect everyday life, as the pain suffered from knee OA can be unbearable and make even the simplest of tasks difficult. Along with pain, episodic bouts of knee instability are also commonly reported in patients with knee OA which can further limit their functional capabilities. A knee OA patient is deemed to have instability if they report subjective sensation of buckling, shifting, or giving way of the knee joint [1]. While this definition makes distinguishing between stable and unstable patients relatively easy, understanding the mechanical phenomena responsible for presence of knee instability in patients with knee OA remains elusive. A commonly cited hypothesis regarding the cause of instability is the lack of appropriate dynamic joint control which could lead to increased variability of the knee motion in patients with knee OA. Therefore, we hypothesized that compared to a control group (older adults without knee OA or reports of instability) or a group of knee OA patients without instability, the unstable knee OA patients would demonstrate increased knee joint motion variability. This project focused on first determining the methodology for quantifying variability in knee movement during gait and then determining if there were significant differences in knee motion variability between these groups.

METHODS

Forty-four older adults participated in this study and were divided into 3 mutually exclusive groups of control, knee OA stable and knee OA unstable. Twenty-four subjects were placed in the control group (age:69.6±7.5 yrs, body mass index (BMI): 24.7±3.8 kg/m^2), 9 were placed in the knee OA stable group (age: 69.5±7.9 yrs, BMI: 27.5±5.0 kg/m^2), and 11 were placed in the knee OA unstable group (age: 69.9 ± 8.2 yrs, BMI: 31.5±4.8 kg/m^2). Each subject walked on a declined treadmill (7% grade, 0.75m/s) three separate times. Knee motion was imaged during the loading response phase of gait using dynamic stereo x-ray techniques. Using ground reaction force data taken from an instrumented treadmill, the loading response phase of gait was determined as the first 20% of the gait cycle. The dynamic x-ray data was processed to produce knee joint angles in sagittal, coronal, and transverse planes. Patients' knee movement was also assessed by calculating their angular velocities and plotting these values against time. Variability of knee motion was then quantified for each patient using a previously suggested method that creates an easily interpretable variability index using the joint angle and velocity waveforms described above [2]. Phase angles were then calculated as the angle created by plotting normalized angles of a patients' motion against their normalized angular velocities at each time point during their movement. The angles and velocities were normalized according to the following equations [2]:

$$\theta_i^{norm} = \frac{2 \times (\theta_i - \min(\theta_i))}{\max(\theta_i) - \min(\theta_i)} - 1 \qquad [1]$$

$$\omega_i^{norm} = \frac{\omega_i}{\max(|\omega_i|)} \qquad [2]$$

The angle that is created by the line connecting a specific time point to the origin and the positive horizontal axis is defined as the phase angle. Phase angles (see Figure 1) were calculated for every time point in each trial for each patient, and the phase angles between trials for a specific patient were then compared. This comparison was done by looking at the standard deviation among the phase angles at a specific time point, and doing that for every time point in the loading response phase of gait. For example, if there were three trials of knee motion for a patient with 20 time points, there would be 20 phase angles for each trial, or three phase angles per time point. The standard deviation is then taken of three phase angles from the three

trials at each time point. This would result in 20 standard deviations total, one for each of the 20 time points. The average of all 20 standard deviations for that patient was then taken, resulting in a unique variability index for that patient [2]. A higher variability index indicates that the standard deviations were higher, meaning that there was more variability in a patient's phase angles, or knee motion, between trials.

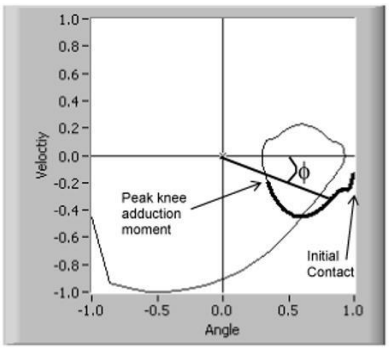

Figure 1. Example of a phase angle using the normalized angles and velocities [2].

DATA PROCESSING

The angles and velocities used for each trial for each patient were put through a custom written MATLAB code that accounted for making the appropriate adjustments to normalize the data so it could then be used to calculate phase angles. The same code then calculated the phase angle for each time point for each trial for each patient, and put this into an organized structure array. This structure was then used to calculate the standard deviations among the phase angles at every time point of the trials for each patient, and put this into another organized structure. The data in this structure was then exported to Excel, where the averages of the standard deviations (ie. Variability Index) for each subject was calculated. This analysis was done in each plane (sagittal, coronal, and transverse), resulting in three variability indexes per patient. An ANOVA with Tukey's correction ($p \leq 0.05$) was used to compare the variability indexes between groups.

RESULTS

In the sagittal plane, variability index for the unstable knee OA group was significantly higher (33.9±19.9) than the control group (17.1±10.9; $p<0.01$) and the stable knee OA group (12.5±15.5; $p<0.1$). However, significant differences were not found in the coronal and transverse planes between any of the groups (Figure 2).

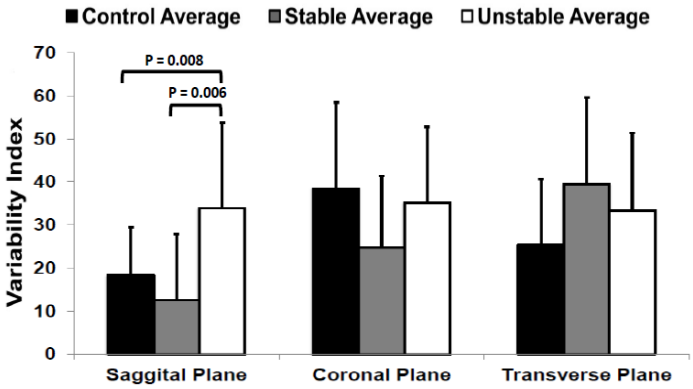

Figure 2. Variability index for knee joint kinematics during loading response phase of decline gait.

DISCUSSION

As hypothesized, there was a significant increase in variability among patients with unstable knee OA compared to the control group in the sagittal plane. This increased variability may be the result of decreased strength of the quadriceps muscles which are the primary muscles responsible for sagittal plane stability of the knee joint during gait. Further testing analyzing the activity of these muscles is necessary to support this hypothesis. Additionally, the absence of significant variability difference in the coronal and transverse plane was not surprising as these secondary movements are not necessary for normal performance of a functional task such as gait. The findings from this study can lead to devising better strategies for assessment of knee motion variability in patients with knee OA. From a clinical perspective, the findings from this study may also help with devising more appropriate treatment strategies for patients with knee OA who report episodic instability through options such as bracing that may limit their sagittal plane knee joint variability.

REFERENCES

1. Farrokhi et al. Altered Tibiofemoral Joint Contact Mechanics and Kinematics in Patients with Knee Osteoarthritis and Episodic Complaints of Joint Instability, *Clinical Biomechanics*, 2013.
2. Lewek et al. Stride-to-Stride Variability of Knee Motion in Patients with Knee Osteoarthritis, Gait Posture, 2006.

ACKNOWLEDGEMENTS

Dr. Farrokhi for being an excellent mentor and inspiring educator. Also to Mr. Gustafson for being extremely patient and a great teacher. Finally to Ms. Paige Kendell and Ms. Meghan Kaffine for being encouraging and thought-provoking lab mates.

EFFECTS OF PHARMACOGENETIC MANIPULATION OF THE NUCLEUS ACCUMBENS ON ALCOHOL-INDUCED TASTE AVERSION

Jake Bosin, Angela Ozburn, Colleen McClung
The McClung Lab, Department of Psychiatry, Translational Neuroscience Program
University of Pittsburgh, PA, USA
Email: jrb157@pitt.edu Web: http://www.mcclung.pitt.edu

INTRODUCTION

A recent clinical trial has shown that Deep Brain Stimulation of the nucleus accumbens (NAc) in severely alcohol-dependent subjects results in a "complete disappearance of [alcohol] craving" and a reduction in relapse [1]. These results, although promising, are very poorly understood from a mechanistic standpoint. Prior work in this area has shown that using DREADDs to increase NAc activity results in decreased ethanol (EtOH) self-administration, however, increasing NAc activity in this way doesn't change the rewarding value of EtOH as measured by conditioned place preference. Therefore, we hypothesize that increased activity in the NAc could decrease alcohol-seeking behavior by increasing the aversive effects of alcohol, which is what the present study aims to investigate using a Conditioned Taste Aversion (CTA) experimental paradigm.

CTA is a specialized, highly robust form of Pavlovian conditioning wherein an animal associates a taste (conditioned stimulus [CS]) with the aversive effects of a toxic or poisonous substance (unconditioned stimulus [US]). In the first published CTA experiment, for example, a novel saccharin solution was paired with a dose of radiation, resulting in decreased consumption of the saccharin solution [2]. A CTA can also be induced by association of a novel taste with drugs of abuse such as alcohol, morphine, THC, cocaine, and amphetamine [3]. Though this seems at first somewhat counter-intuitive, as these drugs are rewarding and reinforcing, it shows these drugs also have negative effects which can be measured in a CTA experimental paradigm. In the present study, the effects of alterations in activity of the NAc to the aversive effects of alcohol are examined using such a methodology.

To produce these alterations, we used a recently engineered class of mutagenized muscarinic receptors called DREADDs (Designer Receptors Exclusively Activated by Designer Drugs). DREADDs, unlike endogenous muscarinic receptors, do not bind to acetylcholine and are instead activated by the otherwise pharmacologically inert drug clozapine n-oxide (CNO). There are two kinds of DREADDs used in this study; hM3Dq, a Gq-coupled GPCR whose activation increases intracellular calcium levels which increases neuronal firing, and hM4Di, which is Gi-coupled so its' activation decreases cAMP and increases GIRK activity resulting in decreased neuronal firing.

In this study, one group of mice were stereotaxically injected (billaterally into the NAc) with AAV expressing the mutated M3-receptor (hM3Dq) to increase NAc activity, another group with the mutated M4-receptor (hM4Di) to decrease NAc activity, and a final group was injected with GFP as a control (CNO should not have any effect on this group as it does not express a DREADD).

METHODS

Female C57BL/6J mice (n=11-13/group) were stereotaxically injected with AAV hM3Dq, hM4Di, or GFP bilaterally into the NAc, and subsequently underwent 2 weeks of recovery, followed by a week of limited water access (9-11AM daily). To conduct the actual experiment, the mice were then given 1 hour of access to a 0.15% Saccharin solution without CNO or EtOH injections, followed by a planned 10 days of 5 EtOH-saccharin pairings ("trial days") interspersed with 5 limited-water access days (Fig. 1A). On trial days, the mice were injected with CNO (1g/kg) at 9:30AM, allowed access to the saccharin solution from 10-11AM, and then at 11AM control animals (4/treatment) were injected with saline, and the rest were injected with 2g/kg EtOH IP (intraperitoneally). On trial days, mice were given unmeasured access to water from 4-5 pm to prevent dehydration. On the days in between trials, mice were allowed unmeasured access to water from 9-11AM.

On the sixth day of the experiment (between the second and third trials), however, the mice were accidentally given the saccharin solution instead of water (without CNO injections), so the entire initial methodology had to be abandoned and a new methodology was constructed. In the revised experimental design (Fig. 1B), the mice were given two different Kool Aid solutions (0.1% Kool Aid, 0.15% saccharin in tap water) in grape and cherry flavors. On the first day of the experiment, the mice were given both solutions for 1 hour (10-11AM) of measured drinking. On days 2 and 4 of the experiment, all 35 mice were given IP injections of CNO (1g/kg) 30 minutes prior to 1 hour (10-11AM) of measured drinking of the cherry flavored solution, followed immediately by IP injections of EtOH (2.5g/kg). On days 3 and 5, all mice were given IP injections of CNO 30 minutes prior to 1 hour (10-11AM) of measured drinking of the grape solution, followed immediately by IP saline injections. On the

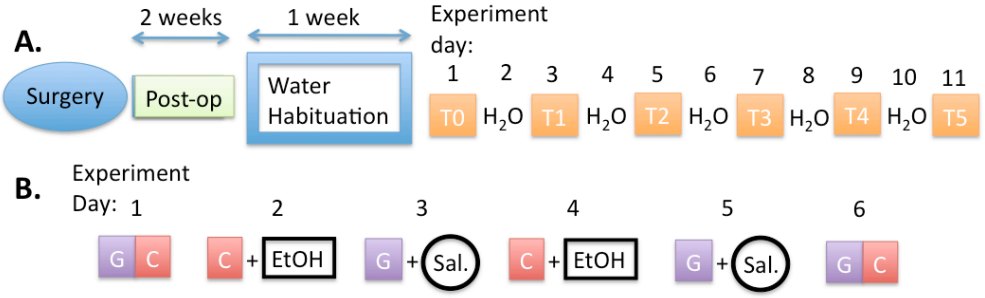

Figure 1: Experimental timeline. [A] Shows the timeline as originally designed, [B] shows the modifications made after the original methodology had to be abandoned

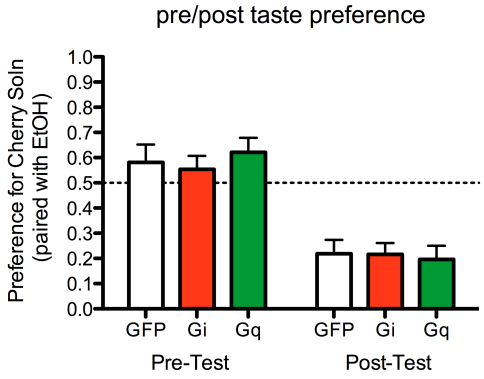

Figure 2: Pre-(day 1) and Post-(day 6) experiment cherry solution preferences for the GFP, hM3Dq (Gq) and hM4Di (Gi) groups (n = 7-10/group). Preference is cherry intake divided by total (grape + cherry) intake).

sixth day, the mice were again allowed access to both flavors for 1 hour of measured drinking without any injections.

RESULTS

Two-way ANOVA was used to analyze the data (Fig. 2) where the factors were time (pre/post test) and treatment group (GFP/Gi/Gq). A main effect of time was observed indicating a significant EtOH-induced CTA occurred in all groups ($F(2,32)=70.62$, $p < 0.0001$). However, we did not observe a main effect of treatment group, thus no significant difference in CTA-expression was found between treatment groups ($F(2,32)=0.08$, $p = 0.92$).

DISCUSSION

The results seem to suggest that changing the activity of the NAc has no impact on expression of an EtOH-induced CTA, which is unexpected, considering the results of previous studies [see introduction] and the robust effects observed in Vogues et al.'s clinical trial. One possible explanation for this is that the NAc may be involved in alcohol craving, but the associations mediating a CTA occur in other brain regions. This seems unlikely, however, as the results of several taste studies[4] indicate a strong role for the NAc in taste memory formation/retrieval and the association of taste unconditioned and conditioned stimuli. Another possible explanation is that the different groups could develop a CTA at different rates, as the data presented here does not take into account the acquisition, or development of the taste aversion, but only looks at the final expression of aversion.

There are a myriad of other possible explanations for the results. We injected the DREADDs into both the shell and core of the NAc, but it's possible there are subregion-specific effects of NAc activity (shell vs. core) on alcohol consumption. We assumed in our experimental design that the association between the CNO injection and saccharin consumption is negligible compared to the association of saccharin and EtOH injections, but this is not necessarily the case. It could be that CNO should be given with EtOH instead of before saccharin. It could be also be important to give CNO 4 hours post-EtOH injection to "relieve" withdrawal symptoms, which are at a maximum at 6 hours after acute injection.

It's unclear if the lack of significant difference observed between treatment groups is because changing activity in the NAc doesn't alter acquisition of an EtOH-induced CTA, or because a mistake forced us to abandon the original methodology and attempt a recovery with an unexplored experimental design. Therefore, I propose we repeat the experiment again using the original methodology, perhaps with altered injection times.

REFERENCES

1. Voges, Juergen. 2012. Deep Brain Stimulation Surgery for Alcohol Addiction. *World Neurosurg.*
2. Garcia, J. et al. 1955. Conditioned aversion to saccharin resulting from exposure to gamma radiation. *Science.* **122:** 57-58.
3. Davis, C.M. and A.L. Riley. 2010. Conditioned taste aversion learning. *Ann. N.Y. Acad. Sci.* **1187:** 247-275.
4. Ramirez-Lugo, L. et al. 2007. Taste Memory Formation: Role of Nucleus Accumbens. *Chem. Senses*. **32**: 93-97.

AKNOWLEDGEMENTS

I would like to thank my mentors Dr. Ozburn and Dr. McClung for their endless support and patience and to the Department of Bioengineering for providing me with funding to pursue this wonderful opportunity.

Creation of a Handheld NIRS Imaging Device for Infants

Deanna Pelkey and Ted Huppert
NIRS Brain Imaging Lab
University of Pittsburgh, PA, USA
Email: dcp26@pitt.edu Web: http://www.pitt.edu/~huppert1/Huppert_Lab/Welcome.html

Introduction: Currently, there are many different methods to study brain activity. Some of these techniques include magnetic resonance imaging (MRI), positron emission tomography (PET), and near-infrared spectroscopy (NIRS). While MRI and PET scans can provide crucial information about a patient's brain function, these scans can be lengthy and cannot be used with all patients. These restrictions make it difficult to perform a scan on an infant. A way to avoid these issues involves an Imagent system, such as an ISS. An ISS machine uses infrared lights, at wavelengths of 690 nm and 830 nm, which go through the tissue of a patient to provide information about the brain. The ISS then calculates the absorbance and scattering coefficients of the subject. These coefficient values are used to understand the oxygen saturation levels and total hemoglobin of a subject's brain. This system provides a non-invasive and simple way to take measurements on a subject.

The total amount of hemoglobin in a patient represents the number of oxygen carrying cells in the blood and is vital for understanding if a patient's brain is receiving enough oxygen. The normal range for total hemoglobin for an adult male is 14-18 gm/dL, while the normal range for an adult female is 12-16 gm/dL.[1] The total oxygen saturation value relates to the percentage of hemoglobin that is bound to oxygen. A normal oxygen saturation value is around 90%, meaning that 90% of hemoglobin is oxygenated.[2] As the oxygen saturation level decreases, there is a higher risk for brain damage, with brain damage usually occurring around a oxygen saturation level of 65%.

The purpose of this experiment is to create a small, handheld device that can be used to take consistent measurements of the brain activity of infants. This device should also be portable and ultimately should be kept in the Children's Hospital of Pittsburgh. It must also be flexible enough to accommodate infant heads of different circumferences and it must be sterile.

Materials and Methods: In order to make the portable handheld device, an 8.2 cm by 6.2 cm rectangle of flexible foam was cut. Then, two circles, each a diameter of 2.2 cm, were cut out of the rectangle. Two rubber stoppers were then used to house the source fibers and the detector fiber separately. There is one detector fiber and four source fibers in this model. In order to hold the fibers, holes were drilled into the rubber stoppers and the fibers were pushed through these holes and then the rubber stoppers were glued into the foam rectangle. Picture 1 shows the final design of the device. The fiber optics were then connected to the ISS Imagent machine and calibration measurements were recorded. These measurements consisted of calibrating the machine on Phantom A, and then recording the data for 100 seconds on Phantoms A and B. Picture 2 shows the handheld being calibrated on Phantom A.

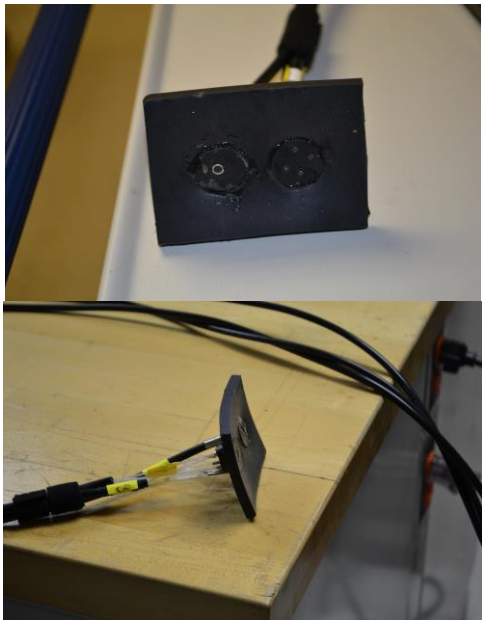

Picture 1

After the calibrations were performed, the handheld device was used on human subjects. The handheld was calibrated on Phantom A, and then the device was placed on a subject's head for 60 seconds. This was repeated on 3 different subjects for 6 trials. The oxygen saturation levels and total hemoglobin levels for each patient were calculated for each trial. The median oxygen saturation and

total hemoglobin were found for each individual patient.

Picture 2

Results and Discussion: The handheld was calibrated on Phantom A and then the absorption coefficient, μ_a, of Phantom B was measured. The measured values were then compared to the known values of μ_a for Phantom B, as seen in Table 1. From Table 1, the measured values of μ_a are slightly lower than the actual values of the absorption coefficient, with a percent error of approximately 26% for 690 nm. This could be due to light penetrating the fiber optics or the calibration of the machine. Even though there is a small amount of error in the measured values, they are still consistent enough to take measurements on an infant's head.

Table 1. Calculated and measured values of μ_a for Phantom B at wavelengths of 690 nm and 830 nm.

	Calculated Values (cm^{-1})	Measured Values (cm^{-1})
690 nm	0.133	0.093
830 nm	0.128	0.100

After the calibration process, the median values of the total hemoglobin and total oxygen saturation of each patient were calculated. These values can be seen in Table 2.

Table 2. Median Total Hemoglobin and Median Total Oxygen Saturation Values for Subjects

Subject Number	**Total Hemoglobin (g/dL)**	**Total Oxygen Saturation (%)**
Subject1	17.98	77.24
Subject 2	19.83	73.25
Subject 3	17.75	78.66

The average range of total hemoglobin for an adult male is 14 g/dL – 18 g/dL and the range for a adult female is 12-16 g/dL. From these literatures values, it can be seen that the measured total hemoglobin values of all of the subjects are in the normal range.

A normal oxygen saturation level is approximately 90%. The subjects measured values are all below this normal value.

Conclusions: Overall, the handheld device is a valid way to take measurements of an infant's brain. The handheld can be calibrated correctly and then used to take measurements. While the device measured total hemoglobin levels that were in an appropriate range, the measured total oxygen saturation levels were slightly lower than normal. This could be due to variability in the measurements and can be fixed by limiting the amount of outside light and by calibrating the handheld to Phantom A between each trial.

Acknowledgements: I would like to thank the University of Pittsburgh Swanson School of Engineering for funding my project. I would also like to thank Dr. Ted Huppert, Jeff Barker for programming the code to determine the coefficient values, Helmut Karim, and Nancy Beluk for their help on my project.

References:

1. "Definition of Hemoglobin Normal Values." *MedicineNet*. N.p., 14 6 2012. Web. 23 Aug 2013. <http://www.medicinenet.com/script/main/art.asp?articlekey=15737>.
2. "Definition of Hemoglobin Normal Values." *MedicineNet*. N.p., 14 6 2012. Web. 23 Aug 2013. <http://www.medicinenet.com/script/main/art.asp?articlekey=15737>.
3. Fantini, Sergio, and Maria Angela Franceschini, et all. "Quantitative determination of the absorption spectra of chromophores in strongly scattering media: a light-emitting-diode based technique." *Applied Optics*. 33.22 (1994): 9. Print.

CHARACTERIZING REAL-TIME PLATELET DEPOSITION ONTO CLINICALLY RELEVANT SURFACES

Drake D. Pedersen, Megan A. Jamiolkowski, Marina V. Kameneva, James F. Antaki, William R. Wagner
McGowan Institute for Regenerative Medicine
University of Pittsburgh, PA, USA
Carnegie Mellon University, PA, USA
Email: ddp17@pitt.edu, Web: http://www.mirm.pitt.edu/

INTRODUCTION

Heart disease is the leading cause of death in the United States, killing approximately 600,000 Americans per year [1]. In order to treat heart disease, the first generation pulsatile flow ventricular assist devices (VADs) were implemented as a bridge-to-transplant therapy. The development of continuous flow VADs decreased the size and power requirements and have extended mechanical life of VADs. For example, the Heartmate II (Thoratec Corp.), is FDA approved for use as destination therapy. Many VAD manufacturers utilize highly polished titanium alloy (TiAl6V4) as the blood contacting surface of their devices. However, *in vitro* studies have shown these titanium alloy VADs to be subject to elevated acute thrombogenicity, compared to other candidate materials or coatings [2].

Thrombosis and thromboembolism are pernicious concerns associated with VADs and must be thoughtfully considered when choosing a biomaterial. For any VAD, platelets may be activated from high wall shear rates, complex flow patterns, contact surface area, and a number of agonists [3]. Improving the blood biocompatibility of VAD surfaces may help reduce the risk of thrombosis and thromboembolic events. Developing a method to visualize time dependent platelet adhesion onto clinically relevant surfaces could improve material selection. Because opaque materials are often used in VADs, traditional methods for real time platelet deposition are not applicable. This study aims to provide a novel method of visualizing platelet adhesion to opaque surfaces under physiologically normal flow patterns and wall shear rates.

METHODS

In order to visualize platelet adhesion without disrupting the laminar flow of blood, a specialized chamber was designed. The chamber was sealed by placing an acrylic top plate over the test material with a silicon gasket representing the flow path in between. Aluminum shim stocks were placed between the top plate and material to provide a channel height of precisely 76 μm. In all, six materials were tested in the study: the titanium alloy control, TiAl6V4 (Ti), Al_2O_3 (Al), 2-methacryloyloxyethyl phosphorylcholine coated TiAl6V4 (MPC), Silicone Carbide (SiC), Yttria Partially Stabilized Zirconia (YZTP), and Zirconia Toughened Alumina (ZTA).

Because whole blood is opaque, red blood cells (RBCs) were converted to ghost cells (for transparency) through modifications of established protocols [4]. Platelet-rich plasma was fluorescently labeled and mixed with the RBC ghosts at a hematocrit of 25%. Then, blood was perfused through the parallel plate chamber across the test surfaces at a flow rate to produce a wall shear rate of $1000s^{-1}$. Platelet adhesion was visualized in real time under an inverted epifluorescence microscope with a 40x super long working distance objective. Images were acquired using a CCD camera and analyzed for percent platelet surface coverage using a custom designed MatLab program.

It was also necessary to quantify how many platelets had been activated, but had not adhered. To do this, we used a flow cytometer on blood samples from each material at zero and five minutes to determine percent activation of platelets.

RESULTS

Our results show that platelet deposition onto Ti, measured as percent coverage, was significantly higher than any of the other five materials tested ($p < 0.01$). We used two-way ANOVA with specific post-hoc testing using the Bonferroni correction to

compare results of each material with the control, TiAl6V4.

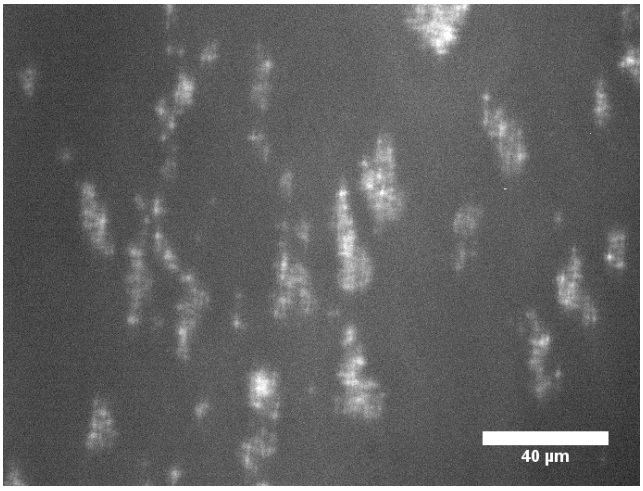

Figure 1. Real-time platelet deposition onto TiAl6V4 after five minutes of blood perfusion

The percent platelet coverage of Ti at the end of the five minute perfusion was 5.375 ± 0.979%. As shown in **figure 1**, many thrombi formed on the surface of Ti. What is not shown is that, from the thrombi seen on the surface, emboli would periodically form and break off from the adhered body of platelets. At the end of the five minute perfusion, the results for percent platelet coverage on the other materials are as follows: Al = 1.253 ± 0.335, SiC = 0.7246 ± 0.424, MPC = 0.7178 ± 0.251, YZTP = 0.6617 ± 0.182, ZTA = 0.3523 ± 0.154. Alumina was the only material aside from Ti that had a percent coverage of greater than one.

DISCUSSION

Although Ti has been used in VADs for its durable qualities, resistance to corrosion, and biocompatibility, this study and another study by Schaub et al. have shown that Ti is not the most compatible material for blood contact in VADs [4]. This study has provided a novel method to assess compatibility of alternative materials in VAD design.

The use of RBC ghosts in this study allowed for visualization of real-time platelet deposition without disruption of the blood flow path. A limitation of the study conducted by Schaub et al. was that the flow path was disturbed by a fiber optic probe inserted into the flow path [5]. Our non-invasive method allows for more physiologically relevant results because there is no intrusion into the flow path, and RBC ghosts have shown to have very similar flow characteristics to whole blood.

Computer models have been constructed to simulate when and where platelet adhesion onto artificial surfaces will occur [6]. Although computer modeling is outside the scope of this paper, it is still useful to predict platelet deposition onto clinically relevant surfaces. It is now possible, however, to visualize in real time and measure how platelets react to surfaces.

Based on our results, Ti is the least effective material that we tested to use in VADs. Our data show that a material such as ZTA would offer a much safer alternative to Ti for use in VADs, as it has shown to be much less susceptible to thrombosis, averaging only 0.3523 ± 0.154 percent platelet coverage of the surface tested. This result is significantly lower than that of Ti in the acute tests that we ran. It would be worth testing ZTA further to determine if it could potentially reduce the risk of thrombosis in VADs.

A limitation of this study is that it is an acute test, whereas VAD patients can now use their devices for months if not years at a time. However, when determining an alternative material for *in vivo* testing, it would be more ideal to select a surface that has very little platelet surface coverage after five minutes compared to surfaces that promote formation of large thrombi within the same period of time.

REFERENCES

[1] Murphy et al. *Deaths: Final Data for 2010,* 2010
[2] Wagner et al. *J. Biomater. Sci.,* **11**, 1239-1259, 2000
[3] Cosemans et al. *Cardiovascular Research* **99**, 342–352, 2013
[4] Schwoch et al. *Biochemistry*. **2**, 197-218, 1973
[5] Schaub et al. *J Biomed Mater Res.* **49**, 460-468, 2000
[6] Hund et al. *Phys Med Biol.* **54**, 6415–6435, 2009

ACKNOWLEDGEMENTS

I would like to acknowledge Megan Jamiolkowski for allowing me to partake in her project and for teaching me the theory behind the experiment.